

UNIVERSITY OF CRETE
DEPARTMENT OF MATERIALS SCIENCE AND
TECHNOLOGY
NATIONAL CENTER FOR SCIENTIFIC RESEARCH
“DEMOKRITOS”

ELENI ANDROULAKI

MOLECULAR SIMULATION OF IONIC LIQUIDS
FOR ENVIRONMENT-FRIENDLY TECHNOLOGICAL
APPLICATIONS

DOCTORAL DISSERTATION



HERAKLEION, MARCH 2014



ΠΑΝΕΠΙΣΤΗΜΙΟ ΚΡΗΤΗΣ
ΣΧΟΛΗ ΘΕΤΙΚΩΝ ΚΑΙ ΤΕΧΝΟΛΟΓΙΚΩΝ ΕΠΙΣΤΗΜΩΝ
ΤΜΗΜΑ ΕΠΙΣΤΗΜΗΣ ΚΑΙ ΤΕΧΝΟΛΟΓΙΑΣ ΥΛΙΚΩΝ

ΠΡΑΚΤΙΚΟ ΔΗΜΟΣΙΑΣ ΠΑΡΟΥΣΙΑΣΗΣ ΚΑΙ ΕΞΕΤΑΣΗΣ
ΤΗΣ ΔΙΔΑΚΤΟΡΙΚΗΣ ΔΙΑΤΡΙΒΗΣ ΤΗΣ
κας. Ανδρουλάκη Ελένης
ΥΠΟΨΗΦΙΑΣ ΔΙΔΑΚΤΟΡΟΣ ΤΟΥ ΤΜΗΜΑΤΟΣ ΕΠΙΣΤΗΜΗΣ ΚΑΙ
ΤΕΧΝΟΛΟΓΙΑΣ ΥΛΙΚΩΝ

Η Επταμελής Επιτροπή της Διδακτορικής Διατριβής της κας. Ανδρουλάκη Ελένης η οποία ορίστηκε στην 57η Γ.Σ.Ε.Σ. στις 20/12/2013, εκλήθη την Παρασκευή 21 Μαρτίου 2014 να εξετάσει την σύμφωνα με το Νόμο υποστήριξη της διατριβής της υποψηφίου με τίτλο:

«Μοριακή Προσομοίωση Ιοντικών Υγρών για Τεχνολογικές
Εφαρμογές Φιλικές Προς το Περιβάλλον»
«Molecular Simulation of Ionic Liquids for Environment-
Friendly Technological Application»

Τα παρόντα μέλη της επταμελούς Επιτροπής εκφράζουν ομόφωνα την πλήρη ικανοποίησή τους για την υψηλή ποιότητα του περιεχομένου και της υποστήριξης της διατριβής.

Τα ερευνητικά αποτελέσματα της εργασίας της κας. Ανδρουλάκη Ελένης είναι σημαντικά, πρωτότυπα και διεκδικούν το πεδίο της έρευνας στην Επιστήμη και Τεχνολογία Υλικών.

Ως εκ τούτου η Εξεταστική Επιτροπή προτείνει ομόφωνα την απονομή του Διδακτορικού Διπλώματος στην κα. Ανδρουλάκη Ελένη.

Τα μέλη της επταμελούς επιτροπής για την αξιολόγηση της Διδακτορικής Διατριβής της κας. Ανδρουλάκη Ελένης.

Η Επταμελής Επιτροπή:

Βλασσόπουλος Δημήτριος	(Επιβλέπων)	
Καθηγητής Τμήματος Επιστήμης και Τεχνολογίας Υλικών, Παν/μιου Κρήτης		
Φυτάς Γεώργιος		
Καθηγητής Τμήματος Επιστήμης και Τεχνολογίας Υλικών, Παν/μιου Κρήτης		
Ρεμεδιάκης Ιωάννης		
Μόνιμος Επίκουρος Καθηγητής Τμήματος Επιστήμης και Τεχνολογίας Υλικών, Παν/μιου Κρήτης		
Χαρμανδάρης Ευάγγελος		
Επίκουρος Καθηγητής Τμήματος Εφαρμοσμένων Μαθηματικών, Παν/μιου Κρήτης		
Θεοδώρα Θεόδωρος		
Καθηγήτρια, Σχολή Χημικών Μηχανιών ΕΜΠ		
Ρωμανός Γεώργιος		
Ερευνητής Β, Ινστιτούτο Προηγμένων Υλικών, Φυσικοχημικών Διεργασιών, Νανοτεχνολογίας και Μικροσυστημάτων, ΕΚΕΦΕ «Δημόκριτος»		
Οικονόμου Ιωάννης		
Ερευνητής Α, Ινστιτούτο Προηγμένων Υλικών, Φυσικοχημικών Διεργασιών, Νανοτεχνολογίας και Μικροσυστημάτων, ΕΚΕΦΕ «Δημόκριτος»		

Molecular Simulation of Ionic Liquids for Environment-Friendly Technological Applications

Thesis Author: Eleni Androulaki

Thesis Supervisor: Professor Dimitris Vlassopoulos
Research Director Ioannis G. Economou

Thesis Committee: Professor Georgios Fytas
Professor Doros N. Theodorou
Research Director Georgios Romanos
Assistant Professor Vagelis Harmandaris
Assistant Professor Ioannis Remediakis

*Αφιερώνεται με σεβασμό
στον Παναγιώτατο Οικουμενικό Πατριάρχη κ.κ. Βαρθολομαίο·
εκείνον που προσεύχεται και αγωνίζεται για τη σωτηρία του
πλανήτη και την ευαισθητοποίηση των ανθρώπων όλης της γης.
Το ήθος και το παράδειγμά του υπήρξαν πηγή έμπνευσης
στην πορεία αυτής της εργασίας.*

*This Thesis is respectfully dedicated
to his Holiness Ecumenical Patriarch Bartholomew, one who prays
and strives to save the planet and to awake the awareness of people
all around the earth. His ethos and paradigm were an inspiration
in the process of the present study.*

Ευχαριστίες

Η παρούσα Διδακτορική Διατριβή δεν θα είχε πραγματοποιηθεί χωρίς την συμβολή και την συμπαράσταση πολλών ανθρώπων.

Κατ' αρχήν θα ήθελα να ευχαριστήσω θερμά τα μέλη της επταμελούς εξεταστικής επιτροπής για τα ουσιαστικά σχόλια και τις παρατηρήσεις τους όσον αφορά το περιεχόμενο της εργασίας, καθώς επίσης και όλους όσους παρευρέθηκαν στην υποστήριξή της, τόσο για το ενδιαφέρον που έδειξαν όσο και για τον χρόνο που αφιέρωσαν.

Ευχαριστίες οφείλω στον Δρ. Ιωάννη Οικονόμου, διευθυντή του εργαστηρίου Μοριακής Θερμοδυναμικής και Μοντελοποίησης Υλικών του Εθνικού Κέντρου Έρευνας Φυσικών Επιστημών «Δημόκριτος», που με την εμπιστοσύνη του στήριξε την παρούσα μελέτη από το ξεκίνημά της και υπήρξε σύμβουλος και καθοδηγητής καθ' όλη την πορεία της, παρά τις αντιξοότητες που αναπόφευκτα προέκυπταν. Ιδιαίτερος θα ήθελα να εκφράσω τις ολόθυμες ευχαριστίες μου στην Δρ. Νίκη Βέργαδου για την στήριξη, την υπομονή και την ουσιαστική συμβολή της στην πραγμάτωση αυτής της μελέτης. Ευχαριστώ και όλα τα υπόλοιπα μέλη του εργαστηρίου για την ανταλλαγή ιδεών και απόψεων, αλλά και για το ευχάριστο και δημιουργικό περιβάλλον εργασίας, που οφείλεται στην παρουσία τους.

Τέλος, θα ήθελα να εκφράσω τις ολόψυχες ευχαριστίες μου στον Σεβασμιώτατο Αρχιεπίσκοπο Κρήτης κ. Ειρηναίο, ο οποίος ευλόγησε αυτή την προσπάθεια και με στήριξε με πατρική αγάπη σε κάθε δύσκολη στιγμή· στην Καθηγουμένη και τις αδελφές της Ιεράς Μονής Χρυσοπηγής Χανίων, για τις προσευχές και την αμέριστη συμπαράστασή τους· στα αδέρφια μου και ιδιαιτέρως, στους γονείς μου, Σπύρο και Μαγδαληνή, για την άνευ όρων αγάπη τους και την υποστήριξή τους όλα αυτά τα χρόνια.

Acknowledgements

The present Doctoral Dissertation would not have been completed without the contribution and the support of many people.

First of all, I would like to thank the members of the thesis committee for their vital comments and remarks on the context of this study, and also all of the people who attended the thesis defense for their interest and the time they devoted.

I would like to thank Dr. Ioannis G. Economou, director of the Molecular Thermodynamics and Modeling of Material Laboratory in the National Center of Scientific Research “Demokritos”, who truly supported the present study for the beginning and has been an advisor and a mentor since then, despite the difficulties that inevitably aroused. Particularly, I would like to hearty thank Dr. Niki Vergadou for her support, her patience and her crucial contribution to the completion of the present study. I would also like to thank all the other member of the laboratory for the useful discussions, but also, for creating a fruitful and creative working environment.

Finally, I would like to sincerely thank his Eminence Archbishop of Crete Irinaios, who blessed this effort and supported me with fatherly love at every difficult moment; the Abbess and the sisters of the Holy Monastery of Chrysopigi in Chania, for their prayers and their undivided support; my brother and sisters and, especially, my parents Spyros and Magdalini, for their unconditional love and sacrificial support all these years.

Abstract

In the present Thesis, a molecular simulation methodology has been applied for the study of imidazolium-based bis-trifluoromethylsulphonyl ($[C_n\text{mim}^+][\text{Tf}_2\text{N}^-]$) and tricyanomethanide ($[C_n\text{mim}^+][\text{TCM}^-]$) ionic liquids (ILs). The main goal of the Thesis was the investigation of the properties of pure ILs and the study of their permeability and selectivity properties to gases that are present in the gas stream of a coal-fired power plant and, most importantly, their capability to capture CO_2 which is the most important greenhouse gas. Optimized classical atomistic force fields have been employed and very long molecular dynamics (MD) simulations were performed in a wide temperature range and at atmospheric pressure in order to predict the thermodynamic, structural and transport properties of the pure ILs and to analyze their complex microscopic behavior. Imidazolium-based $[\text{TCM}^-]$ ILs, in particular, were studied for the first time using a classical atomistic force-field that was optimized in order to accurately predict density and diffusion coefficients. Gas diffusivity was studied by performing additional very long MD simulations while gas solubility was calculated using the Widom test particle insertion method. The predicted absorption selectivities for the two imidazolium-based ($[\text{Tf}_2\text{N}^-]$ and $[\text{TCM}^-]$) families confirm that the $[\text{TCM}^-]$ ILs are very promising candidates for use in gas separation technologies and, in particular, for the capture of CO_2 from a gas stream of coal-fired power plants. The influence of the anion, the cationic alkyl chain length and the temperature on the above properties was studied in depth and a wealth of microscopic information was extracted on the underlying molecular mechanisms that control the macroscopic behavior of these materials. In all cases, the agreement between available experimental data and the results from molecular simulation is very good.

Περίληψη

Στην παρούσα Διδακτορική Διατριβή μια μεθοδολογία μοριακής προσομοίωσης εφαρμόστηκε για την μελέτη ιοντικών υγρών που περιλαμβάνουν κατιόντα με βάση το ιμιδαζόλιο και δύο διαφορετικά ανιόντα, το διτριφλουορομεθυλοσουλφονύλιο ($[C_n\text{mim}^+][\text{Tf}_2\text{N}^-]$) και το τρικυανομεθανίδιο ($[C_n\text{mim}^+][\text{TCM}^-]$). Ο κύριος στόχος της Διδακτορικής Διατριβής ήταν η διερεύνηση των ιδιοτήτων των καθαρών υλικών και η μελέτη των ιδιοτήτων διαπερατότητας και εκλεκτικότητάς τους σε παράγωγα αέρια μονάδων παραγωγής ηλεκτρικής ενέργειας καύσης άνθρακα και ιδιαιτέρως, της ικανότητάς τους να δεσμεύουν διοξείδιο του άνθρακα (CO_2), το πλέον υπεύθυνο αέριο για το φαινόμενο του θερμοκηπίου. Χρησιμοποιήθηκαν βελτιστοποιημένα πεδία δυνάμεων για την διενέργεια προσομοιώσεων μοριακής δυναμικής (ΜΔ) σε μεγάλο θερμοκρασιακό εύρος και σε ατμοσφαιρική πίεση ώστε να προβλεφθούν οι διάφορες θερμοδυναμικές, δομικές και δυναμικές ιδιότητες, καθώς επίσης και για να γίνει η ανάλυση της σύνθετης μικροσκοπικής συμπεριφοράς των υπό μελέτη υλικών. Είναι η πρώτη φορά που ιοντικά υγρά με ιμιδαζολικά κατιόντα και ανιόν το $[\text{TCM}^-]$ μελετώνται με χρήση ενός κλασσικού ατομιστικού πεδίου δυνάμεων το οποίο και βελτιστοποιήθηκε ώστε να προβλέπονται με ακρίβεια η πυκνότητα και οι συντελεστές αυτό-διάχυσης των ιόντων. Οι διαχυτότητες των αερίων υπολογίστηκαν με διεξαγωγή επιπρόσθετων προσομοιώσεων ΜΔ ενώ οι διαλυτότητές τους στα υπό μελέτη υλικά υπολογίστηκαν με χρήση της μεθόδου ένθεσης σωματιδίου ελέγχου του Widom. Οι προβλεπόμενες εκλεκτικότητες απορρόφησης για τις δύο οικογένειες ιοντικών υγρών καταδεικνύουν τα ιμιδαζολικά $[\text{TCM}^-]$ ιοντικά υγρά ως πολύ υποσχόμενα υλικά για χρήση σε διεργασίες διαχωρισμού αερίων και ιδιαιτέρως, σε εφαρμογές που στοχεύουν στην δέσμευση διοξειδίου του άνθρακα από μονάδες παραγωγής ηλεκτρικής ενέργειας καύσης άνθρακα. Η επίδραση του ανιόντος, τους μήκους της αλκυλικής αλυσίδας του κατιόντος και της θερμοκρασίας στις υπό μελέτη ιδιότητες μελετήθηκε σε βάθος, ενώ εξάχθηκε ένα πλήθος συμπερασμάτων που αφορά στους μοριακούς μηχανισμούς που ελέγχουν την μακροσκοπική συμπεριφορά των υπό μελέτη υλικών. Τα αποτελέσματα της μοριακής προσομοίωσης είναι σε κάθε περίπτωση σε πολύ καλή συμφωνία με τα πειραματικά δεδομένα.

Table of Contents

List of Tables	5
List of Figures	9
List of Symbols	15
1. Introduction.....	17
1.1 Characteristics and Properties of Ionic Liquids	17
1.2 Applications of Ionic Liquids - Capture of CO ₂	20
1.3 Theoretical Studies of Ionic Liquids	21
1.3.1 Molecular Simulation	22
1.3.2. Equations of State for Ionic Liquids.....	22
1.4 Motivation and Outline of the Thesis.....	23
2. Structure, Thermodynamic and Transport Properties of Imidazolium-Based [Tf ₂ N ⁻] Ionic Liquids	27
2.1 Simulation Details	28
2.2 Force Field.....	29
2.3. Results and Discussion.....	30
2.3.1. Thermodynamic Properties.....	30
2.3.2. Microscopic Structure.....	32
2.3.3 Segmental Dynamics	38
2.3.4. Self-Diffusion Coefficients.....	43
2.3.5. Shear Viscosity	46
2.4 Conclusions	48
3. Analysis of the Heterogeneous Dynamics of Imidazolium-Based [Tf ₂ N ⁻] Ionic Liquids and Prediction of their Transport Properties Using a Further Optimized Force Field	51
3.1 Simulation Details	51
3.2 Force Field Optimization	52

3.2.1 Implementation of the Classical Drude Oscillator Model	53
3.2.2 Use of Reduced Total Ionic Charge	54
3.3 Results on Density, Self-diffusivity and Viscosity	56
3.4 Dynamic Behaviour of Ionic Liquids	60
3.4.1 Analysis of the Ions' Translational Motion	60
3.4.2 Dynamic Heterogeneity	63
3.5 Conclusions	72
4. Imidazolium-Based [TCM ⁺] Ionic Liquids: Optimization of an All-atom Force Field and Prediction of Thermodynamic, Structure and Transport Properties	73
4.1 Simulation Details	74
4.2 Force Field Optimization	75
4.3 Force Field Validation and Prediction of Properties	83
4.3.1 Density and Structure Properties	83
4.3.2 Transport Properties	89
4.3.3 Anisotropy in Cation's Translational Motion.....	91
4.3.4 Cluster Formation of Dynamically Distinguishable Ions	93
4.4 Conclusions	95
5. Permeability Properties of [TF ₂ N ⁻] and [TCM ⁺] Imidazolium-Based Ionic Liquids to Gases	97
5.1 Force Fields	97
5.2 Simulation Details	97
5.3 Results and Discussion.....	98
5.3.1 Gas Diffusivities	98
5.3.2 Gas Solubility - Henry's Law Constant.....	101
5.3.3 Permeability and Selectivity Properties of Ionic Liquids	107
5.4 Conclusions	109
6. Conclusions and Proposed Future Work.....	111
6.1 Concluding Remarks	111

6.2 Proposed Future Work	113
Appendix A: Force Field Parameters for the [Tf ₂ N ⁺] Ionic Liquids	115
Appendix B: Force Field Parameters for the [TCM ⁺] Ionic Liquids.....	127
Appendix C: Force Field Parameters for Gasses	141
References	143

List of Tables

Table 2.1: Mass density calculations for the three ILs at different temperatures at 1 bar. In all cases, the statistical uncertainty is less than 0.001 gr/cm ³	31
Table 2.2: Thermal expansion coefficient, α_p , for the three ILs at different temperatures and 1 bar.	31
Table 2.3: Isothermal compressibility, k_T , for the three ILs at different temperatures and 1 bar.	32
Table 2.4: Mean decorrelation time, τ_c , for various bond vectors defined on [C ₄ mim ⁺][Tf ₂ N ⁻], [C ₈ mim ⁺][Tf ₂ N ⁻] and [C ₁₂ mim ⁺][Tf ₂ N ⁻], as calculated from the mKWW fit to the $P_2(t)$ data. Relaxation time for N1-N2 at 298.15 K for [C ₁₂ mim ⁺][Tf ₂ N ⁻] is too large to be accurately estimated by simulation.	40
Table 2.5: Mean decorrelation time, τ_c , for various torsion angles defined on [C ₄ mim ⁺][Tf ₂ N ⁻], [C ₈ mim ⁺][Tf ₂ N ⁻] and [C ₁₂ mim ⁺][Tf ₂ N ⁻], as calculated from the mKWW fit to the $P_\phi(t)$ data.	42
Table 2.6: Activation energies obtained from fitting an Arrhenius expression to the self diffusivities calculated by the Einstein relation.	46
Table 4.1: The conformers of [C ₄ mim ⁺][TCM ⁻] and their relative energies as calculated by Scienomics ²⁰³	76
Table 4.2: Simulation results for density and diffusivity of [C ₄ mim ⁺][TCM ⁻] at 298.15 K using the 4RC set of charges and modified Lennard-Jones parameters for the anion. The deviation from the experimental density is stated in the parenthesis. (Note that: $R_{min} = \sigma\sqrt{2}$).	78
Table 4.3: Simulation results for density and diffusivity of [C ₄ mim ⁺][TCM ⁻] at 298.15 K using the 4RC scaled at 0.65e ⁻ set of charges and modified Lennard-Jones parameters for the anion. The deviation from the experimental density is stated in the parenthesis.	79

Table 4.4: Optimized Lennard-Jones parameters for [TCM ⁻] anion and simulation results for [C ₄ mim ⁺][TCM ⁻] at 298.15 K and 363.14 K using charges from the 4RC procedure.....	80
Table 4.5: Optimized Lennard-Jones parameters for [TCM ⁻] anion and simulation results for [C ₄ mim ⁺][TCM ⁻] at 298.15 K and 363.14 K using charges from the ISO procedure.....	81
Table 5.1 Gas diffusivities in the [C _{<i>n</i>} mim ⁺][TF ₂ N ⁻], <i>n</i> = 4, 8, 12 at various temperatures.....	99
Table 5.2 Gas diffusivities in the [C _{<i>n</i>} mim ⁺][TCM ⁻], <i>n</i> = 2, 4, 8 at various temperatures.....	100
Table 5.3 Gas Henry's law constant for [C _{<i>n</i>} mim ⁺][TF ₂ N ⁻], <i>n</i> = 4, 8, 12 at various temperatures. Error bars have been calculated with the block averaging method.....	106
Table 5.4 Gas Henry's law constant for [C _{<i>n</i>} mim ⁺][TCM ⁻], <i>n</i> = 2, 4, 8 at various temperatures. Error bars have been calculated with the block averaging method.....	107
Table 5.5: Selectivities for [C _{<i>n</i>} mim ⁺][Tf ₂ N ⁻], <i>n</i> = 4, 8, 12 at 298.15 K and atmospheric pressure.....	109
Table 5.6: Selectivities for [C _{<i>n</i>} mim ⁺][TCM ⁻], <i>n</i> = 2, 4, 8 at 298.15 K and atmospheric pressure.	109
Table A1: Bond force constants (<i>k_b</i>) and equilibrium bond distances (<i>b₀</i>).....	116
Table A2: Bond angle bending parameters (<i>k_θ</i>) and equilibrium angles (<i>θ₀</i>).	117
Table A3: Dihedral angle parameters.	119
Table A4: Improper dihedral angle parameters.	121
Table A5: Lennard-Jones parameters. Note that $\sigma = \frac{R_{\min}}{\sqrt[6]{2}}$	121
Table A6: Partial Atomic Charges (<i>e</i>) from six minimum energy conformations of the ionic pairs.....	122

Table A7: Partial Atomic Charges (e^-) from six minimum energy conformations of the ionic pair uniformly scaled to $\pm 0.75e^-$ total ionic charge.....	124
Table A8: Mass density calculations for the three ILs at different temperatures and 1 bar using charges scaled to $\pm 0.75e^-$ total ionic charge. In all cases, the statistical uncertainty is less than 0.001.	126
Table A9: Anions' and cations' self-diffusion coefficients of the center of mass for the three ILs at different temperatures and 1 bar using charges scaled to $\pm 0.75e^-$ total ionic charge.	126
Table A10: Viscosity calculations for the three ILs at different temperatures and 1 bar using charges scaled to $\pm 0.75e^-$ total ionic charge.	126
Table B1: Charges for [TCM $^-$] anion calculated as isolated ion and averaged over multiple ion pair conformations.	128
Table B2: Charges for [C $_4$ mim $^+$] cation calculated as isolated ion and averaged over multiple ion pair conformations.	128
Table B3: Bond force constants (k_b) and equilibrium bond distances (b_0).	130
Table B4: Bond angle bending parameters (k_θ) and equilibrium angles (θ_0).	131
Table B5: Dihedral angle parameters.	133
Table B6: Improper dihedral angle parameters.	135
Table B7: Lennard-Jones parameters. Note that $\sigma = R_{\min} / \sqrt[6]{2}$ 136	
Table B8: Partial Atomic Charges (e^-) from isolated ions uniformly scaled to $\pm 0.7e^-$ total ionic charge.	137
Table B9: Mass density calculations for the three ILs at different temperatures and 1 bar. In all cases, the statistical uncertainty is less than 0.001.	138
Table B10: Anions' and cations' self-diffusion coefficients of the center of mass for the three ILs at different temperatures and 1 bar.	139

Table B11: Viscosity calculations for the three ILs at different temperatures and 1 bar.	139
Table C1: Bond force constants (k_b) and equilibrium bond distances (b_0).....	141
Table C2: Bond angle bending parameters (k_θ) and equilibrium angles (θ_0).	141
Table C3: Lennard-Jones parameters. Note that $\sigma = R_{\min} / \sqrt[6]{2}$	142
Table C4: Partial Atomic Charges (e^-).....	142

List of Figures

Figure 1.1: Ethylammonium nitrate ($[\text{EtNH}_3^+][\text{NO}_3^-]$), the first IL ever reported. 17

Figure 1.2: Commonly used cations: (a) 1-alkyl-3-methylimidazolium ($[\text{C}_n\text{mim}^+]$), (b) 1,1-dialkylpyrrolidinium ($[\text{C}_m\text{C}_n\text{pyr}^+]$), (c) 1-alkylpyridinium ($[\text{C}_n\text{py}^+]$), (d) tetraalkylphosphonium ($[\text{P}_{ijkl}^+]$), (e) tetraalkylammonium ($[\text{N}_{ijkl}^+]$), and commonly used anions: (f) bis(trifluoromethanesulfonyl)amide ($[\text{Tf}_2\text{N}^-]$), (g) trifluoromethanesulfonate ($[\text{TfO}^-]$), (h) tosylate ($[\text{OTos}^-]$), (i) alkylsulfates ($[\text{C}_n\text{OSO}_3^-]$), (j) dicyanamide ($[(\text{CN})_2\text{N}^-]$). 19

Figure 1.3: Applications incorporating ionic liquids. (Adapted from Ref. 121) 21

Figure 2.1: Ions (a) $[\text{C}_4\text{mim}^+]$, (b) $[\text{C}_8\text{mim}^+]$, (c) $[\text{C}_{12}\text{mim}^+]$ and (d) $[\text{Tf}_2\text{N}^-]$ and labelling of the atoms. 30

Figure 2.2: Radial distribution function $g(r)$ for the anion-anion (black), anion-cation (red) and cation-cation (green) center of mass of $[\text{C}_8\text{mim}^+][\text{Tf}_2\text{N}^-]$ at 398.15 K. 33

Figure 2.3: Radial distribution function $g(r)$ for the cation - anion centers of mass of the $[\text{C}_4\text{mim}^+][\text{Tf}_2\text{N}^-]$, $[\text{C}_8\text{mim}^+][\text{Tf}_2\text{N}^-]$ and $[\text{C}_{12}\text{mim}^+][\text{Tf}_2\text{N}^-]$ at 398.15 K. 33

Figure 2.4: Radial distribution function $g(r)$ between the terminal carbon atoms in the cation's alkyl chain of $[\text{C}_4\text{mim}^+][\text{Tf}_2\text{N}^-]$, $[\text{C}_8\text{mim}^+][\text{Tf}_2\text{N}^-]$ and $[\text{C}_{12}\text{mim}^+][\text{Tf}_2\text{N}^-]$ at 298.15 K. 34

Figure 2.5: Radial distribution function $g(r)$ between the C_2 carbon in the imidazolium ring and the S1, O2 and N4 in the anion of the $[\text{C}_{12}\text{mim}^+][\text{Tf}_2\text{N}^-]$ at 398.15 K. 35

Figure 2.6: Radial distribution function $g(r)$ between the C4 in the imidazolium ring and the N4 in the anion of the $[\text{C}_4\text{mim}^+][\text{Tf}_2\text{N}^-]$, $[\text{C}_8\text{mim}^+][\text{Tf}_2\text{N}^-]$ and $[\text{C}_{12}\text{mim}^+][\text{Tf}_2\text{N}^-]$ at 398.15 K. 36

Figure 2.7: Radial Angular Distribution Functions (RADF) for (a) $[\text{C}_4\text{mim}^+][\text{Tf}_2\text{N}^-]$, (b) $[\text{C}_8\text{mim}^+][\text{Tf}_2\text{N}^-]$ and (c) $[\text{C}_{12}\text{mim}^+][\text{Tf}_2\text{N}^-]$ at 298.15 K with r being the distance between the C2 carbon atom of the imidazolium ring and the N4 nitrogen atom of the

anion and θ is the angle formed by the main plain of the imidazolium ring and the vector \mathbf{r}37

Figure 2.8: Alkyl chain end-to-end distance distribution of the $[\text{C}_4\text{mim}^+][\text{Tf}_2\text{N}^-]$, $[\text{C}_8\text{mim}^+][\text{Tf}_2\text{N}^-]$ and $[\text{C}_{12}\text{mim}^+][\text{Tf}_2\text{N}^-]$ at 398.15 K.....38

Figure 2.9: Relaxation times of vectors between atoms of the $[\text{C}_{12}\text{mim}^+][\text{Tf}_2\text{N}^-]$ IL, plotted in logarithmic scale, as a function of the inverse temperature.....41

Figure 2.10: The $P_\varphi(t)$ function for the decorrelation of the torsion defined by the atoms42

N3 – C7 – C8 – C9 of $[\text{C}_4\text{mim}^+][\text{Tf}_2\text{N}^-]$, $[\text{C}_8\text{mim}^+][\text{Tf}_2\text{N}^-]$ and $[\text{C}_{12}\text{mim}^+][\text{Tf}_2\text{N}^-]$ at 298.15 K.....42

Figure 2.11: Self diffusion coefficients of (a) $[\text{C}_4\text{mim}^+][\text{Tf}_2\text{N}^-]$, (b) $[\text{C}_8\text{mim}^+][\text{Tf}_2\text{N}^-]$ and (c) $[\text{C}_{12}\text{mim}^+][\text{Tf}_2\text{N}^-]$ as calculated by Einstein (MSD) and Green-Kubo (VACF) expressions against experimental measurements^{207,218}44

Figure 2.12: Shear viscosity MD results for (a) $[\text{C}_4\text{mim}^+][\text{Tf}_2\text{N}^-]$ (experimental values from Ref. 198,207,221-222), (b) $[\text{C}_8\text{mim}^+][\text{Tf}_2\text{N}^-]$ (experimental values from Ref. 207,221) and (c) $[\text{C}_{12}\text{mim}^+][\text{Tf}_2\text{N}^-]$ (experimental values from Ref. 221).47

Figure 3.1: The Drude particles are attached to atoms with a harmonic spring of force constant k_D53

Figure 3.1: Self-diffusion coefficients of (a) the cation and (b) the anion of $[\text{C}_8\text{mim}^+][\text{TF}_2\text{N}^-]$ against experimental values²⁰⁷ using various charge schemes.....55

Figure 3.2: MD predictions for the density of $[\text{C}_n\text{mim}^+][\text{TF}_2\text{N}^-]$, $n = 4, 8, 12$. Full points correspond to the optimized force field (6RC scaled to $0.75e^-$), open points to previous calculations using the 6RC charge distribution and the lines are interpolation/extrapolation of experimental data for $[\text{C}_4\text{mim}^+][\text{TF}_2\text{N}^-]$ ¹¹⁻¹², $[\text{C}_8\text{mim}^+][\text{TF}_2\text{N}^-]$ ²⁰⁷ and $[\text{C}_{12}\text{mim}^+][\text{TF}_2\text{N}^-]$ ²³⁰.....56

Figure 3.3: Self-diffusion coefficients of the center of mass of anion (squares) and cation (circles) using the 6RC scaled $\pm 0.75e^-$ charge scheme (full points) for (a) $[\text{C}_4\text{mim}^+][\text{TF}_2\text{N}^-]$, (b) $[\text{C}_8\text{mim}^+][\text{TF}_2\text{N}^-]$ and (c) $[\text{C}_{12}\text{mim}^+][\text{TF}_2\text{N}^-]$ compared to

previous data, 6RC (open points), against experimental data for $[\text{C}_4\text{mim}^+][\text{Tf}_2\text{N}^-]$, $[\text{C}_8\text{mim}^+][\text{Tf}_2\text{N}^-]$ ²⁰⁷ (solid lines) and $[\text{C}_{12}\text{mim}^+][\text{Tf}_2\text{N}^-]$ ²¹⁸ (green points).57

Figure 3.4: Viscosity calculations using the optimized force field of the present work, 6RC scaled 0.75e⁻, (full circles) compared to data using the 6RC force field (open triangles) for (a) $[\text{C}_4\text{mim}^+][\text{Tf}_2\text{N}^-]$ against the experimental data^{14,207,221-222}, (b) $[\text{C}_8\text{mim}^+][\text{Tf}_2\text{N}^-]$ against the experimental data^{207,221} and (c) $[\text{C}_{12}\text{mim}^+][\text{Tf}_2\text{N}^-]$ against the experimental data²²¹.59

Figure 3.5: The directions along which the translational motion was analyzed for (a) the cation and (b) the anion.61

Figure 3.6: Mean square displacement (MSD) at 298.15 K calculated along the direction of the vectors NN, NNp, the normal to them vector and the alkyl tail for the cation and along the vectors SS, SS_p and the normal to them vector for the anion. (a) cation and (b) anion of $[\text{C}_4\text{mim}^+][\text{Tf}_2\text{N}^-]$, (c) cation and (d) anion of $[\text{C}_8\text{mim}^+][\text{Tf}_2\text{N}^-]$ and (e) cation and (f) anion of $[\text{C}_{12}\text{mim}^+][\text{Tf}_2\text{N}^-]$62

Figure 3.7: Mean square displacement (MSD) at 398.15 K analyzed in specific axes on the ions for (a) cation and (b) anion of $[\text{C}_4\text{mim}^+][\text{Tf}_2\text{N}^-]$63

Figure 3.8: Non-Gaussian parameter $\alpha_2(t)$ for (a) cation and (b) anion of $[\text{C}_4\text{mim}^+][\text{Tf}_2\text{N}^-]$, (c) cation and (d) anion of $[\text{C}_8\text{mim}^+][\text{Tf}_2\text{N}^-]$ and (e) cation and (f) anion of $[\text{C}_{12}\text{mim}^+][\text{Tf}_2\text{N}^-]$ calculated at 298.15 K.65

Figure 3.9: Mean square displacement (MSD) of the anion (full lines) and the cation (dotted lines) of $[\text{C}_{12}\text{mim}^+][\text{Tf}_2\text{N}^-]$ calculated at 298.15 K (black), 348.15 K (red) and 398.15 K (blue). The slope of the dotted green lines is equal to unity and indicates the Fickian regime.66

Figure 3.10: Self-part of the Van Hove function $G_s(r,t)$ at 298.15 K compared to the expected Gaussian distribution for (a) cation and (b) anion of $[\text{C}_4\text{mim}^+][\text{Tf}_2\text{N}^-]$, (c) cation and (d) anion of $[\text{C}_8\text{mim}^+][\text{Tf}_2\text{N}^-]$ and (e) cation and (f) anion of $[\text{C}_{12}\text{mim}^+][\text{Tf}_2\text{N}^-]$67

Figure 3.11: Self-part of the Van Hove function $G_s(r,t)$ at 398.15 K compared to the expected Gaussian distribution for the cation of $[\text{C}_4\text{mim}^+][\text{Tf}_2\text{N}^-]$68

Figure 3.12: Radial distribution functions between the centers of mass of dynamically distinguishable cations and anions calculated at 298.15 K for $t = 500$ ps. (a) $[\text{C}_4\text{mim}^+][\text{Tf}_2\text{N}^-]$, (b) $[\text{C}_8\text{mim}^+][\text{Tf}_2\text{N}^-]$ and (c) $[\text{C}_{12}\text{mim}^+][\text{Tf}_2\text{N}^-]$	69
Figure 3.13: Radial distribution functions at 298.15 K for $t = 500$ ps between the centers of mass of fast and slow anions of $[\text{C}_{12}\text{mim}^+][\text{Tf}_2\text{N}^-]$	70
Figure 3.14: Radial distribution functions at 298.15 K for $t = 500$ ps between the centers of mass of fast and slow cations of $[\text{C}_8\text{mim}^+][\text{Tf}_2\text{N}^-]$	71
Figure 3.15: Radial distribution functions between the centers of mass of fast cations and fast anions calculated at 298.15 K for $t = 10, 50, 100, 300$ and 1000 ps. (a) $[\text{C}_4\text{mim}^+][\text{Tf}_2\text{N}^-]$ and (b) $[\text{C}_8\text{mim}^+][\text{Tf}_2\text{N}^-]$	71
Figure 3.16: Radial distribution functions between the centers of mass of fast anions of $[\text{C}_4\text{mim}^+][\text{Tf}_2\text{N}^-]$ calculated at 298.15 K for $t = 10, 50, 100, 300$ and 1000 ps.	72
Figure 4.1: The labeling of the atoms of $[\text{TCM}]$	75
Figure 4.2: The structure of two pairs of $[\text{C}_4\text{mim}^+][\text{TCM}^-]$ with charges obtained quantum mechanically.	82
Figure 4.3: MD predictions for the density of $[\text{C}_n\text{mim}^+][\text{TCM}^-]$, $n = 2, 4, 8$ (full points). The lines with open points are experimental data for $[\text{C}_2\text{mim}^+][\text{TCM}^-]$ ^{107,237-238} , $[\text{C}_4\text{mim}^+][\text{TCM}^-]$ ^{16,107,239} and $[\text{C}_8\text{mim}^+][\text{TCM}^-]$ ¹⁰⁹	83
Figure 4.4: Radial distribution function $g(r)$ for the anion-anion (black), anion-cation (red) and cation-cation (green) center of mass of (a) $[\text{C}_2\text{mim}^+][\text{TCM}^-]$, (b) $[\text{C}_4\text{mim}^+][\text{TCM}^-]$ and (c) $[\text{C}_8\text{mim}^+][\text{TCM}^-]$ at 298.15 K.	84
Figure 4.5: Radial distribution function $g(r)$ between the terminal carbon atoms in the cation's alkyl chain of $[\text{C}_2\text{mim}^+][\text{TCM}^-]$ (black), $[\text{C}_4\text{mim}^+][\text{TCM}^-]$ (red) and $[\text{C}_8\text{mim}^+][\text{TCM}^-]$ (green) at 298.15 K.	85
Figure 4.6: Radial distribution function $g(r)$ between the C2 carbon of the cation's imidazolium ring and the NC nitrogen of the anion for $[\text{C}_2\text{mim}^+][\text{TCM}^-]$ (black), $[\text{C}_4\text{mim}^+][\text{TCM}^-]$ (red) and $[\text{C}_8\text{mim}^+][\text{TCM}^-]$ (green) at 298.15 K.	86

Figure 4.7: Radial distribution function $g(r)$ between the terminal carbon of the cation's alkyl tail and the central carbon CCM of the anion for $[\text{C}_2\text{mim}^+][\text{TCM}^-]$ (black), $[\text{C}_4\text{mim}^+][\text{TCM}^-]$ (red) and $[\text{C}_8\text{mim}^+][\text{TCM}^-]$ (green) at 298.15 K.86

Figure 4.8: Radial Angular Distribution Functions (RADF) for (a) $[\text{C}_2\text{mim}^+][\text{TCM}^-]$, (b) $[\text{C}_4\text{mim}^+][\text{TCM}^-]$ and (c) $[\text{C}_8\text{mim}^+][\text{TCM}^-]$ at 298.15 K with r being the distance between the C2 carbon atom of the imidazolium ring and the NC nitrogen atom of the anion and θ is the angle formed by the main plain of the imidazolium ring and the vector \mathbf{r}87

Figure 4.9: Radial Angular Distribution Functions (RADF) for (a) $[\text{C}_2\text{mim}^+][\text{TCM}^-]$, (b) $[\text{C}_4\text{mim}^+][\text{TCM}^-]$ and (c) $[\text{C}_8\text{mim}^+][\text{TCM}^-]$ at 298.15 K with r being the distance between the C2 carbon atom of the imidazolium ring and the NC nitrogen atom of the anion and θ is the angle formed by the main plain of the imidazolium ring and the main plane of the anion.88

Figure 4.10: Self-diffusion coefficients of the anion (circles) and the cation (squares) versus the atom of carbon atoms in the cation's alkyl tail as calculated at 298.15 K (black), 363.15 K (red) and 398.15 (blue). The open circles are the experimental measurements (see acknowledgments) of the cation's diffusivity at 298.15 K.89

Figure 4.11: Viscosity calculations from simulation (full points) as a function of temperature against experimental data (lines with open points) for (a) $[\text{C}_2\text{mim}^+][\text{TCM}^-]^{107,238,240}$, (b) $[\text{C}_4\text{mim}^+][\text{TCM}^-]^{107,239}$ and (c) $[\text{C}_5\text{mim}^+][\text{TCM}^-]^{109}$90

Figure 4.12: The vectors defined on the cation along which the translational motion of the center of mass was analyzed.91

Figure 4.13: Mean square displacement (MSD) at 298.15 K calculated along the direction of the cations' vectors NN (red), NNp (green), the normal to them vector (red) and the alkyl tail (blue) compared to the 1/3 of the total MSD of the center of mass for (a) $[\text{C}_2\text{mim}^+][\text{TCM}^-]$, (b) $[\text{C}_4\text{mim}^+][\text{TCM}^-]$ and (c) $[\text{C}_8\text{mim}^+][\text{TCM}^-]$92

Figure 4.14: Non-Gaussian parameter $\alpha_2(t)$ for the anion (black) and the cation (red) of $[\text{C}_4\text{mim}^+][\text{TCM}^-]$ calculated at 298.15 K.93

Figure 4.15: Radial distribution functions between the centers of mass of slow anions – slow cations (black), fast anions – fast cations (red) and fast – slow anions and cations (green) plotted against the total $g(r)$ (blue dotted line) as calculated without any discrimination on the dynamic nature of the ions. Calculated for $[\text{C}_4\text{mim}^+][\text{TCM}^-]$ at 298.15 K for $t = 500$ ps.	94
Figure 5.1: MD diffusivity of CO_2 as calculated for the $[\text{Tf}_2\text{N}^-]$ ILs plotted against experimental data ²⁴⁶⁻²⁵⁰	101
Figure 5.2: MD diffusivity of CO_2 as calculated for the $[\text{TCM}^-]$ ILs plotted against experimental data provided in the framework of IOLICAP project ¹⁹⁶	101
Figure 5.3: The mean value of μ^{ex}/KT as a function of the number of total insertions for the case of CO_2 in $[\text{C}_8\text{mim}^+][\text{TCM}^-]$ at 298.15 K.	103
Figure 5.4: Calculation of Henry's Law constants for CO_2 , CH_4 , Ar, N_2 and O_2 are plotted against temperature for (a) $[\text{C}_4\text{mim}^+][\text{Tf}_2\text{N}^-]$, (b) $[\text{C}_8\text{mim}^+][\text{Tf}_2\text{N}^-]$ and (c) $[\text{C}_{12}\text{mim}^+][\text{Tf}_2\text{N}^-]$. Experimental measurements for CO_2 and CH_4 in $[\text{C}_4\text{mim}^+][\text{Tf}_2\text{N}^-]$ ^{249,257} and for CO_2 in $[\text{C}_8\text{mim}^+][\text{Tf}_2\text{N}^-]$ ²⁵⁷ are also shown (open points).	104
Figure 5.5: Henry's Law constant for CO_2 , CH_4 , Ar, N_2 and O_2 are plotted against temperature for (a) $[\text{C}_2\text{mim}^+][\text{TCM}^-]$, (b) $[\text{C}_4\text{mim}^+][\text{TCM}^-]$ and (c) $[\text{C}_8\text{mim}^+][\text{TCM}^-]$. Experimental data ²⁵³ for CO_2 and N_2 are also plotted for comparison (open points).	105
Figure 5.6: Selectivity for the gas pairs CO_2/N_2 , CO_2/Ar , CO_2/CH_4 at room temperature and at atmospheric pressure of (a) $[\text{C}_n\text{mim}^+][\text{Tf}_2\text{N}^-]$, $n = 4, 8, 12$, and (b) $[\text{C}_n\text{mim}^+][\text{TCM}^-]$, $n = 2, 4, 8$. Experimental selectivities ²⁶⁰ of CO_2/N_2 and CO_2/CH_4 in $[\text{C}_n\text{mim}^+][\text{Tf}_2\text{N}^-]$ are also plotted.	108
Figure A1: Atomic labeling for (a) $[\text{C}_n\text{mim}^+]$, $n > 2$ and (b) $[\text{Tf}_2\text{N}^-]$	115
Figure B1: Atomic labeling for (a) $[\text{C}_n\text{mim}^+]$, $n > 2$ and (b) $[\text{C}_2\text{mim}^+]$ and (c) $[\text{TCM}^-]$	127
Figure C1: Labeling of the particles for (a) CO_2 , (b) N_2 , (c) O_2 , (d) Ar and, (e) CH_4	141

List of Symbols

D	diffusion coefficient [cm^2/s]
$g(r)$	radial distribution function
$g(r,\theta)$	radial angular distribution function
$G_s(\mathbf{r},t)$	the self-part of the van Hove function
$G_g(\mathbf{r},t)$	Gauss distribution
H	Henry's Law constant [MPa]
k_T	isothermal compressibility [$10^{-4}/\text{MPa}$]
$P_{\text{mKWW}}(t)$	modified Kohlrausch-Williams-Watts function
$P_\phi(t)$	torsion angle autocorrelation function
P	permeability [$\text{MPa}^{-1}\text{cm}^2/\text{s}$]
q	charge [e-]
\mathbf{r}	position [\AA]
R_e	end-to-end distance [\AA]
S	Solubility [$1/\text{MPa}$]
U	potential energy [kcal/mol]
\mathbf{v}	velocity [cm/s]

Greek letters

$\alpha_2(t)$	non-Gaussian parameter
α_p	isobaric thermal expansion coefficient [$10^{-4}/\text{K}$]
ε	energy of the well in the Lennard Jones potential [kcal/mol]
η	viscosity [$\text{Pa}\cdot\text{s}$]
ρ	density [gr/cm^3]
τ_c	relaxation time [ns]

Subscripts

n	denotes am the carbon atoms in the cationic alkyl chain
i, j	denotes a particle, a gas or an element of a pressure tensor

Chapter 1

Introduction

The term “ionic liquids” (ILs) refers to salts that are in the liquid phase at room temperature and, by convention, below 100 °C¹⁻². The anion can be inorganic or organic, while the cation is usually organic, symmetric or asymmetric and large leading thereby to lower melting temperatures than ordinary salts. Over the last two decades, ILs have attracted increasing interest for extended study aiming at their potential use in a broad range of applications due to the unique combination of a number of properties. One of their most important attributes is their negligible vapor pressure which results in minimal vapor emissions that makes them odorless, non-flammable and therefore, excellent candidates for use in “green chemistry” as environmentally friendly materials.

1.1 Characteristics and Properties of Ionic Liquids

The first IL was synthesized in 1914 by Paul Walden, who reported the characteristics of an IL with a melting point of 12 °C, namely the ethylammonium nitrate³ ([EtNH₃⁺][NO₃⁻]; see Figure 1.1). Walden synthesized [EtNH₃⁺][NO₃⁻] by neutralizing ethylamine with nitric acid. However, the systematic study of ILs initiated after 1990 and various new compounds were synthesized and characterized. The first work of this period was reported in 1992 by J. S. Wilkes and M. Zaworotko⁴ who synthesized and characterized two ILs based on the 1-ethyl-3-methylimidazolium cation ([C₂mim⁺]), namely [C₂mim⁺][BF₄⁻] and [C₂mim⁺][CH₃CO₂⁻]. During the same period E. I. Cooper and E. J. M. O’ Sullivan reported the synthesis of two 1-ethyl-3-methylimidazolium ILs, namely [C₂mim⁺][CF₃SO₃⁻] and [C₂mim⁺][CH₃SO₃⁻]⁵. In between the first report of Walden and the early 90’s only few studies and patents concerning ILs appeared in the literature. An informative outlook in the history of ILs can be found in Ref. 6.

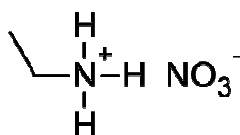


Figure 1.1: Ethylammonium nitrate ([EtNH₃⁺][NO₃⁻]), the first IL ever reported.

The synthesis of ILs generally comprises two steps. At first, the desired cation is synthesized and subsequently, an anion exchange procedure takes place in order to form the target IL. The various synthetic methods for ILs can be generally categorized into two groups: one based on metathesis reactions and another based on acid-based neutralization reactions⁷. The great interest in ILs has led to the optimization of the various synthetic methods in order to efficiently produce ILs in a laboratory or even in a larger scale. Additionally, the need for pure compounds has led to the design of improved purification methods and to the development of synthetic procedures that yield pure products. It is generally accepted that it is better to remove as many impurities as possible from the initial materials and use synthetic methods that produce as few side products as possible or allow them to be easily removed from the final IL. Extensive reports on the synthetic and purification methods of ILs can be found in the literature⁷⁻⁹.

The great number of anions and cations that can be combined leads to a plethora of possible IL structures. It has been estimated⁶ that if all the currently known anions and cations were to be paired it would result in almost 10^{12} ILs. This diversity in the chemical structure of ILs is also reflected to the vast variety in their physicochemical properties. A great number of experimental investigations^{1,10-35} have been conducted in order to measure a wide range of IL properties (volumetric, thermal, transport etc.). However, there is a particular interest in elucidating the link between the chemical structure of an IL and its properties since this knowledge will enable the tuning of the material's properties. For example, it has been reported⁷ that imidazolium-based ILs (see Figure 1.2a) have lower melting points than 1-alkylpyridinium ILs (see Figure 1.2c) and for this reason they are chosen as cations for many ILs.

Despite the diversity in the physicochemical properties of ILs there are some common characteristics in many IL families. It has been reported³⁶⁻³⁷, for example, that the liquid range of ILs is higher than the one of common molecular solvents. In comparison to molten salts, the ion pairing observed in ILs is weaker due to the reduced Coulomb interactions. This fact inhibits volatilization that requires tight ion pairing and results in very low vapor pressures compared to non-ionic solvents³⁶. This negligible vapor pressure results in having the upper limit of the liquid phase being that of thermal decomposition rather than vaporization³⁶.

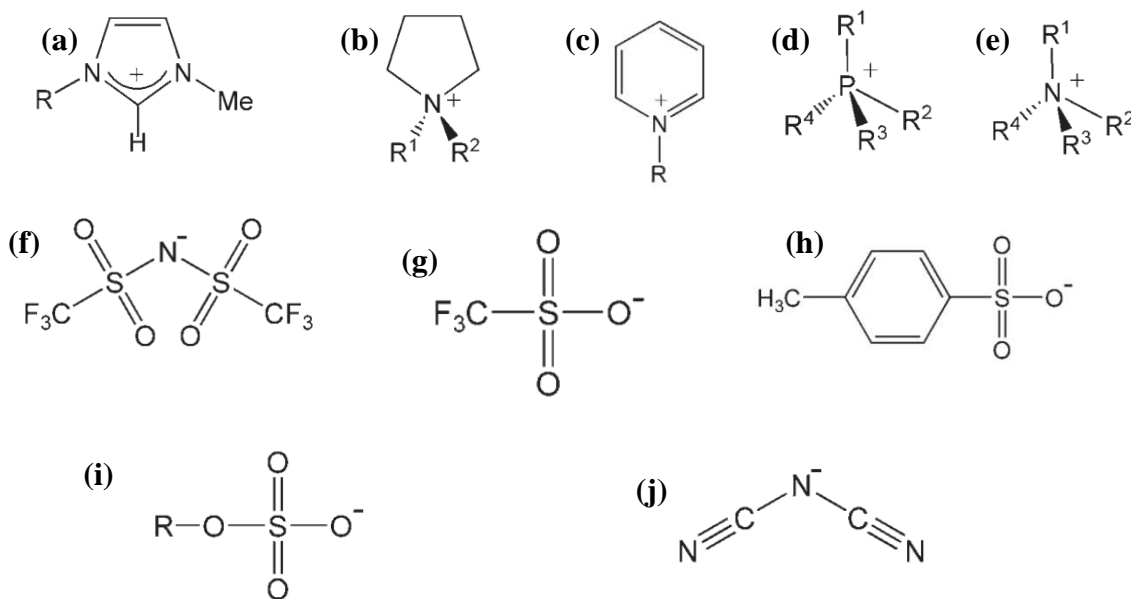


Figure 1.2: Commonly used cations: (a) 1-alkyl-3-methylimidazolium ($[C_n\text{mim}]^+$), (b) 1,1-dialkylpyrrolidinium ($[C_mC_n\text{pyr}]^+$), (c) 1-alkylpyridinium ($[C_n\text{py}]^+$), (d) tetraalkylphosphonium ($[P_{ijkl}]^+$), (e) tetraalkylammonium ($[N_{ijkl}]^+$), and commonly used anions: (f) bis(trifluoromethanesulfonyl)amide ($[\text{Tf}_2\text{N}]^-$), (g) trifluoromethane-sulfonate ($[\text{TfO}]^-$), (h) tosylate ($[\text{OTos}]^-$), (i) alkylsulfates ($[C_n\text{OSO}_3]^-$), (j) dicyanamide ($[(\text{CN})_2\text{N}]^-$).

The determination of the properties of ILs is crucial for their characterization and for their optimum utilization in many applications. Their microscopic structure is of great importance since it provides insight into the structural characteristics that control their macroscopic behaviour. The opposite charged ions have been found to be strongly correlated in space while they retain their spatial organization in long distances^{13,38-40} unlike simple molecular liquids. Additionally, microscopic heterogeneities that are reported in the literature⁴¹⁻⁴⁹ are considered to be the result of the interplay between the polar and the non-polar domains of the ions. For instance, in alkyl-methylimidazolium ILs the non-polar cationic alkyl tails are found to form clusters while the polar imidazolium rings and the anions are found to be strongly correlated forming a charged network. This phenomenon has been observed both experimentally⁴²⁻⁴³ and in simulation studies⁴⁴⁻⁴⁹ and has been attributed to the interplay between the Coulomb and the van der Waals interactions.

The dynamic behaviour of ILs has been reported to be much more complex compared to conventional fluids⁵⁰⁻⁵⁹. Their dynamics resembles the one of polymers,

especially at low temperatures where their behaviour is almost glassy-like, spanning a wide range of time scales for the relaxation of the various modes of the system. The viscosity of ILs is reported to be higher compared to simple liquids⁶⁰, thus limiting the possibility for their potential use in many industrial applications that involve mass transfer operations, pumping or mixing. The temperature dependence of viscosity deviates from the Arrhenius behaviour that simple liquids exhibit^{41,61} and is better represented by the Vogel-Fulcher-Tamman (VFT) equation. This deviation classifies ILs in the “fragile or intermediate glass formers” and not in the “strong glass formers” category of the Arrhenius type behaved liquids⁶². Dynamic heterogeneity phenomena, similar to the ones reported for glass-forming materials and super-cooled liquids⁶³⁻⁶⁹ have been observed in ILs both in experiments⁶⁹⁻⁷⁴ and in molecular simulations^{51-52,54-56,58,75-77}.

1.2 Applications of Ionic Liquids - Capture of CO₂

A number of important properties reported for ILs, such as their ability to dissolve organic and inorganic substances, the high thermal and electrochemical stability and the wide liquid temperature range, renders them ideal candidates for use in a plethora of applications^{1,6,61,78-86}: from electrochemistry and catalysis to separation processes and environmental engineering (see Figure 1.3). For instance, due to their high viscosity they are ideal candidates for lubrication applications^{37,87} while at the same time this inhibits their use in applications that involve mass transfer procedures. They are used in polymer science^{84,88-89} as polymerization media in various processes of polymerization or in biotechnological applications⁹⁰⁻⁹¹ like enzymatic biocatalysis. There are also a number of reports that focus on environmental applications that incorporate ILs. They are used in dye-sensitized solar cells^{83,92-106}, in applications for the capture of carbon dioxide (CO₂)¹⁰⁷⁻¹¹⁵, as dissolution media of wood biomass¹¹⁶⁻¹¹⁷ or in biomass pre-treatment procedures¹¹⁸. In particular, [TCM⁺] ILs that incorporate an imidazolium-based cation have been considered ideal for use in separation processes like CO₂ capture¹⁰⁷⁻¹⁰⁹ or aromatic/aliphatic separations¹¹⁹, as electrolytes in dye-sensitized solar cells⁹²⁻⁹⁷ or in batteries¹²⁰, as lubricants of hard coatings and ceramics⁸⁷.

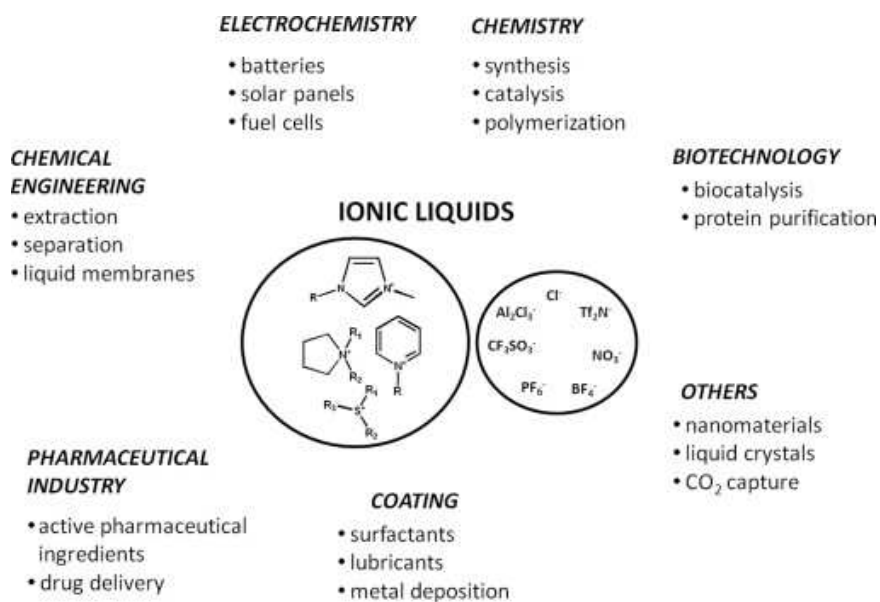


Figure 1.3: Applications incorporating ionic liquids. (Adapted from Ref. 121)

Carbon dioxide (CO₂) is the gas that is primarily responsible for the greenhouse effect. In most countries, its emissions are mainly attributed to power generation: it has been estimated¹¹⁰ that the 26% of the total CO₂ emissions (23 Gton-CO₂/year) is generated by the operation of coal-fired power plants. It is, therefore, of great importance to reduce these emissions in the most efficient possible way. Carbon capture and storage (CCS) technologies focus on the capture of CO₂ in the source of its emissions and then store it, for example, in the geosphere¹¹⁰, thus avoiding its emissions to the atmosphere. The most promising CCS technologies are being reviewed in detail in Refs. 111-112 while some recent reviews¹¹³⁻¹¹⁴ have focused solely on the use of ILs for carbon capture. These technologies can also be applied for the removal of CO₂ from natural gas since it is very important to expand the availability of clean-burning and efficient fuels, such as CH₄ or C₂H₆¹²²⁻¹²³.

The study of the permeability properties of ILs to various gases is, therefore, of great importance for the choice of the optimum IL for a gas separation process. For example, the post-combustion capture of CO₂ from a gas stream of a coal-fired power plant using an IL technology requires a compound with high CO₂ and low N₂ solubility and, thus, a high CO₂/N₂ selectivity^{112,124-125}.

1.3 Theoretical Studies of Ionic Liquids

For the design of task-specific ILs at the molecular level computational studies can play a vital role in establishing the link between the chemical structure and the

macroscopic properties of the material since its end-use performance directly depends on the molecular structure of the constituent ions^{10-11,41,126}. Additionally, computational studies can provide information for the behaviour of a system under extreme conditions where the experimental investigation of its properties is inhibited. Group contribution methods¹²⁷⁻¹³⁷, equations of state^{127-128,138-148} and molecular simulation^{44-45,47-48,51,149-162} have been widely used for the study of the properties of various families of ILs. At all cases, the cooperation among theory, simulation and experimental studies has been proven crucial for the understanding of the observed phenomena.

1.3.1 Molecular Simulation

Molecular simulation¹⁴⁹⁻¹⁵⁰ has been widely used^{44-45,47-48,51,152-160} so far to study the underlying molecular mechanisms that govern the macroscopic properties of ILs, giving insight into the microscopic behaviour that controls the experimentally observed phenomena. The reliability of the calculations from a molecular simulation study largely relies on the ability of the force field to accurately model the intra- and inter-molecular interactions. The vast majority of the molecular simulation studies have used all-atom force fields incorporating *ab initio* parameterization of single ions in the gas phase. Coarse-grained models have also been used to accelerate calculations and access longer length and time scales for the study of ILs¹⁶³⁻¹⁶⁴, whereas lately, the role of polarizability is being investigated^{159,165-166}.

It is well known that classical force fields with fixed partial charges and a total ionic charge equal to $\pm 1e^-$ underestimate the transport properties of ILs^{2,167-172}. One important conclusion drawn from simulation studies is that incorporating polarizability and charge transfer effects in the force field has a substantial influence on the calculated physical properties^{159,165-166,169,173-174} of ILs. Nevertheless, taking polarizability explicitly into account entails the use of a much more complicated simulation scheme and dramatically increases the required computational time. An alternative and much simpler approach that has been used widely in simulation studies of ILs^{51,59,152,173,175-181} is to use reduced total ionic charge. A very comprehensive review on this topic is given in Ref. 169.

1.3.2. Equations of State for Ionic Liquids

The first studies that have used equation of states (EoS) for the estimation of the properties of ILs were published in 2003¹⁸²⁻¹⁸³ and reported the performance of the

Peng-Robinson EoS¹⁸⁴ for the calculation of vapor-liquid (VLE) and solid-liquid (SLE) equilibria of various mixtures of imidazolium-based ILs with CO₂, CHF₃ and other organic solvents. Different EoSs have been used since then for the study of ILs, among which are the Redlich-Kwong¹⁸⁵, the non-random Lattice-fluid¹⁸⁶⁻¹⁸⁷, the square well chain fluid¹⁸⁸, the Cubic Plus Association (CPA)¹⁸⁹ and various versions of the statistical associating fluid theory (SAFT) EoS¹⁹⁰⁻¹⁹³.

Sophisticated extensions of the SAFT EoS have been proposed to account for the polar interactions. In 2001 the perturbed chain-SAFT (PC-SAFT)¹⁹⁴ was developed for a better representation of chain molecules through the incorporation of the chain-length dependence of the dispersive term. In 2005 Karakatsani *et al.*¹⁹⁵ proposed an extension of PC-SAFT to model the polar interactions, namely the polar PC-SAFT (PC-PSAFT). This model was very accurate but rather complicated for calculating the properties of real mixtures. For that, the truncated PC-PSAFT (tPC-PSAFT) was later proposed¹⁴⁵ where an adjustable parameter was incorporated in order to extend the range of the polar interactions beyond the first coordination shell of the polar molecule. In 2006 Kroon *et al.*¹⁴⁷ were the first to use a SAFT EoS and, more particular, the tPC-PCSAFT, for the calculation of the CO₂ solubility in imidazolium-based ILs. An detailed review of the various studies performed on ILs using equations of state is given in Ref. 138.

1.4 Motivation and Outline of the Thesis

The present work focuses on the study of six imidazolium-based ILs: three incorporating the anion bis(trifluoromethylsulfonyl) ([Tf₂N⁻]) and three incorporating the anion tricyanomethanide ([TCM⁻]). Imidazolium-based cations consist of an imidazolium ring and, in our case, one alkyl chain with n carbon atoms ($n = 2, 4, 8, 12$). Molecular dynamics (MD) simulations are performed in order to study the thermodynamic, structure, transport and permeability properties of these families of ILs in a wide temperature range and at atmospheric pressure.

The main goal of the present thesis is to use MD simulations to, firstly, investigate the properties of the pure ILs and then, study their permeability properties to gases that are present in the gas stream of a coal-fired power plant and most importantly, their capability to separate CO₂ which is primarily needed to be captured and not released to the atmosphere. Among the interests of this work is to study in

depth the effect of temperature, the anion and the cation's alkyl chain length on the properties of interest using well validated and good performing force fields in order to reassure the validity of the calculated properties.

The present thesis is comprised of four chapters and one concluding section. In Chapter 2, results from MD simulations of imidazolium-based $[\text{Tf}_2\text{N}^-]$ ILs are shown and the effect of the temperature and the cation's alkyl chain length is thoroughly investigated. More precisely, results concerning structural properties (radial distribution functions between the centers of mass of the ions and between individual sites, radial-angular distribution functions), thermodynamic properties (density, thermal expansion, isothermal compressibility), and dynamic properties (relaxation times of the reorientation of the bonds and the torsion angles, self-diffusion coefficients, shear viscosity) are presented as a function of the temperature and the cationic alkyl chain length.

In Chapter 3, the influence of polarization is investigated and a further optimized force field of the same $[\text{Tf}_2\text{N}^-]$ ILs is proposed and used for the calculation of thermodynamic, structure and transport properties improving the agreement with the experimental data. These new MD simulations have also been subject to a detailed analysis of dynamic heterogeneity phenomena that are studied through the calculation of the non-Gaussian parameter, the self-part of the van Hove function and the analysis of the anisotropy in the translational motion. Spatial correlations of dynamically distinguishable ions are also presented.

In Chapter 4, imidazolium-based ILs that incorporate the $[\text{TCM}^-]$ anion are studied. The lack of an optimized force field for this anion is being treated with the parameterization of a new atomistic force field based on experimental measurements of density and the cation's self-diffusion coefficient. The performance of the proposed force field is being validated at higher temperatures and for ILs with different cationic alkyl chain lengths. Results on density, structure and transport properties together with an analysis of the heterogeneous nature of the dynamics are also reported.

In Chapter 5, the permeability properties of the $[\text{Tf}_2\text{N}^-]$ and $[\text{TCM}^-]$ ILs to CO_2 , N_2 , CH_4 , Ar and O_2 are being studied through the calculation of gas solubility and diffusivity as calculated from new long MD simulations. Comparison between the selectivity of CO_2 over N_2 has been made in order to choose the most appropriate IL

for CO₂ capture. Simulation results presented in Chapter 5 are found to be in excellent agreement with experimental observations, and the [TCM] IL family has been identified as a very attractive candidate for use in gas separation procedures that will be directly used in a small-scale pilot plant within the European project IOLICAP – Novel Ionic LIquid and supported ionic liquid solvents for reversible CAPture of CO₂¹⁹⁶ (funded by the European Commission under the 7th Framework Programme for Research, Technology and Innovation).

Chapter 2

Structure, Thermodynamic and Transport Properties of Imidazolium-Based $[\text{Tf}_2\text{N}^-]$ Ionic Liquids

In the present chapter, ionic liquids (ILs) from the bis(trifluoromethylsulfonyl) imide ($[\text{Tf}_2\text{N}^-]$) family with n -alkyl methyl imidazolium-based cations ($[\text{C}_n\text{mim}^+]$) are studied using molecular simulation. These ILs have received significant attention both experimentally and computationally due to the fact that $[\text{Tf}_2\text{N}^-]$ has been selected by the International Union of Pure and Applied Chemistry (IUPAC) as a benchmark anion in ILs for extensive investigation.

Molecular dynamics (MD) simulations have been performed in order to investigate the behaviour of $[\text{C}_n\text{mim}^+][\text{Tf}_2\text{N}^-]$ ($n = 4, 8, 12$) ionic liquids in a wide temperature range (298.15 – 498.15 K) and at atmospheric pressure (1 bar). The partial charges for the classical molecular simulations were calculated with a previously developed methodology⁴⁵ which incorporates *ab initio* quantum mechanical calculations based on density functional theory (DFT). The wide range of time scales that characterize the segmental dynamics of these ILs, especially at low temperatures, requires very long MD simulations, in the order of several tens of nanoseconds, to reliably calculate the thermodynamic (density, thermal expansion, isothermal compressibility), structural (radial distribution functions between the centers of mass of ions and between individual sites, radial-angular distribution functions) and dynamic (relaxation times of the reorientation of the bonds and the torsion angles, self-diffusion coefficients, shear viscosity) properties. The influence of the alkyl chain length on the thermodynamic, structural and transport properties is thoroughly investigated. Moreover, the temperature effect is analyzed and the behaviour of these ILs is examined at high temperature conditions where no experimental data exist.

The calculated thermodynamic (primary and derivative) and structural properties are in good agreement with the experimental data, while the extremely sluggish dynamics renders the calculation of their transport properties a very complicated and challenging task, especially at low temperatures.

2.1 Simulation Details

Long MD simulations were performed in different thermodynamic ensembles at temperatures ranging from 298.15 to 498.15 K in 50 K increments and 1 bar pressure using NAMD¹⁹⁷. Each system consisted of 100 $[C_n\text{mim}^+][\text{Tf}_2\text{N}^-]$ ($n = 4, 8, 12$) ion pairs which were initially placed in a simulation box according to a target density. The value of the initial density used for each system was extracted from the experimental data, either directly when available, as for the case of $[C_4\text{mim}^+][\text{Tf}_2\text{N}^-]$ and $[C_8\text{mim}^+][\text{Tf}_2\text{N}^-]$ at 298.15 K¹¹⁻¹², or indirectly by interpolating and/or extrapolating the available data at various temperatures. For the case of $[C_{12}\text{mim}^+][\text{Tf}_2\text{N}^-]$ no experimental data were initially found in the literature, and so, a different approach was followed: first, all the experimental data for smaller alkyl chain lengths^{1,10-12,14-33,198-199} were gathered and for each alkyl chain length the values of the density at all desired temperatures were determined by extrapolating or interpolating the available experimental data. Afterwards, for each specific temperature under consideration the target density for $[C_{12}\text{mim}^+][\text{Tf}_2\text{N}^-]$ was calculated by extrapolating the existing data for smaller alkyl chain lengths.

The initial structures were built using the Rotational Isomeric State (RIS) model²⁰⁰ as modified by Theodorou and Suter²⁰¹⁻²⁰² available in MAPS²⁰³. Then, a 10^5 steps conjugate gradient energy minimization procedure was applied to eliminate the atomic overlaps and a 5 ns simulation in the canonical ensemble (NVT) was conducted in order to equilibrate the system. Subsequently, simulations in the isobaric-isothermal ensemble (NPT) of the order of 25 - 60 ns, depending on the system, were carried out to further equilibrate the system and the thermodynamic properties relevant to this ensemble were calculated using the last 15 - 30 ns of the NPT runs, having first adequately equilibrated the system. Next, a 10 - 20 ns NVT simulation was carried out in order to calculate the dynamic and structural properties of the system. Snapshots were stored every 1 ps during each simulation and the Lorentz-Berthelot mixing rules were used for unlike species. A Langevin piston method was used for the temperature control with a 5 ps^{-1} damping factor, while the Nosé-Hoover barostat was used for the pressure control with oscillation period equal to 200 fs and damping factor 100 fs.

Electrostatics were handled by means of particle-mesh Ewald method while the reversible reference system propagator algorithm (rRESPA)^{76,204} was used as a

multiple time step algorithm with a 1 fs reference time step in order to speed up the MD simulations. Short-range non-bonded van der Waals interactions were calculated every 2 fs, while full electrostatic interactions were computed every 4 fs. A cutoff distance of 12 Å was used to truncate the van der Waals interactions.

2.2 Force Field

The all-atom force field used to model the potential energy of the ILs under investigation is based on the following expression:

$$\begin{aligned}
 U = & \sum_{bonds} k_b (b - b_0)^2 + \sum_{angles} k_\theta (\theta - \theta_0)^2 + \sum_{dihedrals} \sum_{n=1}^4 k_\chi [1 + \cos(n\chi - \delta)] \\
 & + \sum_{impropers} k_\psi (\psi - \psi_0)^2 + \sum_{i=1}^{n-1} \sum_{j>i}^n \left\{ 4\epsilon_{ij} \left[\left(\frac{\sigma_{ij}}{r_{ij}} \right)^{12} - \left(\frac{\sigma_{ij}}{r_{ij}} \right)^6 \right] + \frac{q_i q_j}{4\epsilon_0 r_{ij}} \right\}
 \end{aligned} \tag{2.1}$$

where b , θ , χ and ψ denote bond length, bond angle, dihedral angle and improper angle respectively and the subscript “0” refers to the equilibrium values. Parameter n in the expression for the dihedral potential is the multiplicity of the dihedral angle while δ is the phase shift of the dihedral potential over the full range of rotation. Partial charges are denoted by q_i , while ϵ_0 is the vacuum permittivity and ϵ , σ the Lennard-Jones parameters. Bonded and Lennard-Jones parameters were obtained from Cadena and Maginn¹⁶⁷ and from Cadena *et al.*²⁰⁵ for the cations and Canongia Lopes and Pádua²⁰⁶ for the anion. For atoms separated by three covalent bonds, Coulomb interactions were scaled by a factor of 0.4 while Lennard-Jones interactions were fully included. The partial charges were derived from quantum calculations performed by Dr. Javier Ramos at Instituto de Estructura de la Matéria in Madrid, Spain on an isolated $[C_n\text{mim}^+][\text{Tf}_2\text{N}]$ ($n = 4, 8, 12$) ion pair using a Density Functional Theory (DFT) methodology according to which the atomic charges were calculated by taking into account the relative position and orientation of the anion with respect to the cation. For that, six minimum energy configurations of the ionic pair were used and the atomic charges at the different ionic pair conformations were calculated by electrostatic surface potential fits. More information on the procedure followed can be found in Refs. 45 and 59. Subsequently, the mean value of each atomic charge from the six different distributions was calculated and assigned to the cation’s atoms. An additional modification to the anion’s atomic charges was applied in order to preserve the symmetry of the anion by assigning to each group of

symmetric atoms the mean value of the charges estimated by the quantum mechanical calculations. All force field parameters can be found in Appendix A.

2.3. Results and Discussion

In this section the results for the thermodynamic, structural and transport properties as calculated from the MD simulations are presented. The chemical structure of the three ILs ions and the labeling of their atoms are shown in Figure 2.1.

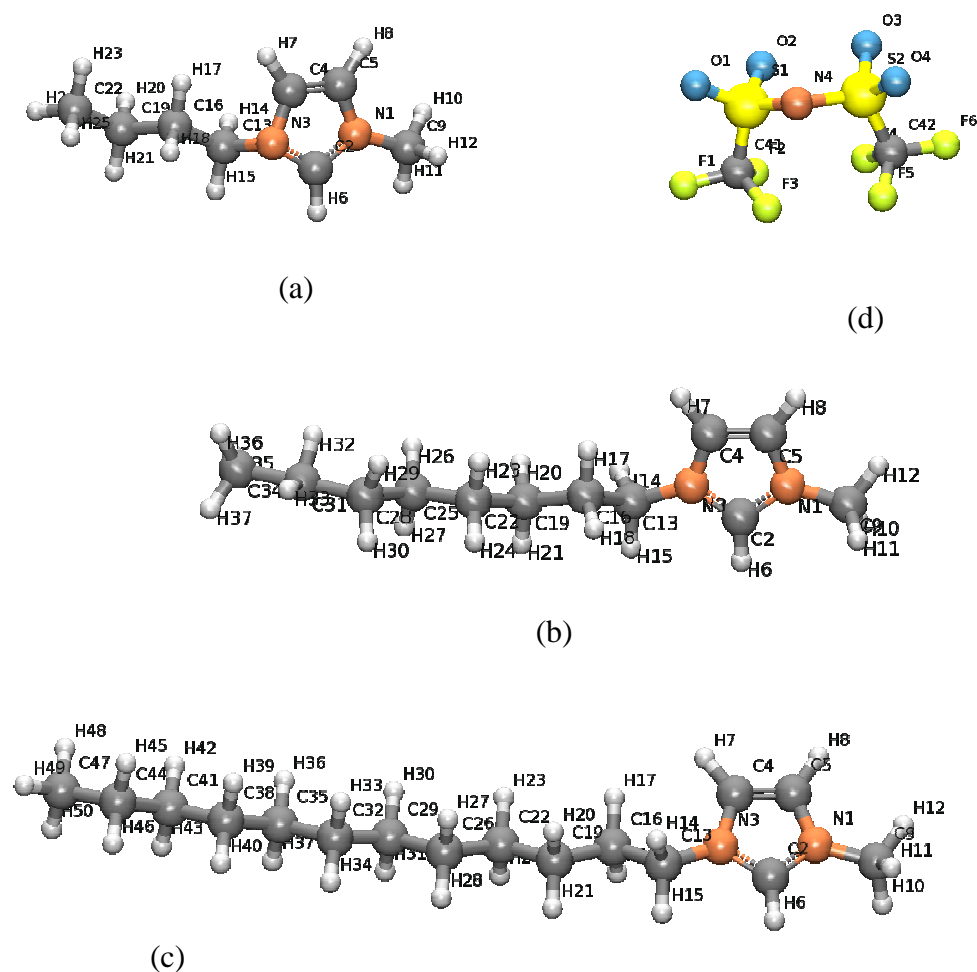


Figure 2.1: Ions (a) $[C_4mim]^+$, (b) $[C_8mim]^+$, (c) $[C_{12}mim]^+$ and (d) $[Tf_2N]^-$ and labelling of the atoms.

2.3.1. Thermodynamic Properties

In Table 2.1, MD calculations for the mass density of the three ILs at 1 bar are presented. Calculations resulted to less than 2% deviation from the available experimental measurements^{11-12,207} which are limited to 288.15 - 328.20 K for the

cases of $[\text{C}_4\text{mim}^+][\text{Tf}_2\text{N}^-]$ and $[\text{C}_8\text{mim}^+][\text{Tf}_2\text{N}^-]$. For a given temperature, the density decreases as the length of the alkyl chain in the cation increases.

Table 2.1: Mass density calculations for the three ILs at different temperatures at 1bar. In all cases, the statistical uncertainty is less than 0.001 gr/cm^3 .

$T \text{ (K)}$	mass density (gr/cm^3)		
	$[\text{C}_4\text{mim}^+][\text{Tf}_2\text{N}^-]$	$[\text{C}_8\text{mim}^+][\text{Tf}_2\text{N}^-]$	$[\text{C}_{12}\text{mim}^+][\text{Tf}_2\text{N}^-]$
298.15	1.461	1.331	1.250
348.15	1.406	1.278	1.205
398.15	1.354	1.228	1.158
448.15	1.303	1.180	1.113
498.15	1.252	1.131	1.068

Furthermore, MD data were used to calculate the isobaric thermal expansion coefficient, a_p , given by the expression:

$$a_p = \frac{1}{V} \left(\frac{\partial V}{\partial T} \right)_p = \frac{1}{\langle V \rangle} \left(\frac{\Delta \langle V \rangle}{\Delta T} \right)_p = \frac{\langle \delta V \delta H \rangle_{NPT}}{\langle V \rangle k_B T^2} \quad (2.2)$$

as well as the isothermal compressibility, k_T , through the expression:

$$k_T = -\frac{1}{V} \left(\frac{\partial V}{\partial P} \right)_T = -\frac{1}{\langle V \rangle} \left(\frac{\Delta \langle V \rangle}{\Delta P} \right)_T \quad (2.3)$$

In Tables 2.2 and 2.3 the estimated values of a_p and k_T for all ILs are shown. They exhibit less than 15% deviation, on average, from the available experimental data¹² for $[\text{C}_4\text{mim}^+][\text{Tf}_2\text{N}^-]$. No data have been found in the literature for $[\text{C}_8\text{mim}^+][\text{Tf}_2\text{N}^-]$ and $[\text{C}_{12}\text{mim}^+][\text{Tf}_2\text{N}^-]$.

Table 2.2: Thermal expansion coefficient, a_p , for the three ILs at different temperatures and 1 bar.

$T \text{ (K)}$	$a_p (10^{-4}/\text{K})$		
	$[\text{C}_4\text{mim}^+][\text{Tf}_2\text{N}^-]$	$[\text{C}_8\text{mim}^+][\text{Tf}_2\text{N}^-]$	$[\text{C}_{12}\text{mim}^+][\text{Tf}_2\text{N}^-]$
298.15	7.4 ₁	7.2 ₉	7.02 ₁
348.15	8.9 ₈	8.48 ₉	8.2 ₈
398.15	7.5 ₃	8.8 ₅	8.5 ₄
448.15	7.9 ₃	8.2 ₅	8.9 ₇
498.15	8.1 ₁	9.9 ₆	9.2 ₁

Table 2.3: Isothermal compressibility, k_T , for the three ILs at different temperatures and 1 bar.

T (K)	$k_T(10^{-4}/\text{MPa})$		
	$[\text{C}_4\text{mim}^+][\text{Tf}_2\text{N}^-]$	$[\text{C}_8\text{mim}^+][\text{Tf}_2\text{N}^-]$	$[\text{C}_{12}\text{mim}^+][\text{Tf}_2\text{N}^-]$
298.15	4.7 ₆	4.54 ₇	4.5 ₄
348.15	5.9 ₄	6.3 ₃	6.5 ₄
398.15	7.4 ₃	7.9 ₃	8.3 ₃
448.15	9.6 ₄	9.9 ₃	10.7 ₂
498.15	12.3 ₃	14.1 ₄	13.6 ₃

2.3.2. Microscopic Structure

The ions' organization in space was examined by means of radial distribution functions (RDFs) between the ions' centers-of-mass, as well as, between specific atoms of the ions. In Figure 2.2 the RDFs of the center-of-mass for anion-anion, cation-cation and cation-anion interactions for $[\text{C}_8\text{mim}^+][\text{Tf}_2\text{N}^-]$ at 398.15 K and 1 bar are shown. The anion-anion RDF exhibits a first peak at approximately 8 Å with a second, less intense peak appearing at 17 Å. The cation-anion RDF has a first maximum at around 5 Å and a second one, less intense at 12.5 Å, while the cation-cation RDF exhibits one small but broad maximum at 10 Å. In all three ILs, the ions are found to retain their spatial organization at longer distances compared to ordinary molecular liquids. The comparison of the three RDFs reveals a stronger cation-anion interaction which is attributed to the ions' opposite charges. This is also observed for $[\text{C}_4\text{mim}^+][\text{Tf}_2\text{N}^-]$ but becomes less evident in the case of $[\text{C}_{12}\text{mim}^+][\text{Tf}_2\text{N}^-]$ a fact that can be attributed to the existence of additional neutral parts in the system as the alkyl tail becomes longer. This behaviour has been reported for a number of ILs both in experimental^{13,38-40} and simulation studies^{54,152,167,205,208-210}.

In Figure 2.3 the anion-cation RDF is plotted for the three ILs at 398.15 K. A drop in the value of the first maximum is observed as the alkyl chain becomes longer while the second and less intense maximum tends to disappear. Additionally, a longer alkyl chain causes a higher delocalization to the cation's center of mass and an increase in the distance where the maximum value appears. Changing the temperature does not significantly affect the RDFs between the ions' centers of mass, apart from 298.15 K where some characteristics of the RDFs are more pronounced. More

specific, at 298.15 K the maximums of all RDFs are found at shorter distances and have higher values, indicating a more intense ionic spatial organization.

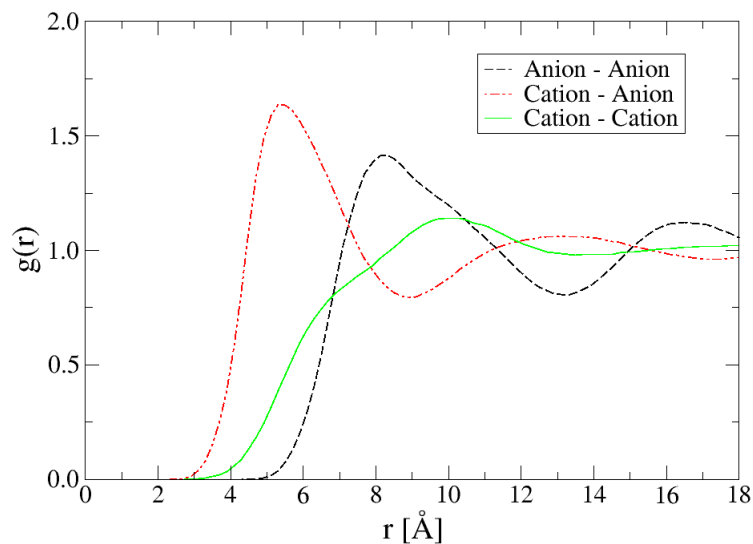


Figure 2.2: Radial distribution function $g(r)$ for the anion-anion (black), anion-cation (red) and cation-cation (green) center of mass of $[\text{C}_8\text{mim}^+][\text{Tf}_2\text{N}^-]$ at 398.15 K.

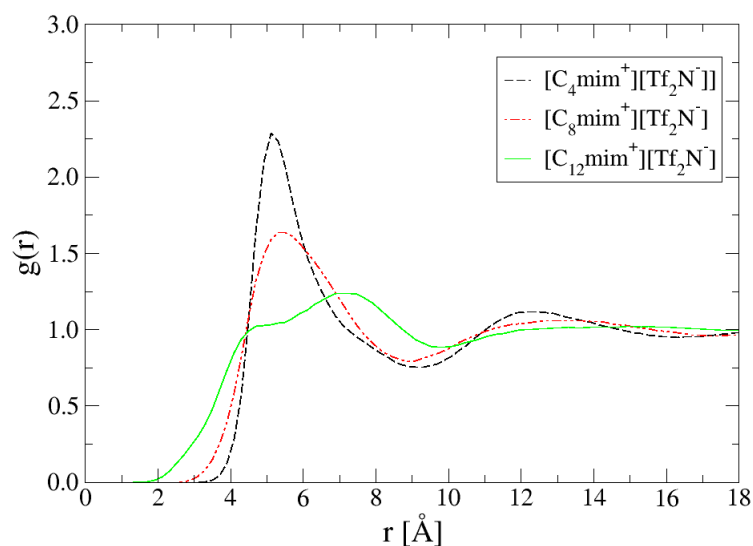


Figure 2.3: Radial distribution function $g(r)$ for the cation - anion centers of mass of the $[\text{C}_4\text{mim}^+][\text{Tf}_2\text{N}^-]$, $[\text{C}_8\text{mim}^+][\text{Tf}_2\text{N}^-]$ and $[\text{C}_{12}\text{mim}^+][\text{Tf}_2\text{N}^-]$ at 398.15 K.

A more detailed insight into the liquid bulk structure can be obtained from RDFs between specific sites of the ions. In Figure 2.4, the RDFs between the terminal carbon atoms of the alkyl chain for each IL at 298.15 K and 1 bar are shown. For all ILs there is a first peak at approximately 4.5 Å and a second one that starts to appear at around 8.5 Å as the alkyl chain becomes longer. The temperature increase results in a drop in the value of the first maximum while the second one is less affected. Interestingly enough, the intensity of the first peak increases as the alkyl chain becomes longer although it always appears at the same distance. This indicates that the almost neutrally charged and non-polar alkyl chains tend to aggregate and form domains while the charged groups of the cations and the anions create a charged network by retaining their structures up to long distances, a trend that has been reported in previous studies on similar systems⁴⁴⁻⁴⁹. An appropriate mechanism to explain this behaviour has been suggested by Wang *et al.*⁴⁹ and is based on the co-existence of competing electrostatic and van der Waals interactions in the ILs that dominate different parts of the ILs. Electrostatic interactions are long-ranged and strong, so the charged groups retain their local structures and form continuous charged domains. On the other hand, in the non-polar regions of the ILs, i.e. the almost neutral cationic alkyl chain, the short ranged van der Waals interactions are dominant thus leading to the tail aggregation phenomena.

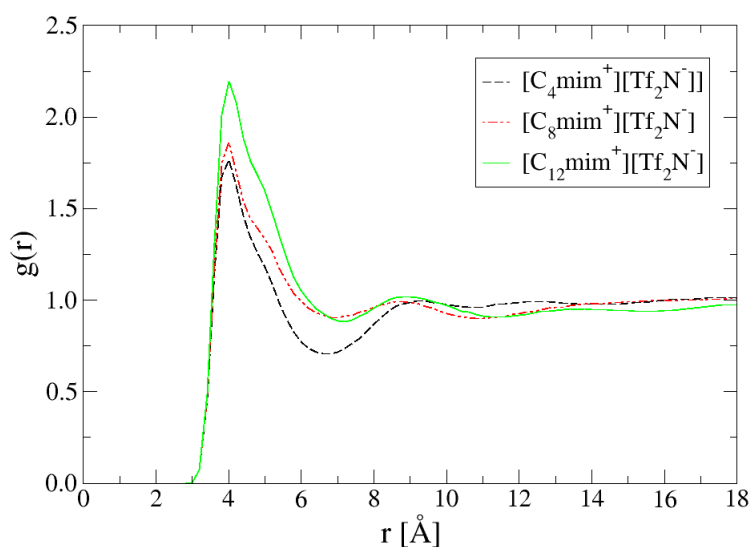


Figure 2.4: Radial distribution function $g(r)$ between the terminal carbon atoms in the cation's alkyl chain of $[C_4mim^+][Tf_2N^-]$, $[C_8mim^+][Tf_2N^-]$ and $[C_{12}mim^+][Tf_2N^-]$ at 298.15 K.

Detailed analysis of the relative configurations of the polar groups, i.e. the anions and the imidazolium rings, can be obtained based on RDFs between specific atoms in these groups. The RDFs between the carbon atoms C2 and C4 on the imidazolium and the atoms S1, O2 and N4 of the anion have been calculated. In Figure 2.5, the RDFs between the C2 carbon on the imidazolium ring and the S1, O2 and N4 of the anion of the $[\text{C}_{12}\text{mim}^+][\text{Tf}_2\text{N}^-]$ at 398.15 K and 1 bar are shown. The C2-O2 RDF has a first peak at around 2.5 Å and a less intense one at around 5 Å. Since O2 is covalently bonded to S1 with a double bond, the RDF between C2 and S1 is of similar form to that of the C2-O2 pair with the first peak appearing at slightly longer distances (4 Å) and the second one much less intense at approximately 6.5 Å. The C2-N4 RDF has a first peak at around 3 Å and a second peak at around 5 Å.

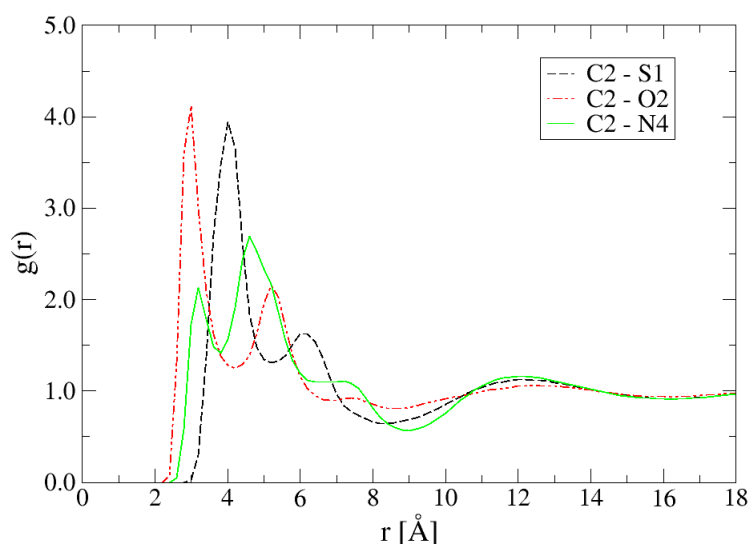


Figure 2.5: Radial distribution function $g(r)$ between the C₂ carbon in the imidazolium ring and the S1, O2 and N4 in the anion of the $[\text{C}_{12}\text{mim}^+][\text{Tf}_2\text{N}^-]$ at 398.15 K.

The RDF between C2-N4 indicates that at small distances, where O2 or S1 are most likely to be found close to the C2 carbon atom, N4 can be found anywhere between 3 – 6 Å as the value of RDF at these distances is higher than one. Nevertheless, the two peaks show that there are preferable relative positions and the peak at 3 Å may be indicative of a configuration where the N4 nitrogen of the anion comes close to the C2 carbon atom on the imidazolium ring, while the second and more intense peak may correspond to the most probable case where the O2 and S1 atoms are closer to the C2 carbon. The nitrogen N4, which is covalently bonded to S1, is mostly found to a longer distance.

The RDFs between the C4 and the O2, S1, N4 of the anion at all ILs highlight this preferential conformation between the C2 and the above mentioned anion atoms. An example of such RDFs is shown in Figure 2.6 where the RDFs between the C4 on the imidazolium ring and the N4 of the anion of the $[\text{C}_4\text{mim}^+][\text{Tf}_2\text{N}^-]$, $[\text{C}_8\text{mim}^+][\text{Tf}_2\text{N}^-]$ and $[\text{C}_{12}\text{mim}^+][\text{Tf}_2\text{N}^-]$ at 398.15 K and 1 bar are shown. For all ILs there is one peak that appears at approximately 5 Å and becomes more intense as the alkyl chain length increases.

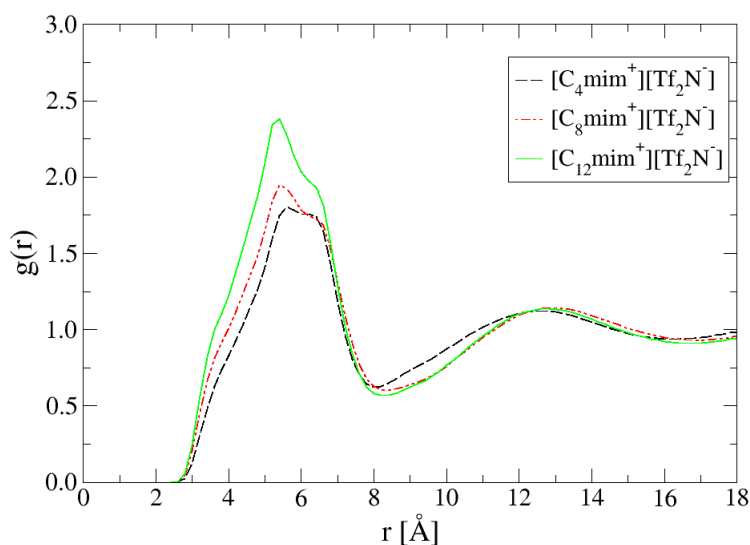


Figure 2.6: Radial distribution function $g(r)$ between the C4 in the imidazolium ring and the N4 in the anion of the $[\text{C}_4\text{mim}^+][\text{Tf}_2\text{N}^-]$, $[\text{C}_8\text{mim}^+][\text{Tf}_2\text{N}^-]$ and $[\text{C}_{12}\text{mim}^+][\text{Tf}_2\text{N}^-]$ at 398.15 K.

Additional information on the microscopic structure of ILs can be obtained from the calculation of three-dimensional radial-angular distribution functions (RADF). In Figures 2.7a, 2.7b and 2.7c the RADFs between the C2 carbon atom of the imidazolium ring and the N4 nitrogen of the anion for the three ILs are shown. The angle θ is the angle formed by the main plain of the imidazolium ring and the vector that connects the atoms C2 and N4. At all cases, the main peaks appear at about 4-5 Å and at symmetrical positions above and below the plain of the imidazolium ring. A second peak is also observed at around 7-8 Å and at 0° angle for all ILs. Extra RADFs calculated measuring the distance between the geometrical center of the imidazolium ring and the N4 nitrogen of the anion indicate that this second peak corresponds to the case where the N4 nitrogen of the anion lies on the

plane of the imidazolium ring but is situated not close to the C2 carbon atom but on the other side of the imidazolium ring, that is, closer to the C4 and C5 carbon atoms.

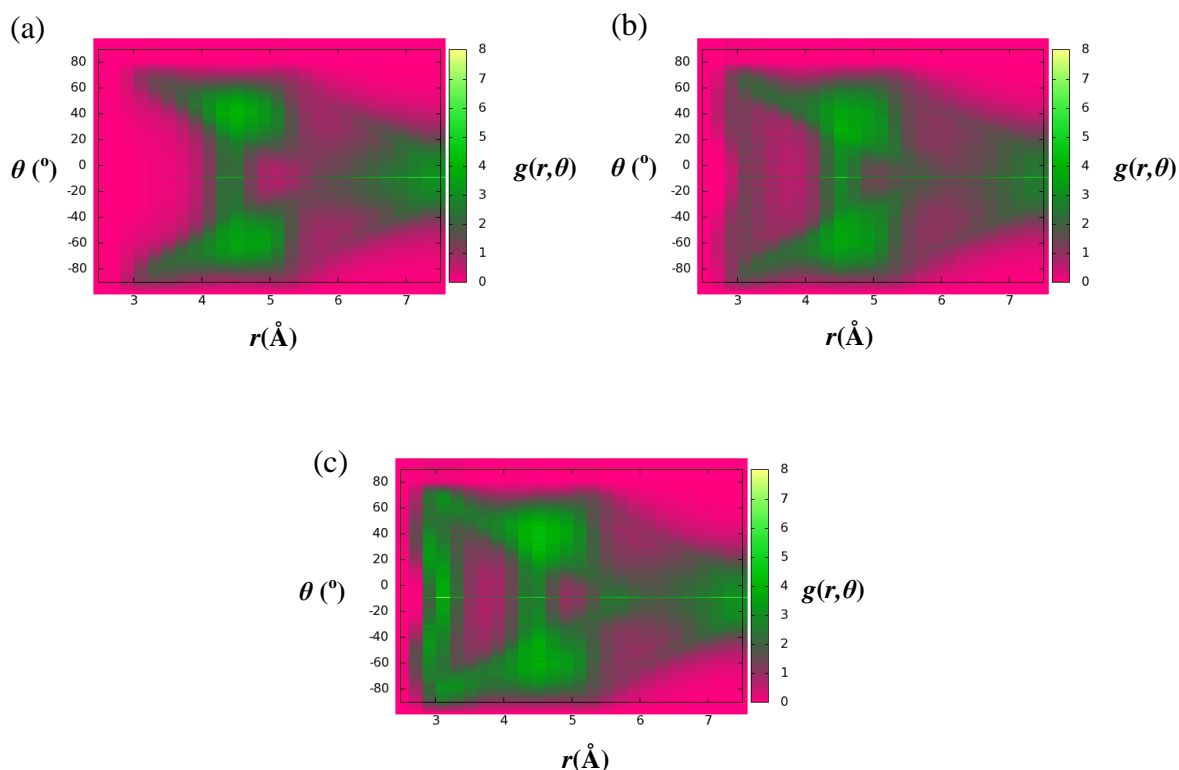


Figure 2.7: Radial Angular Distribution Functions (RADF) for (a) $[\text{C}_4\text{mim}^+][\text{Tf}_2\text{N}^-]$, (b) $[\text{C}_8\text{mim}^+][\text{Tf}_2\text{N}^-]$ and (c) $[\text{C}_{12}\text{mim}^+][\text{Tf}_2\text{N}^-]$ at 298.15 K with r being the distance between the C2 carbon atom of the imidazolium ring and the N4 nitrogen atom of the anion and θ is the angle formed by the main plain of the imidazolium ring and the vector \mathbf{r} .

For the case of the longest alkyl chain, i.e. the $[\text{C}_{12}\text{mim}^+][\text{Tf}_2\text{N}^-]$ IL, there is also a third peak appearing in shorter distances, at about 3 Å, which spans over almost the whole range of θ . This is consistent with the results obtained from the RDFs between the terminal carbon atoms of the cationic alkyl chain where the most intense peak in the RDFs corresponded to the IL with the longest cationic alkyl chain (Figure 2.4). These two findings clearly confirm that as the alkyl chain becomes longer not only do the non-polar alkyl tail groups come closer but also the anion approaches the imidazolium ring and, more precisely, the C2 carbon atom. Generally, a temperature increase resulted in a small decrease in the maximum values of all atom-atom RDFs and RADFs studied with no particular change to the overall spatial organization of the ions.

Insight into the conformations of the cationic alkyl chains can be obtained from the calculation of the distribution of the end-to-end distance R_e . This was chosen to be calculated as the distance between the geometric center of the imidazolium ring and the terminal carbon atom of the alkyl chain. In Figure 2.8 the distribution of the end-to-end distance for each IL at 398.15 K and at 1 bar is shown. The end-to-end distance distribution for each IL is a right-shifted normal distribution with the variance around the mean value becoming higher as the alkyl chain becomes longer indicating that a longer alkyl chain is more flexible. Temperature increase systematically decreases the mean value of the end-to-end distance and increases the variance around the mean value. These data were fit to the expression:

$$\langle R_e^2 \rangle \propto N^{2\nu} \quad (2.4)$$

where N is the number of carbon atoms of the alkyl chain and ν is was found equal to 0.74, 0.76 and 0.8 for $T = 298.15$, 398.15 and 498.15 K respectively, and are in very good agreement with simulation calculations for low molecular weight alkanes²¹¹⁻²¹².

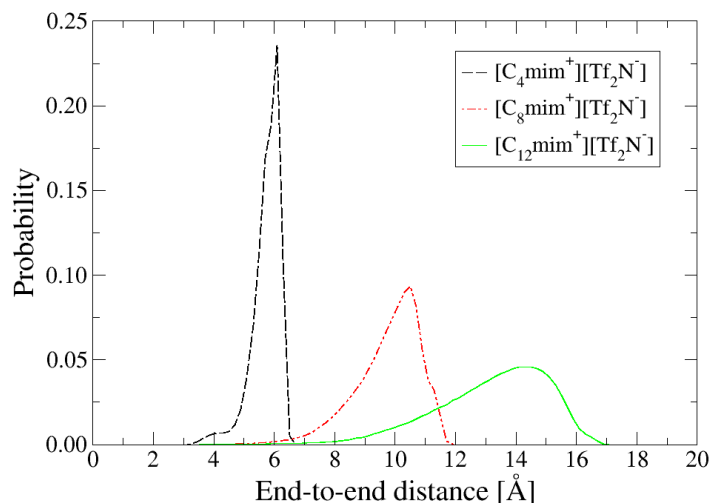


Figure 2.8: Alkyl chain end-to-end distance distribution of the $[C_4mim^+][Tf_2N^-]$, $[C_8mim^+][Tf_2N^-]$ and $[C_{12}mim^+][Tf_2N^-]$ at 398.15 K.

2.3.3 Segmental Dynamics

The local dynamics was examined through the estimation of the decorrelation of the orientation of various vectors defined by atoms on the ions as well as through

torsion angle decorrelation. The reorientation of vectors is quantified by a second-order autocorrelation function of the form²¹³:

$$P_2(t) = \frac{1}{2} \left\{ 3 \left\langle \left[\mathbf{u}_{\alpha\beta}(t) \cdot \mathbf{u}_{\alpha\beta}(0) \right]^2 \right\rangle - 1 \right\} \quad (2.5)$$

where $\mathbf{u}_{\alpha\beta}(t)$ is the unit vector along the vector under study at time t . The calculated data indicate that there is a large deviation in the decorrelation rates of different vectors defined by atoms of the cation and the anion. The vectors defined by atoms close to the imidazolium ring, such as N1-N3 and N1-C6, are found to decorrelate much slower than vectors defined by atoms at the end of the cation's alkyl chain due to the higher flexibility of the alkyl chain compared to the bonds attached to the imidazolium ring. In the anion, the bond that connects atoms C42 and S2 also decorrelates much faster than the vector defined by atoms S1 and S2 as can be seen from the different rates with which their $P_2(t)$ function decays to zero. These behaviours are observed in all three ILs. Temperature has a strong impact on the rates of decorrelation of all vectors: as the temperature increases there is a significant increase on the decorrelation rate of all vectors defined on the ions, even for the stiffest ones as the one defined by the N1 and N3 atoms of the imidazolium ring.

These observations can be quantified by calculating the mean decorrelation time τ_c of each vector under study, defined by integrating the $P_2(t)$ function which can accurately be described by the modified Kohlrausch-Williams-Watts (mKWW) function²¹⁴:

$$P_{mKWW}(t) = \alpha \exp \left[- \left(\frac{t}{\tau_0} \right) \right] + (1 - \alpha) \exp \left[- \left(\frac{t}{\tau_{KWW}} \right)^\beta \right] \quad (2.6)$$

The mKWW function consists of two terms. The first describes a fast exponential decay with characteristic time τ_0 and amplitude α that is associated with small perturbations of torsion angles around skeletal bonds and with the bond and bond-angle bending vibrations of skeletal and pendent bonds around their equilibrium values. The second term is a slower stretching exponential decay (KWW) associated with cooperative conformational transitions in the ions, with τ_{KWW} being the characteristic correlation time and β the stretching exponent. By fitting the MD data

of $P_2(t)$ to the $P_{mKWW}(t)$ function one can calculate the mean decorrelation time τ_C through the expression:

$$\tau_C = \int_0^\infty P_2(t)dt = \int_0^\infty P_{mKWW}(t)dt = \alpha\tau_0 + (1+\alpha)\tau_{KWW} \frac{1}{\beta} \Gamma\left(\frac{1}{\beta}\right) \quad (2.7)$$

The calculated relaxations times τ_C for various vectors in the ILs at each temperature are reported in Table 2.4. It is also quantitatively evident that vectors defined by atoms near the imidazolium ring are much stiffer than others defined by atoms at the end of the alkyl chain. This behaviour is observed at all temperatures whereas it is more intense at the two lower temperatures, 298.15 and 348.15 K. In Figure 2.9 the values of τ_C for various vectors defined by atoms on the $[C_{12}mim^+][Tf_2N^-]$ are plotted in logarithmic scale versus the inverse of the temperature. Figure 2.9 clearly demonstrates the wide range of relaxation times that characterizes the segmental dynamics of these ILs, especially at room temperature.

Table 2.4: Mean decorrelation time, τ_c , for various bond vectors defined on $[C_4mim^+][Tf_2N^-]$, $[C_8mim^+][Tf_2N^-]$ and $[C_{12}mim^+][Tf_2N^-]$, as calculated from the mKWW fit to the $P_2(t)$ data.

Relaxation time for N1-N2 at 298.15 K for $[C_{12}mim^+][Tf_2N^-]$ is too large to be accurately estimated by simulation.

Bond Vector	τ_c (ns)				
	298.15 K	348.15 K	398.15 K	448.15 K	498.15 K
$[C_4mim^+][Tf_2N^-]$					
N1 – N3	12.7	0.644	0.161	0.069	0.038
N3 – C7	48.1	0.572	0.142	0.062	0.034
C9 – C10	1.03	0.055	0.017	0.0062	0.0035
S1 - S2	4.03	0.432	0.108	0.044	0.027
$[C_8mim^+][Tf_2N^-]$					
N1 – N3	98.42	0.907	0.209	0.082	0.050
N3 – C7	8.674	0.667	0.201	0.078	0.047
C13 – C14	0.423	0.068	0.018	0.0071	0.0040
S1 - S2	1.543	0.292	0.078	0.035	0.020
$[C_{12}mim^+][Tf_2N^-]$					
N1 – N3	-	3.9	0.5	0.2	0.08
N3 – C7	24.7	1.6	0.5	0.2	0.08
C17 – C18	1.1	0.2	0.03	0.009	0.004
S1 - S2	6.2	0.7	0.2	0.07	0.04

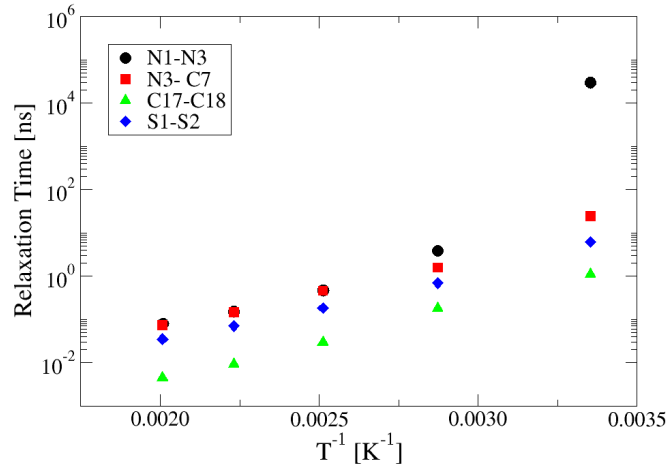


Figure 2.9: Relaxation times of vectors between atoms of the $[C_{12}mim^+][Tf_2N^-]$ IL, plotted in logarithmic scale, as a function of the inverse temperature.

Additionally, the decorrelation of the torsional angles can be studied using the autocorrelation function defined as²¹⁵:

$$P_{\varphi}(t) = \frac{\langle \cos(\varphi(t)) \cos(\varphi(0)) \rangle - \langle \cos(\varphi(0)) \rangle^2}{\langle \cos(\varphi(0))^2 \rangle - \langle \cos(\varphi(0)) \rangle^2} \quad (2.8)$$

where $\varphi(t)$ is the value of the torsional angle at time t . As expected from the analysis on the decorrelation of the vectors' orientation, torsion angles at the end of the cationic alkyl chain decorrelate much faster than the ones defined near the imidazolium ring. The $P_{\varphi}(t)$ data can be represented by the mKWW function and the mean correlation time τ_c for the torsional motion can also be calculated from Eq. 2.7. In Table 2.5, the mean decorrelation times for torsion angles close to the imidazolium ring and at the end of the alkyl chain are reported for all ILs. As expected, the mean decorrelation times reported for the torsion defined near the imidazolium ring are higher than the ones for the torsion defined by the terminal atoms of the alkyl chain. As the alkyl chain becomes longer, the τ_c of the stiffest torsion which is closer to the imidazolium ring increases in contrast to the terminal torsion of the alkyl tail that relaxes faster (see Figure 2.10).

Temperature has an important impact on the torsion decorrelation rate: the higher the temperature the faster the torsional decorrelation rate and, for that, the mean relaxation time decreases as can be seen in Table 2.5. The time scale separation

that governs the segmental dynamics of ILs at low temperatures has been observed both in experimental and simulation studies and resembles the complex dynamical behaviour of polymeric systems^{214,216-217}.

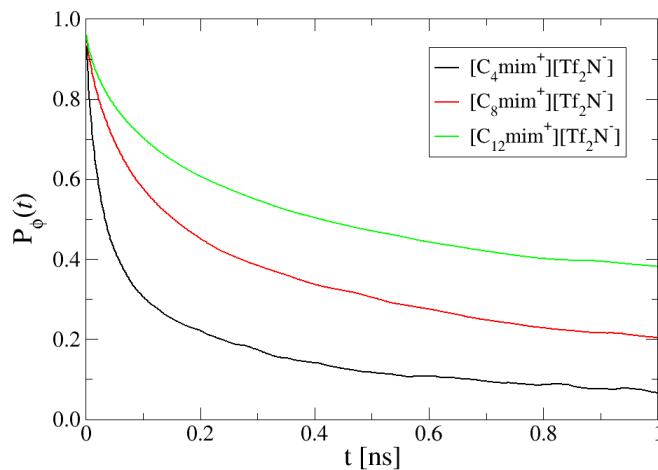


Figure 2.10: The $P_\phi(t)$ function for the decorrelation of the torsion defined by the atoms N3 – C7 – C8 – C9 of $[\text{C}_4\text{mim}^+][\text{Tf}_2\text{N}^-]$, $[\text{C}_8\text{mim}^+][\text{Tf}_2\text{N}^-]$ and $[\text{C}_{12}\text{mim}^+][\text{Tf}_2\text{N}^-]$ at 298.15 K.

Table 2.5: Mean decorrelation time, τ_c , for various torsion angles defined on $[\text{C}_4\text{mim}^+][\text{Tf}_2\text{N}^-]$, $[\text{C}_8\text{mim}^+][\text{Tf}_2\text{N}^-]$ and $[\text{C}_{12}\text{mim}^+][\text{Tf}_2\text{N}^-]$, as calculated from the mKWW fit to the $P_\phi(t)$ data.

Torsion Angle	τ_c (ns)				
	298.15 K	348.15 K	398.15 K	448.15 K	498.15 K
$[\text{C}_4\text{mim}^+][\text{Tf}_2\text{N}^-]$					
N3-C7-C8-C9	0.21	0.05	0.02	0.008	0.005
C7-C8-C9- C10	0.24	0.03	0.01	0.007	0.004
$[\text{C}_8\text{mim}^+][\text{Tf}_2\text{N}^-]$					
N3-C7-C8-C9	1.8	0.1	0.04	0.02	0.01
C11-C12-C13- C14	0.1	0.03	0.01	0.007	0.007
$[\text{C}_{12}\text{mim}^+][\text{Tf}_2\text{N}^-]$					
N3-C7-C8-C9	2.6	0.3	0.07	0.04	0.02
C15-C16-C17- C18	0.2	0.03	0.01	0.006	0.004

2.3.4. Self-Diffusion Coefficients

The self-diffusivity of the ions can be calculated by the Einstein relation:

$$D = \frac{1}{6} \lim_{t \rightarrow \infty} \frac{d}{dt} \left\langle \left| \mathbf{r}_i(t) - \mathbf{r}_i(0) \right|^2 \right\rangle \quad (2.9)$$

where $\mathbf{r}_i(t)$ is the position of the i -th ion's center of mass at time t and the brackets denote the mean-square displacement (MSD) over the ions' centers of mass. Equation 2.9 is valid only when the diffusivity is in the Fickian regime which can be identified by the slope being equal to unity in a $\log(\text{MSD})$ versus $\log(t)$ plot. ILs have much more complex dynamics than conventional fluids due to the different timescales that are involved in the local dynamics as shown in the previous section. Due to this, extremely long MD simulations are required to reach the Fickian regime, especially at low temperatures. In short timescales of ballistic motion, the slope is higher than unity, while in intermediate times ILs exhibit glass-like behaviour and the slope in that regime is less than unity.

The calculated diffusivities for the three ILs, $[\text{C}_4\text{mim}^+][\text{Tf}_2\text{N}^-]$, $[\text{C}_8\text{mim}^+][\text{Tf}_2\text{N}^-]$ and $[\text{C}_{12}\text{mim}^+][\text{Tf}_2\text{N}^-]$ are shown in Figures 2.11a, 2.11b and 2.11c respectively as a function of temperature. Additionally, experimental measurements^{207,218} in the temperature range 263 – 353 K are also shown. The cation's self-diffusion coefficients are higher than the anion's for $[\text{C}_4\text{mim}^+][\text{Tf}_2\text{N}^-]$ and $[\text{C}_8\text{mim}^+][\text{Tf}_2\text{N}^-]$ at all temperatures being in agreement with observations reported for most imidazolium-based ILs both from experiment³⁴⁻³⁵ and from simulation^{2,51,53,152,219-220}. The increase of the alkyl chain length leads to a reduced cationic mobility and to smaller differences in the ions' self-diffusivities so that in the case of $[\text{C}_{12}\text{mim}^+][\text{Tf}_2\text{N}^-]$ the two ions have comparable self-diffusion coefficients (see Figure 2.11c). This can be partially attributed to the interplay between the weights of the counterions as the mass of $[\text{Tf}_2\text{N}^-]$ is 280.1469 amu, while $[\text{C}_{12}\text{mim}^+]$ weights 251.4295 amu.

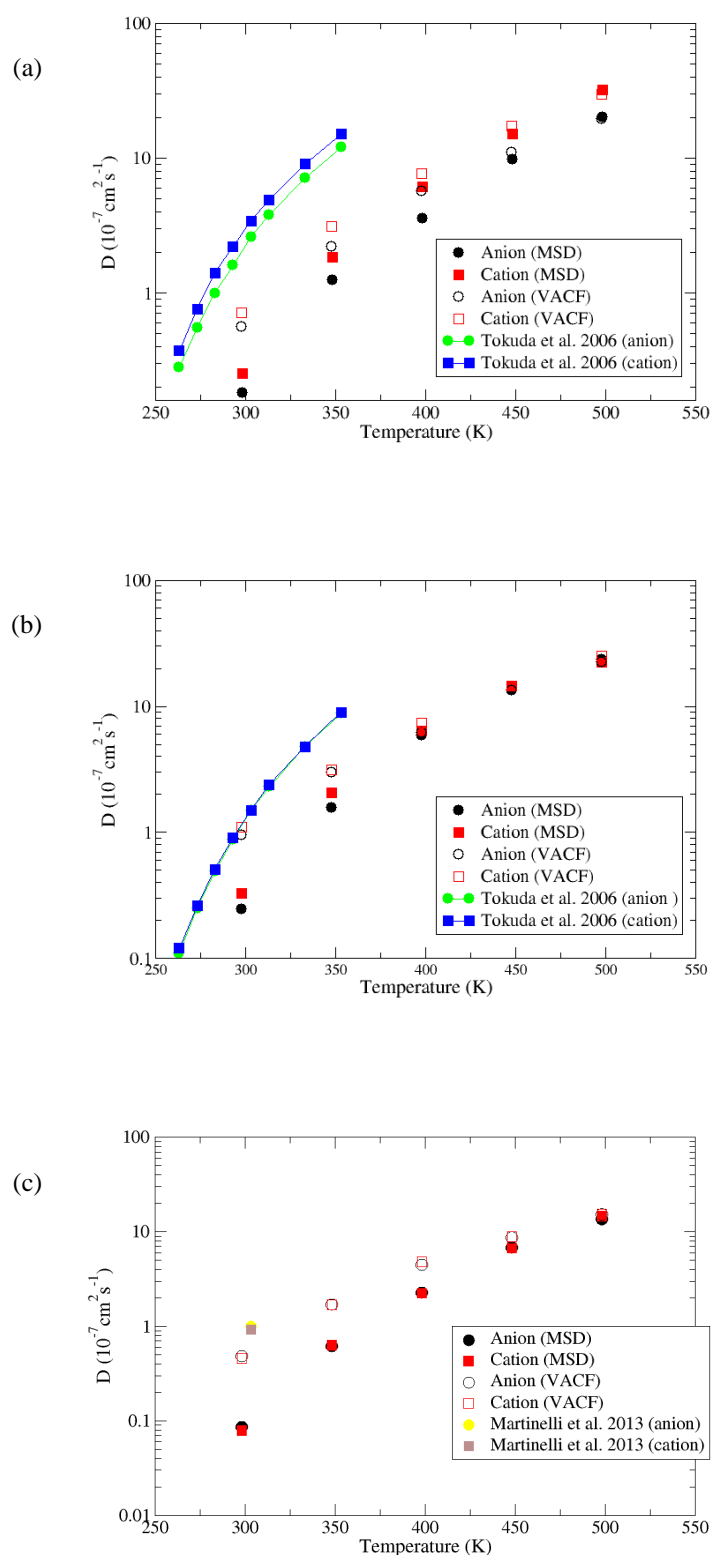


Figure 2.11: Self diffusion coefficients of (a) $[\text{C}_4\text{mim}^+][\text{Tf}_2\text{N}^-]$, (b) $[\text{C}_8\text{mim}^+][\text{Tf}_2\text{N}^-]$ and (c) $[\text{C}_{12}\text{mim}^+][\text{Tf}_2\text{N}^-]$ as calculated by Einstein (MSD) and Green-Kubo (VACF) expressions against experimental measurements^{207,218}.

The self-diffusion coefficients calculated from MD for all ILs were underestimated at low temperatures compared to the experimental values^{207,218}, a problem that is generally reported in most classical molecular simulation studies^{2,51,170,205}. The lack of experimental data at higher temperatures hinders the verification of the predicted values.

The self-diffusion coefficients were also calculated using the Green-Kubo formula:

$$D = \frac{1}{3} \int_0^\infty dt \langle \mathbf{v}_i(t) \cdot \mathbf{v}_i(0) \rangle \quad (2.10)$$

where $\mathbf{v}_i(t)$ is the velocity of the center of mass of the i -ion at time t and the term inside the brackets is the velocity autocorrelation function (VACF). The self-diffusion coefficients for each IL at every temperature were calculated using the last 2 ns of each trajectory with the information on velocity being stored every 10 fs. The self-diffusion coefficients obtained from the Green-Kubo method are systematically higher than the ones calculated using the Einstein relation with the difference between the two methods being larger at low temperatures (Figures 2.11a, 2.11b and 2.11c). Although Green-Kubo diffusivity coefficients appear to be closer to the experimental values at low temperatures, results obtained from the Einstein relation are considered more reliable as the Green Kubo method is more prone to errors in cases of systems with complex local dynamics and modes of motion that take place in a wide range of time scales^{2,53}. The values obtained from the two methods progressively converge for all ILs as the temperature increases possibly due to the fact that as the temperature increases the time scale separation phenomenon is no longer present in the segmental dynamics.

Diffusivity calculations using the Einstein relation were used to calculate the activation energies for diffusion shown in Table 2.6 by fitting to an Arrhenius expression. The activation energy for the anion is greater than the one of the cation as expected by the values of diffusivity from MD, being in agreement to activation energy calculations reported in the literature^{10-11,51}.

Table 2.6: Activation energies obtained from fitting an Arrhenius expression to the self diffusivities calculated by the Einstein relation.

	Activation energy (kJ mol ⁻¹)	
	E_{D-}	E_{D+}
[C ₄ mim ⁺][Tf ₂ N ⁻]	30.0	29.1
[C ₈ mim ⁺][Tf ₂ N ⁻]	28.9	28.3
[C ₁₂ mim ⁺][Tf ₂ N ⁻]	33.3	32.7

2.3.5. Shear Viscosity

Calculations of the shear viscosity were performed using the following Green-Kubo relation:

$$\eta = \frac{V}{k_B T} \int_0^\infty dt \langle P_{ij}(t) \cdot P_{ij}(0) \rangle \quad (2.11)$$

where $P_{ij}(t)$ is the ij -element of the pressure tensor at time t ($i \neq j$). The shear viscosity is a collective quantity and its calculation is prone to errors due to the sensitivity of the stress correlation function to the intra-molecular vibrational modes. The stress correlation function was integrated at the last section of each productive run during which the information of the pressure was stored each 8 fs and the viscosity was estimated by an integral plateau value. In Figures 2.12a, 2.12b and 2.12c the values for the viscosity are plotted for [C₄mim⁺][Tf₂N⁻], [C₈mim⁺][Tf₂N⁻] and [C₁₂mim⁺][Tf₂N⁻] respectively and are compared to experimental data^{198,207,221-222}. No value of the shear viscosity was included for [C₁₂mim⁺][Tf₂N⁻] at 298.15 K as the integral of the pressure tensor autocorrelation function failed to reach a smooth plateau at that temperature. As expected, simulation overestimates viscosity being consistent with the underestimation on calculated diffusivities; whereas the temperature dependence of viscosity reproduces rather well the experimental results for all ILs.

The fact that molecular simulation underestimates diffusivity and overestimates viscosity at low temperatures may be attributed to the fixed atomic charges that cause formation of long-living cages in order to achieve charge neutrality

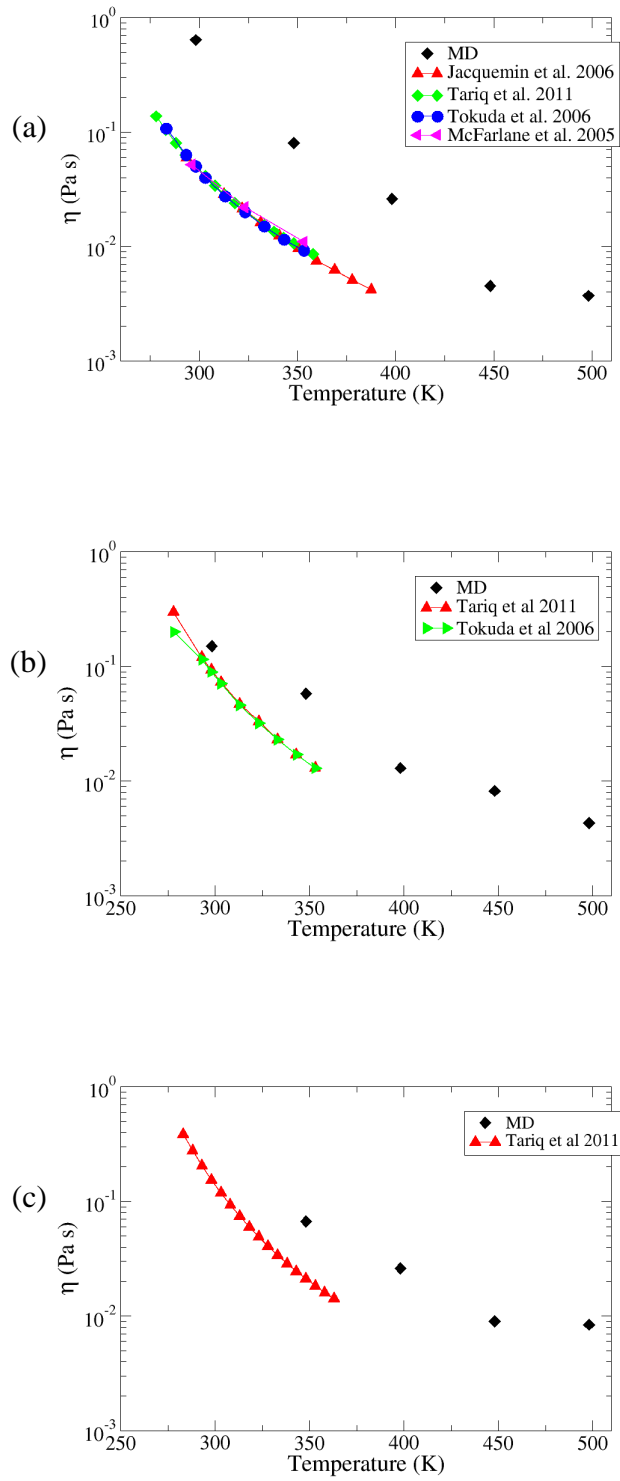


Figure 2.12: Shear viscosity MD results for (a) $[C_4mim^+][Tf_2N^-]$ (experimental values from Ref. 198,207,221-222), (b) $[C_8mim^+][Tf_2N^-]$ (experimental values from Ref. 207,221) and (c) $[C_{12}mim^+][Tf_2N^-]$ (experimental values from Ref. 221).

among groups of ions which results in a slower dynamics⁴⁹. It is proposed^{159,165-166} that taking into account polarizability effects leads to better low-temperature predictions of transport properties in comparison to experimental values.

2.4 Conclusions

Long MD simulations of several tens of nanoseconds, were performed at a wide temperature range, from 298.15 to 498.15 K with 50 K increments, and at atmospheric pressure in order to study the thermodynamic (density, thermal expansion, isothermal compressibility), structural (radial distribution functions between the centers of mass of ions and radial distribution functions between different sites of the ions, radial-angular distribution functions, end-to-end distance distributions) and dynamic (relaxation times in segmental dynamics, self-diffusion coefficients, shear viscosity) properties of the imidazolium-based ILs, namely [C₄mim⁺][Tf₂N⁻], [C₈mim⁺][Tf₂N⁻] and [C₁₂mim⁺][Tf₂N⁻]. The temperature effect was thoroughly studied, as well as, the influence of the anion and the cation's alkyl chain's length in the properties under investigation.

A wealth of information on the microscopic mechanisms that govern the spatial organization and the dynamical behaviour of these systems was revealed. The calculated radial distribution and radial-angular distribution functions between the ions' centers of mass reveal that ILs exhibit organization at much longer distances than conventional liquids with the anion-cation interaction being stronger than the other two interactions at all temperatures. There is clear indication of alkyl tail aggregation which becomes more evident for the longer alkyl chain lengths, while the anions were found to localize near the cation's imidazolium ring where the positive charge is located. The dynamics of these ILs were found to be extremely sluggish as indicated by the wide range of relaxation times that characterize their segmental dynamics, a fact that makes the calculation of their transport properties a very complicated task, especially at low temperatures, while the lack of experimental data at high temperatures hinders the verification of molecular simulation diffusivity predictions. However, molecular simulation results of viscosity were consistent with the ones for diffusivity and the temperature dependence of these properties was captured well. Optimization of existing force fields or development of new ones that will effectively incorporate the polarizability of the systems is expected to improve

the agreement between experimental data and simulations for the transport properties of ionic liquids, especially at low temperatures.

Chapter 3

Analysis of the Heterogeneous Dynamics of Imidazolium-Based [Tf₂N⁻] Ionic Liquids and Prediction of their Transport Properties Using a Further Optimized Force Field

In the present chapter, the force field for imidazolium-based [Tf₂N⁻] that was used in Chapter 2 is optimized in order to attain good agreement with the experimental data for the transport properties of [C_{*n*}mim⁺][Tf₂N⁻], *n* = 4, 8, 12. The effect of charge transfer and polarizability in the transport properties is investigated and two different ways to incorporate polarizability are being tested. The Drude polarizable model is implemented and compared to results obtained by simulations performed using charge distributions scaled to lower total ionic charges. Furthermore, new results on densities, ion self-diffusivities and viscosities are reported and the complex dynamics of these systems is analyzed using an optimized force field. The ions' translational motion is analysed into specific axes dictated by their geometry, and anisotropy in the diffusion is detected for both ions. The heterogeneity in the dynamics is thoroughly investigated by calculating the non-Gaussian parameter and the self-part of the Van Hove function. Ions that move faster or slower than expected are being detected through deviations from the normal distribution, while these dynamically distinguishable ions are found to be strongly spatially correlated. The effect of the temperature and the alkyl chain length on the above properties is examined in depth.

3.1 Simulation Details

Long MD simulations of 100 [C_{*n*}mim⁺][Tf₂N⁻] (*n* = 4, 8, 12) ion pairs were performed at 298.15 K, 348.15 K and 398.15 K and atmospheric pressure using NAMD software¹⁹⁷. The initial configuration for each run was the last snapshot of the well equilibrated trajectories (~80 ns) of Chapter 2. At first, a 15-25 ns simulation in the isobaric-isothermal ensemble (NPT) was performed in order to relax the system and calculate the density. Subsequently, simulations in the canonical ensemble (NVT) of the order of 20-40 ns -depending on the energy equilibration- were performed at the mean density obtained from the NPT simulations, in order to calculate the transport properties. Snapshots were stored every 1 ps during each simulation. The

Lorentz-Berthelot mixing rules were used to calculate the force field parameters between unlike atoms. A Langevin piston was used to control temperature with a 5 ps^{-1} damping factor and the Nosé-Hoover barostat was used for the pressure control with oscillation period equal to 200 fs and a damping factor of 100 fs.

Electrostatics were handled by means of particle-mesh Ewald method while the reversible reference system propagator algorithm (rRESPA^{76,204}) was used as a multiple time step algorithm with a 1 fs reference time step in order to speed up the MD simulations. Short-range non-bonded van der Waals interactions were calculated every 2 fs and full electrostatic interactions were computed every 4 fs. A cutoff distance of 12 Å was used to truncate the van der Waals interactions using a switching function beyond 10.5 Å. A long-range correction was applied to the system's energy and virial to account for the neglected van der Waals forces due to switching and cutoff of the Lennard-Jones potential.

3.2 Force Field Optimization

The formalism of the all-atom force field used to model the potential energy of the systems is given by Eq. 2.1. Bonded and Lennard-Jones parameters were obtained from Cadena and Maginn¹⁶⁷ and from Cadena *et al.*²⁰⁵ for the cations and Canongia Lopes and Pádua²⁰⁶ for the anion. For atoms separated by three covalent bonds, Coulombic interactions were scaled by a factor of 0.4 while Lennard-Jones interactions were fully included. The partial charges were derived from quantum mechanical calculations performed on an isolated $[\text{C}_n\text{mim}^+][\text{Tf}_2\text{N}^-]$ ($n = 4, 8, 12$) ion pair using a Density Functional Theory (DFT) methodology. Further details on the procedure followed for the calculation of the partial charges can be found in Ref. 45 and ⁵⁹. The calculation of the charges based on the minimum energy conformations of the ionic pair results in reduced total ions' charge, a fact that is attributed to the charge transfer and polarization effects^{2,169}. Additionally, charge distributions obtained by quantum mechanical calculations performed on isolated ions have also been used. These calculations have been performed by Dr. Joerg Rudrigger Hill. The effect of polarizability has been tested by performing simulations using the polarizable Drude oscillator model and by using classical force fields with rescaled charge distributions to lower total ionic charges as a simpler way to implement polarizability and charge transfer effects.

As shown in Chapter 2, the use of charges based on minimum energy conformations of the ionic pair resulted in good agreement with the experimental data for the thermodynamic properties whereas there was a systematic underestimation and overestimation by an order of magnitude of the self-diffusion coefficients and the viscosity, respectively. It has been shown^{159,165-166} that taking into account polarizability and charge transfer effects improves the predictions of the transport properties for ILs. In 3.2.1 and 3.2.2 below, two different strategies to account for polar interactions are presented.

3.2.1 Implementation of the Classical Drude Oscillator Model

The Drude Oscillator Model is based on the incorporation of virtual sites (Drude particles) that carry partial electrical charge and are attached to individual atoms by a harmonic spring²²³⁻²²⁸ (see Figure 3.1).

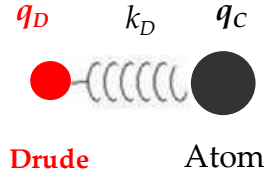


Figure 3.1: The Drude particles are attached to atoms with a harmonic string of force constant k_D .

The movement of a Drude particle serves as a means for changing distribution of the electric charge associated with the corresponding atom. Drude particles are manipulated as atoms during simulation and so, implementation of polarizability effects is straightforward, without major modifications in the functional form of the potential energy. The term that corresponds to the contribution of the Drude particles to the system's potential energy is given by:

$$U_{Drude} = \sum_{A < B}^{N, N_D} \frac{q_D(A)q_C(B)}{|\mathbf{r}_D(A) - \mathbf{r}(B)|} + \sum_{A < B}^{N_D} \frac{q_D(A)q_D(B)}{|\mathbf{r}_D(A) - \mathbf{r}_D(B)|} + \frac{1}{2} \sum_A^{N_D} k_D |\mathbf{r}_D(A) - \mathbf{r}(A)|^2 \quad (3.1)$$

where k_D is the Drude force constant, $q(A)$ is the partial atomic charge of the atom A, $q_D(A) = \sqrt{k_D \alpha(A)}$ is the charge of the Drude particle that is connected to the atom A, $\alpha(A)$ is the polarizability of the atom A, $q_C(A) = q(A) - q_D(A)$ is the atomic charge of the core and $\mathbf{r}(A)$ is the position of the atom A. Recently, the use of the Drude model

has become available in NAMD¹⁹⁷. However, its implementation is in relatively early stage and the necessary input files for the simulation are not provided by the developers. So the implementation of the Drude Oscillator Model in NAMD requires that the user incorporates the Drude particles into the system of interest before starting the simulations.

The [C₈mim⁺][Tf₂N⁻] IL was chosen as a test system and simulations were performed mainly at 298.15 K using NAMD¹⁹⁷ in order to examine the agreement with the experimental values for the ions' self-diffusivities. Atomic polarizabilities were found in the literature²²⁹ and the charge distribution used for the implementation of the Drude Model was obtained by quantum mechanical calculations performed by Dr. Jörg-Rüdiger Hill of Scienomics²⁰³ on the isolated ions in order to have total ionic charges equal to $\pm 1e^-$. The different schemes used for the implementation of the Drude model are shown in Table 3.1 and extracted diffusivities are shown in Figure 3.1 in comparison to results obtained in Section 3.2.2.

One major drawback of this method is the increase of the computational cost due to the lower integration step. As can be seen in Table 3.1, the use of the Drude Model required a decrease of the integration step in order to have a stable simulation. Another important issue is that one needs to calculate IL specific polarizabilities in order to obtain a realistic representation of polarizability effects into the system.

Table 3.1: The different schemes used for the implementation of the Drude model.

Drude Charge	Simulation	Integration Step
-0.5 e	30ns NPT, 10ns NVT	0.5 fs
-1 e	10ns NPT, 20ns NVT	0.5 fs
-2 e	5ns NPT	0.2 fs
Atom-specific Drude charge by setting $k_D=500\text{kcal}/(\text{mol}\cdot\text{\AA})$	10ns NPT	0.5 fs

3.2.2 Use of Reduced Total Ionic Charge

Scaling the ionic total charge to values lower than ± 1 has been widely used in molecular simulation studies of ILs^{51,169,175-176,179} as an alternative to using complicated polarizable force fields and it has been reported to result in better

predictions for transport properties. In this analysis, the charge distributions obtained both by quantum mechanical calculation of the isolated ions (abbreviated “ISO”) and by calculation on the six minimum energy conformations, were uniformly scaled to give lower values of total ionic charge.

Different charge models have been tested: ISO, ISO charge scheme with Drude charge $0.5e^-$, ISO scaled to $0.8e^-$ with Drude charge of $0.5e^-$, ISO charge scheme scaled to $0.8e^-$ and $0.75e^-$, 6RC scaled to $0.8e^-$ and $0.75e^-$. In Figure 3.1 results on self-diffusion coefficients of the ions’ centers of mass are shown as calculated using different charge schemes and are plotted against experimental data²⁰⁷. As can be seen in Figure 3.1, the lowest self-diffusivities were obtained with the ISO charge scheme. On the other hand, the ISO scheme performs equally well with the 6RC when is uniformly scaled to a total charge of $0.75e^-$. The scaling of the partial charges results in significant improvement of the predicted transport properties, whereas the density is very weakly affected and there is no notable impact in the structural properties.

The charge scheme chosen to be used for the remaining of the calculations is the 6RC scaled to $0.75e^-$ since it is directly related to the force field used in Chapter 2. Calculations performed with the force field used in Chapter 2 will be referred to as “6RC” since the charge distribution was derived from *ab initio* calculations on six minimum energy conformations of the ion pair, while results using the new force field will be referred to as “6RC scaled $0.75e^-$ ”.

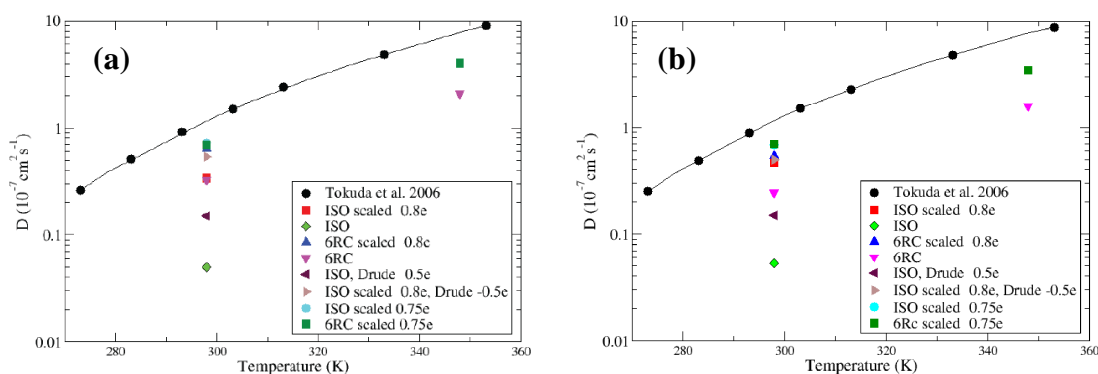


Figure 3.1: Self-diffusion coefficients of (a) the cation and (b) the anion of $[\text{C}_8\text{mim}^+][\text{TF}_2\text{N}^-]$ against experimental values²⁰⁷ using various charge schemes.

3.3 Results on Density, Self-diffusivity and Viscosity

MD predictions for the density of the three ILs are plotted in Figure 3.2 against experimental data^{11-12,207,230} as a function of temperature. Our previous calculations are also shown for comparison (6RC). In all cases, the deviation between the calculated values and the experimental measurements is less than 1%. There is a systematic decrease of the values compared to our previous calculations, primarily driven by the reduction in the intensity of the attractive electrostatic interactions. The values of the density using the scaled charges are also given in Table A8 of Appendix A.

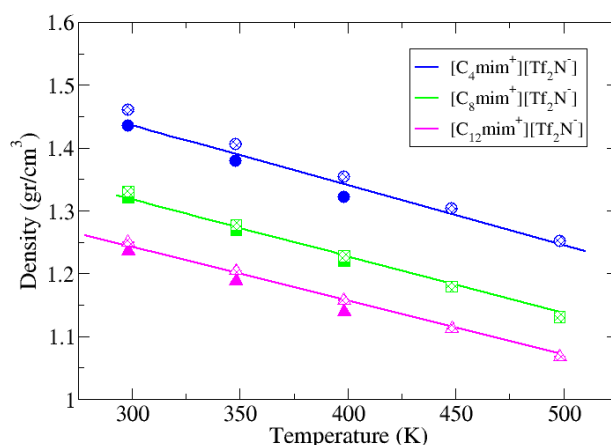


Figure 3.2: MD predictions for the density of $[C_n\text{mim}^+][\text{TF}_2\text{N}^-]$, $n = 4, 8, 12$. Full points correspond to the optimized force field (6RC scaled to $0.75e^-$), open points to previous calculations using the 6RC charge distribution and the lines are interpolation/extrapolation of experimental data for $[C_4\text{mim}^+][\text{TF}_2\text{N}^-]$ ¹¹⁻¹², $[C_8\text{mim}^+][\text{TF}_2\text{N}^-]$ ²⁰⁷ and $[C_{12}\text{mim}^+][\text{TF}_2\text{N}^-]$ ²³⁰.

The diffusion coefficients were calculated using the Einstein relation (Eq. 2.9) in the Fickian regime, which is identified by a slope equal to unity in the $\log(\text{MSD})$ versus $\log(t)$ plot. The self-diffusion coefficients of $[C_4\text{mim}^+][\text{TF}_2\text{N}^-]$, $[C_8\text{mim}^+][\text{TF}_2\text{N}^-]$ and $[C_{12}\text{mim}^+][\text{TF}_2\text{N}^-]$ calculated using the optimized force field (6RCscaled0.75e) are plotted in Figure 3.3a, 3.3b and 3.3c respectively as a function of temperature, together with experimental data^{207,218}. For comparison, our previous results on self-diffusivity are also plotted (6RC). The calculated self-diffusivities using the scaled charges are also given in Table A9 of Appendix A.

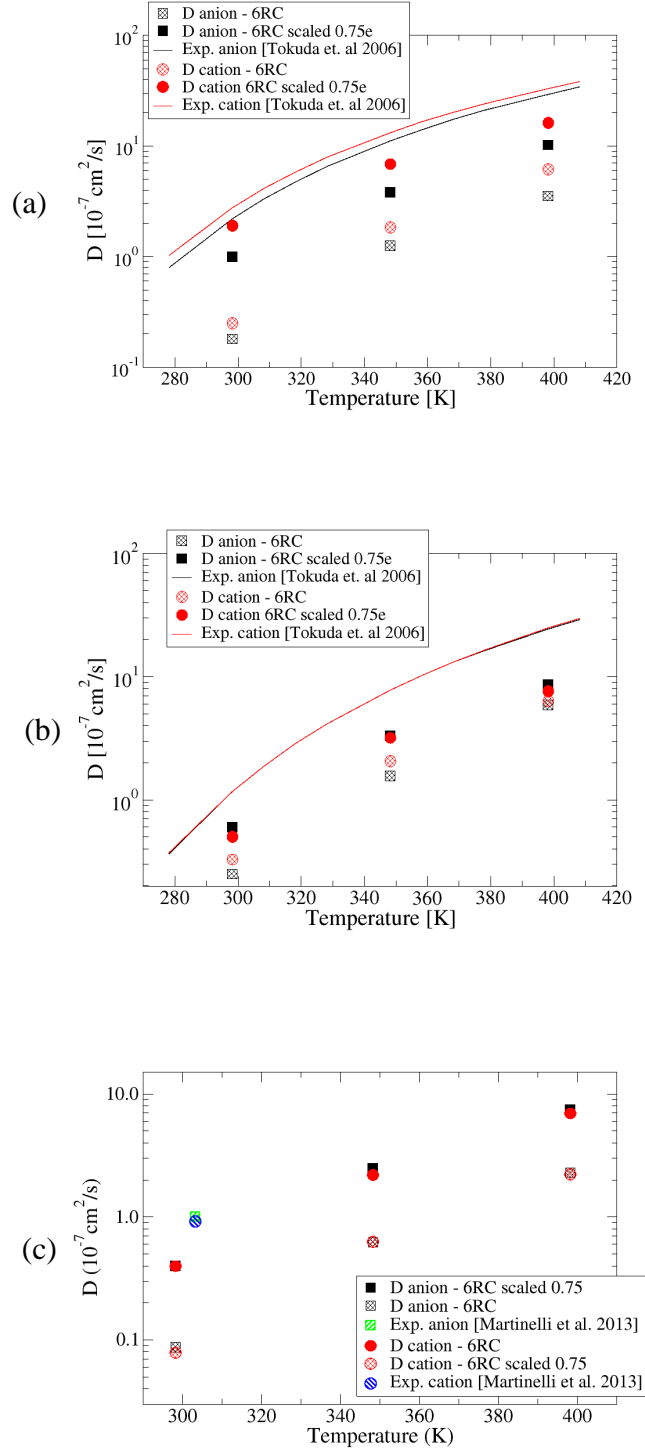


Figure 3.3: Self-diffusion coefficients of the center of mass of anion (squares) and cation (circles) using the 6RC scaled $\pm 0.75e$ charge scheme (full points) for (a) $[\text{C}_4\text{mim}^+][\text{Tf}_2\text{N}^-]$, (b) $[\text{C}_8\text{mim}^+][\text{Tf}_2\text{N}^-]$ and (c) $[\text{C}_{12}\text{mim}^+][\text{Tf}_2\text{N}^-]$ compared to previous data, 6RC (open points), against experimental data for $[\text{C}_4\text{mim}^+][\text{Tf}_2\text{N}^-]$, $[\text{C}_8\text{mim}^+][\text{Tf}_2\text{N}^-]^{207}$ (solid lines) and $[\text{C}_{12}\text{mim}^+][\text{Tf}_2\text{N}^-]^{218}$ (green points).

There is a clear improvement in the accuracy of the calculations with the new force field while simulation captures quite well the temperature dependence of the self-diffusivities as well as the fact that the cation's self-diffusion coefficient is higher than the anion's for $[\text{C}_4\text{mim}^+][\text{Tf}_2\text{N}^-]$ as reported in past simulation studies of imidazolium-based ILs^{2,51,53,152,219-220}, too. As the alkyl tail becomes longer, the cation's mobility is reduced and the ions attain comparable self-diffusivities, as can be seen in Figures 3.3b and 3.3c for the case of $[\text{C}_8\text{mim}^+][\text{Tf}_2\text{N}^-]$ and $[\text{C}_{12}\text{mim}^+][\text{Tf}_2\text{N}^-]$.

Calculations of the shear viscosity were performed using the Green-Kubo relationship (Eq. 2.11). Shear viscosity is a collective property of the system and, therefore, its calculation is prone to errors due to the sensitivity of the stress correlation function to the intra-molecular vibrational modes. At the same time, experimental measurements of viscosity are also very sensitive to impurities of the testing material; consequently, even experimental results obtained using the same method deviate from each other³⁷. The stress correlation function was calculated at the last section of each productive NVT run during which the information of the pressure was stored each 8 fs and the viscosity was estimated by the integral plateau value after reassuring that the pressure autocorrelation function was fluctuating around zero. In Figures 3.4a, 3.4b and 3.4c, the values for the viscosity of $[\text{C}_4\text{mim}^+][\text{Tf}_2\text{N}^-]$, $[\text{C}_8\text{mim}^+][\text{Tf}_2\text{N}^-]$ and $[\text{C}_{12}\text{mim}^+][\text{Tf}_2\text{N}^-]$, respectively, are plotted against our previous calculations and are compared to experimental data^{14,207,221-222}. The calculated viscosities using the scaled charges are also given in Table A10 of Appendix A. The simulations using the optimized force field result in a much better agreement between the calculated viscosity values and the experimental data, and the temperature dependence is captured very accurately.

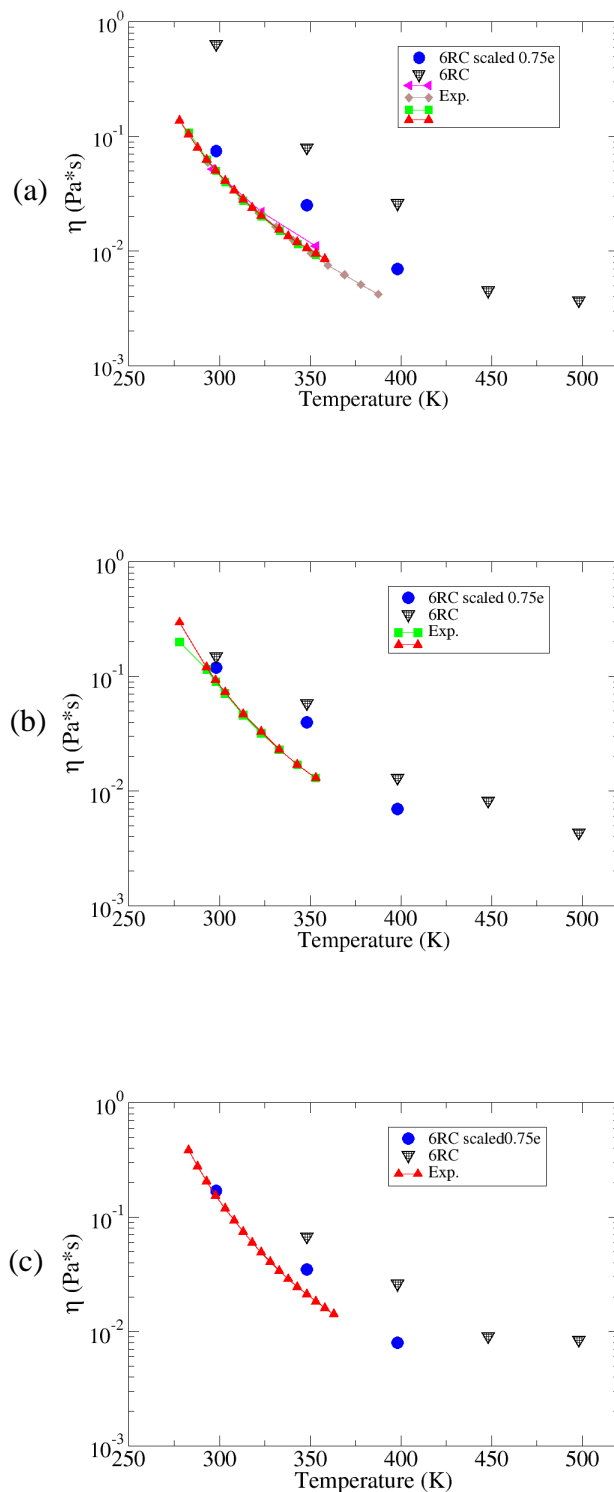


Figure 3.4: Viscosity calculations using the optimized force field of the present work, 6RC scaled 0.75e⁻, (full circles) compared to data using the 6RC force field (open triangles) for (a) $[\text{C}_4\text{mim}^+][\text{Tf}_2\text{N}^-]$ against the experimental data^{14,207,221-222}, (b) $[\text{C}_8\text{mim}^+][\text{Tf}_2\text{N}^-]$ against the experimental data^{207,221} and (c) $[\text{C}_{12}\text{mim}^+][\text{Tf}_2\text{N}^-]$ against the experimental data²²¹.

3.4 Dynamic Behaviour of Ionic Liquids

Computational studies found in the literature concerning the heterogeneous nature of the dynamics of ILs have focused on the quantification of the non-Gaussian character of the dynamics by calculating the non-Gaussian parameter and by analyzing the deviations of the self-part of the Van Hove correlation function²³¹ from the expected Gaussian form. Del Pópolo and Voth⁵⁴ studied the dynamics of $[\text{C}_2\text{mim}^+][\text{NO}_3^-]$ and identified spatial correlations between ions of similar mobility. Hu and Margulis⁵⁵⁻⁵⁶ conducted molecular dynamics (MD) simulations on $[\text{C}_4\text{mim}^+][\text{PF}_6^-]$ and investigated the coupling between translational and rotational diffusion and the connection of dynamic heterogeneity phenomena to the “red-edge effect”. Köddermann *et al.*⁷⁵ examined the connection between dynamic heterogeneity phenomena and the non-validity of the Stokes-Einstein and the Stokes-Einstein-Debye relations by simulating $[\text{C}_2\text{mim}^+][\text{TF}_2\text{N}^-]$ and its mixtures with chloroform. Liu and Maginn⁵¹ analyzed the non-Gaussian behaviour of $[\text{C}_4\text{mim}^+][\text{TF}_2\text{N}^-]$ at various temperatures and studied the anisotropy in the ions’ translational motion, while Urahata and Ribeiro⁵² focused on the investigation of the link between dynamic heterogeneity and the conformations of the alkyl chains in $[\text{C}_4\text{mim}^+][\text{Cl}^-]$. Moreover, mutual diffusion of anions and cations and the multi-fractal nature of the heterogeneous dynamics have been thoroughly studied by Habasaki and Ngai^{58,76}.

3.4.1 Analysis of the Ions’ Translational Motion

In an effort to investigate the origin of the fact that in many cases cations are found to have an enhanced diffusivity compared to anions, Urahata and Ribeiro⁵³ studied the anisotropy in the cation’s diffusion for the case of imidazolium-bases ILs with small-sized anions. They analyzed the cations’ translational motion along specific axes, namely along the vector that is normal to the imidazolium ring, along the vector NN that connects the two nitrogens of the imidazolium ring and along the vector NNp that is perpendicular to the other two vectors (see Figure 3.5a). They identified an enhanced movement of the cation along the NNp vector that lies on the plane of the imidazolium ring and is almost perpendicular to the alkyl chain. Liu and Maginn⁵¹ performed a similar analysis for the case of $[\text{C}_4\text{mim}^+][\text{TF}_2\text{N}^-]$ and also found anisotropy in the diffusion, detecting in their case the direction along the NN vector as being the most favourable one.

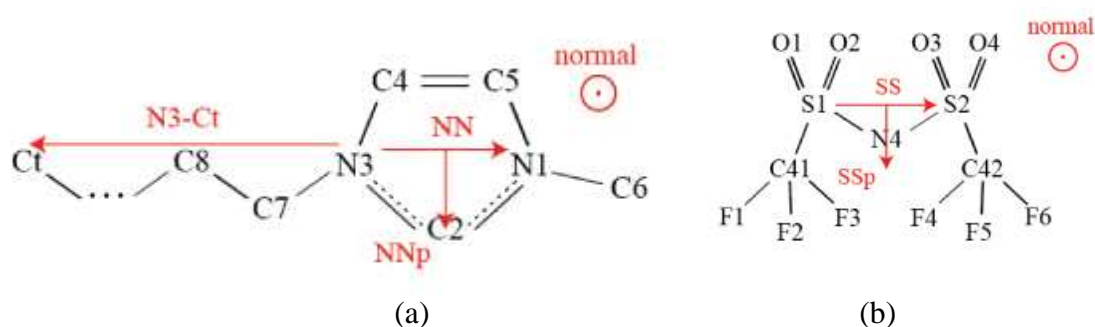


Figure 3.5: The directions along which the translational motion was analyzed for (a) the cation and (b) the anion.

We further investigated this phenomenon and examined the effect of the alkyl tail length by analyzing the cations' translational motion along the three axes mentioned above and, additionally, along the N3-Ct vector that connects the terminal carbon atom of the alkyl tail (Ct) and the N3 nitrogen of the imidazolium ring (see Figure 3.5a). At the same time, the anions' translational motion was analysed along the axes: (i) SS that connects the two sulphurs, (ii) SSp that is perpendicular to SS and lies on the plane defined by the two sulphur atoms and the nitrogen of the anion, and, (iii) the vector normal to the plane that is defined by the SS and the SSp vectors (see Figure 3.5b). The mean square displacement (MSD) of the ions' center of mass in each specific axis is compared to the 1/3 of the total MSD of the ions' center of mass.

In Figure 3.6, the MSD along each axis is shown for the cation and the anion of $[\text{C}_4\text{mim}^+][\text{Tf}_2\text{N}^-]$, $[\text{C}_8\text{mim}^+][\text{Tf}_2\text{N}^-]$ and $[\text{C}_{12}\text{mim}^+][\text{Tf}_2\text{N}^-]$ at 298.15 K. In accordance with Liu and Maginn⁵¹, all the cations exhibit an enhanced movement along the NN vector that lies in the plane of the imidazolium ring. In fact, for the case of $[\text{C}_4\text{mim}^+][\text{Tf}_2\text{N}^-]$ where the cation's alkyl tail is rather short, the MSD along the N3-Ct vector is the same as the MSD along the NN vector. However, as the alkyl tail becomes longer, the MSD along the alkyl tail (N3-Ct) is much larger compared to the MSD along the NN vector. For the case of $[\text{C}_8\text{mim}^+][\text{Tf}_2\text{N}^-]$ at 298.15 K (Figure 3.5c) the MSD along N3-Ct at 8 ns is almost 50% higher than the 1/3 of the total MSD, whereas for the case of $[\text{C}_{12}\text{mim}^+][\text{Tf}_2\text{N}^-]$ that has the longest alkyl tail, this deviation reaches almost 100% (Figure 3.6e). This behaviour is preserved at very long times and is present even at time scales that correspond to the Fickian regime of the total MSD at 298.15 K.

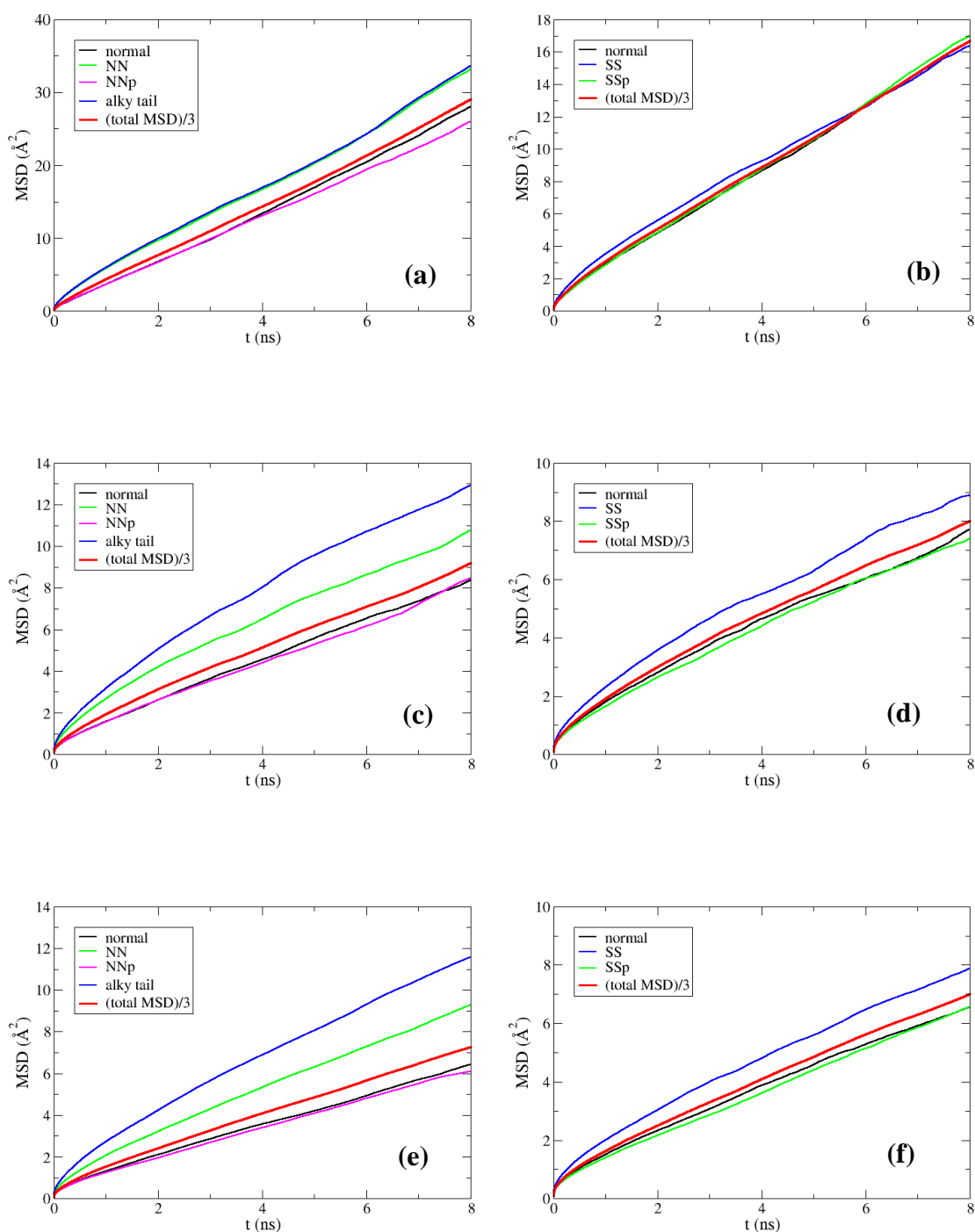


Figure 3.6: Mean square displacement (MSD) at 298.15 K calculated along the direction of the vectors NN, NNp, the normal to them vector and the alkyl tail for the cation and along the vectors SS, SSp and the normal to them vector for the anion. (a) cation and (b) anion of $[\text{C}_4\text{mim}^+][\text{Tf}_2\text{N}^-]$, (c) cation and (d) anion of $[\text{C}_8\text{mim}^+][\text{Tf}_2\text{N}^-]$ and (e) cation and (f) anion of $[\text{C}_{12}\text{mim}^+][\text{Tf}_2\text{N}^-]$.

The analysis of the anion's diffusion also reveals a favorable motion along the SS vector, which is more pronounced for the two ILs with the longest alkyl tails (see Figure 3.5b, d, f). As the temperature increases, the difference in the MSDs is only present at very short timescales, for example, for $[\text{C}_4\text{mim}^+][\text{Tf}_2\text{N}^-]$ at 398.15 K, this preferential translational motion is observed below 1 ns for the cation and below 0.5 ns for the anion (see Figure 3.7).

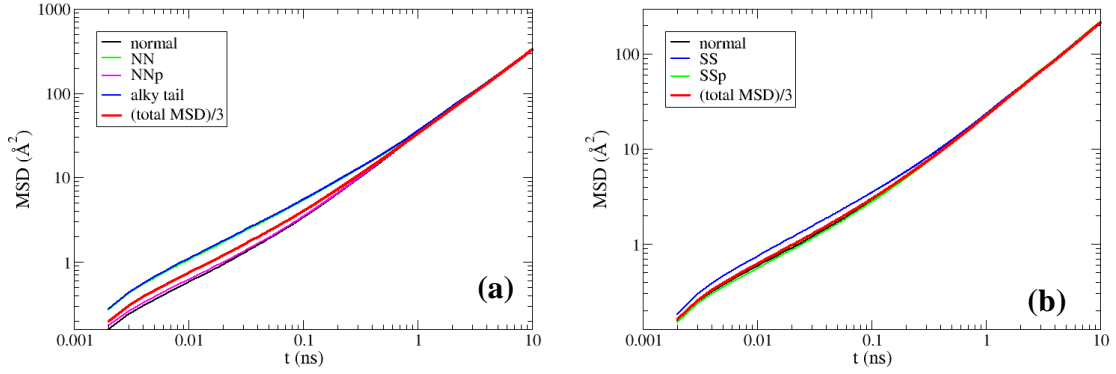


Figure 3.7: Mean square displacement (MSD) at 398.15 K analyzed in specific axes on the ions for (a) cation and (b) anion of $[\text{C}_4\text{mim}^+][\text{Tf}_2\text{N}^-]$.

3.4.2 Dynamic Heterogeneity

The ions' translational motion is further analyzed in order to investigate the presence of heterogeneity in the dynamics by detecting deviations from the expected Gaussian behaviour. The global non-Gaussian behaviour of a system can be quantified by analyzing the time dependence of the non-Gaussian parameter $\alpha_2(t)$ defined as²³²:

$$\alpha_2(t) = \frac{3 \langle |\mathbf{r}_i(t) - \mathbf{r}_i(t_0)|^4 \rangle}{5 \langle |\mathbf{r}_i(t) - \mathbf{r}_i(t_0)|^2 \rangle^2} - 1 \quad (3.2)$$

where $|\mathbf{r}_i(t) - \mathbf{r}_i(t_0)|$ is the displacement of an ion's center of mass at time t with respect to its position at time t_0 . In the case of a Gaussian distribution of $|\mathbf{r}_i(t) - \mathbf{r}_i(t_0)|$, $\alpha_2(t)$ is equal to zero, while any deviation from zero is indicative of dynamic heterogeneities in the system revealing simultaneously the time scale at which the

non-Gaussian behaviour is present. The time at which $\alpha_2(t)$ reaches a maximum value indicates the time interval of the most intense dynamic heterogeneity.

The self-part $G_s(\mathbf{r}, t)$ of the van Hove correlation function²³¹ is given by:

$$G_s(\mathbf{r}, t) = \frac{1}{N} \left\langle \sum_{i=1}^N \delta[\mathbf{r} + \mathbf{r}_i(0) - \mathbf{r}_i(t)] \right\rangle = \frac{1}{N} \left\langle \sum_{i=1}^N \delta[\Delta\mathbf{r}(t)] \right\rangle \quad (3.3)$$

and corresponds to the probability that a particle (or the center of mass of a molecule) is at position $\mathbf{r}_i(t)$ at time t given that it was located at $\mathbf{r}_i(0)$ at time 0. Note that for all times t :

$$\int_0^\infty 4\pi r^2 G_s(\mathbf{r}, t) d\mathbf{r} = 1 \quad (3.4)$$

The probability density that a particle moves by distance r is given by the solid angle integral²³³:

$$g_s(r, t) = \int_{\theta=0}^\pi \int_{\varphi=0}^{2\pi} G_s(\mathbf{r}, t) r^2 \sin \theta d\varphi d\theta \quad (3.5)$$

In case of isotropy, $G_s(\mathbf{r}, t) = G_s(r, t)$ and so, $g_s(r, t) = 4\pi r^2 G_s(r, t)$.

When heterogeneous dynamics is present, the self-part $G_s(\mathbf{r}, t)$ of the van Hove correlation function deviates from the expected Gaussian distribution that is given by the following expression:

$$G_g(\mathbf{r}, t) = \left(\frac{3}{2\pi \langle |\Delta\mathbf{r}(t)|^2 \rangle} \right)^{3/2} \exp \left\{ \frac{-3r^2}{2 \langle |\Delta\mathbf{r}(t)|^2 \rangle} \right\} \quad (3.6)$$

where $\langle |\Delta\mathbf{r}(t)|^2 \rangle$ is the mean square displacement (MSD) of the particles.

In Figure 3.8, the non-Gaussian parameter $\alpha_2(t)$ is plotted against time for the cation and the anion of the three ILs at 298.15, 348.15 and 398.15 K.

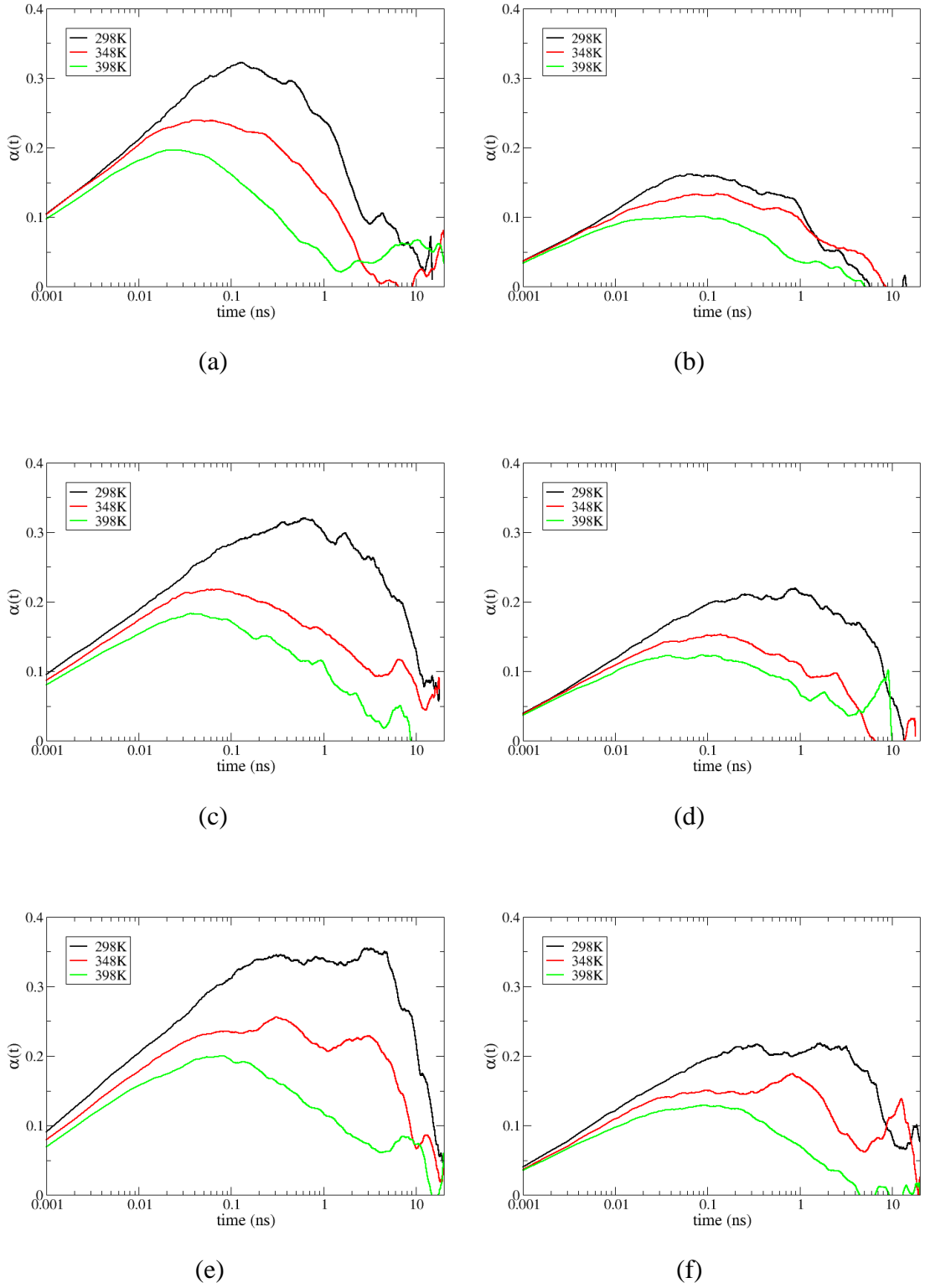


Figure 3.8: Non-Gaussian parameter $\alpha_2(t)$ for (a) cation and (b) anion of $[\text{C}_4\text{mim}^+][\text{Tf}_2\text{N}^-]$, (c) cation and (d) anion of $[\text{C}_8\text{mim}^+][\text{Tf}_2\text{N}^-]$ and (e) cation and (f) anion of $[\text{C}_{12}\text{mim}^+][\text{Tf}_2\text{N}^-]$ calculated at 298.15 K.

For both ions, $\alpha_2(t)$ maximizes at intermediate times and as the temperature decreases, the maximum of $\alpha_2(t)$ tends to appear at longer times reaching a higher value. Cations systematically exhibit a higher degree of heterogeneity than anions, which is reflected to a higher peak of $\alpha_2(t)$. These findings are in agreement with previous analysis of dynamic heterogeneities of ILs found in the literature^{51,54}. It is evident, especially at low temperatures, that as the alkyl tail becomes longer the heterogeneity in the dynamics is present for much longer time intervals for both ions since the non-Gaussian parameter starts to decay at much longer times. This indicates the existence of a cage regime of longer duration, a fact that can be directly related to the MSD behaviour and the time scales involved for reaching in each case the Einstein regime of diffusion. For example, for the case of the cation of $[\text{C}_{12}\text{mim}^+][\text{TF}_2\text{N}^-]$ at 298.15 K (Figure 3.8e), $\alpha_2(t)$ starts to decay at about 8 ns, that is, the time at which the cation's diffusion reaches the Fickian regime (see Figure 3.9).

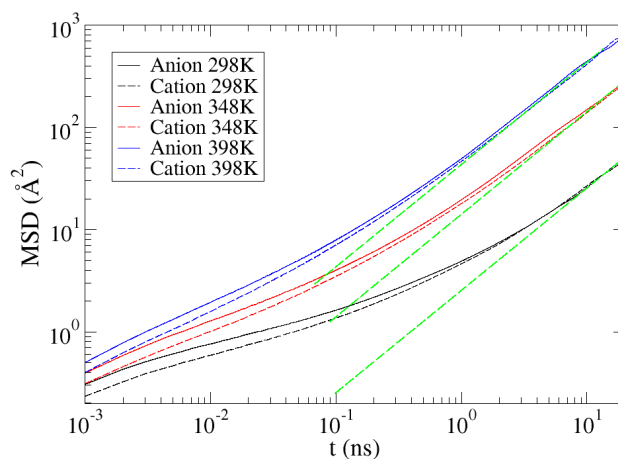


Figure 3.9: Mean square displacement (MSD) of the anion (full lines) and the cation (dotted lines) of $[\text{C}_{12}\text{mim}^+][\text{TF}_2\text{N}^-]$ calculated at 298.15 K (black), 348.15 K (red) and 398.15 K (blue). The slope of the dotted green lines is equal to unity and indicates the Fickian regime.

The self-part of the van Hove function $4\pi r^2 G_s(r, t)$ calculated at $t = 10, 300, 1000$ and 3000 ps is plotted in Figure 3.10 as a function of distance r and in comparison to the corresponding expected Gaussian distribution for (a) cation and (b) anion of $[\text{C}_4\text{mim}^+][\text{TF}_2\text{N}^-]$, (c) cation and (d) anion of $[\text{C}_8\text{mim}^+][\text{TF}_2\text{N}^-]$ and (e) cation and (f) anion of $[\text{C}_{12}\text{mim}^+][\text{TF}_2\text{N}^-]$ at 298.15 K.

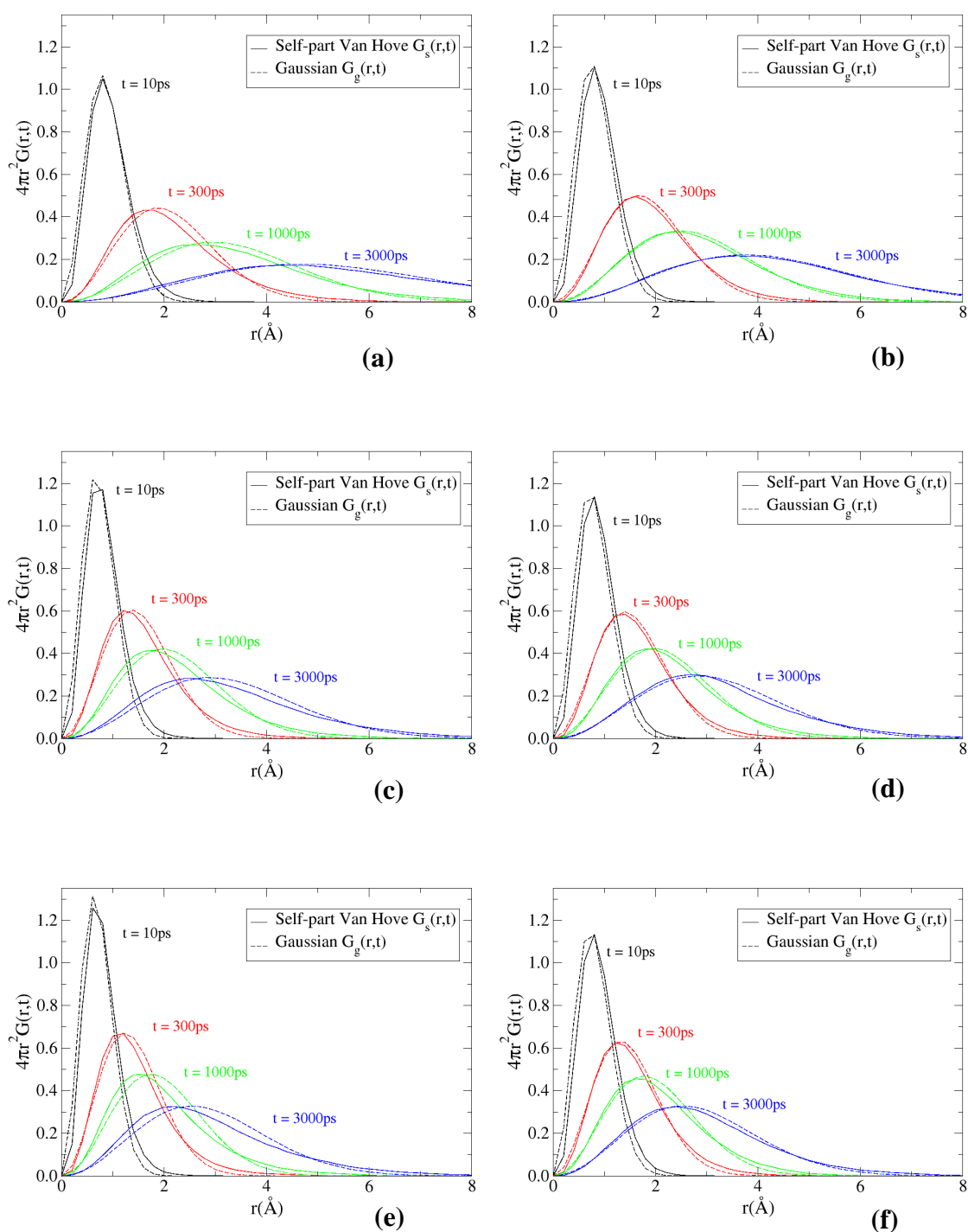


Figure 3.10: Self-part of the Van Hove function $G_s(r,t)$ at 298.15 K compared to the expected Gaussian distribution for (a) cation and (b) anion of $[C_4mim^+][Tf_2N^-]$, (c) cation and (d) anion of $[C_8mim^+][Tf_2N^-]$ and (e) cation and (f) anion of $[C_{12}mim^+][Tf_2N^-]$.

These plots clearly show that there are deviations from the Gaussian distribution and that heterogeneity phenomena are present at time intervals from a few

ps up to several ns depending on the ionic liquid. This is more pronounced for the two ILs with the longest alkyl tails, for which the caging regime involves longer times.

In agreement with the $\alpha_2(t)$ results, the $G_s(r,t)$ of the cations exhibit greater deviations from the Gaussian distribution, a fact that is attributed to the non-uniform way that anions surround the cations, while the anions experience a more uniform neighborhood⁵¹. At all cases, the deviations from the Gaussian distribution are reduced as the temperature increases (see for example, Figure 3.11).

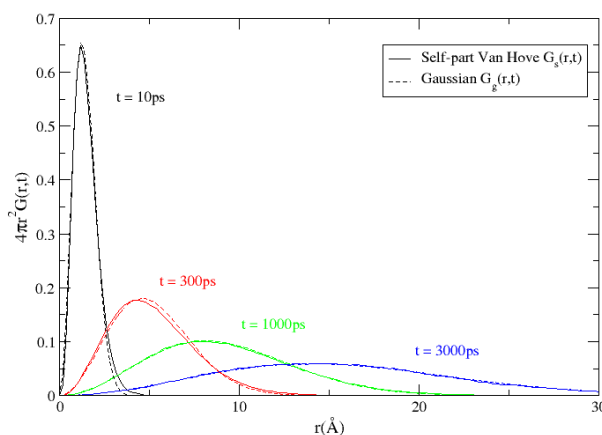


Figure 3.11: Self-part of the Van Hove function $G_s(r,t)$ at 398.15 K compared to the expected Gaussian distribution for the cation of $[\text{C}_4\text{mim}^+][\text{Tf}_2\text{N}^-]$.

Following the approach of Kob *et al.*⁶³ on super-cooled liquids, ions can be classified according to their mobility (the distance each ion has travelled at time t). In many cases $G_s(r,t)$ and $G_g(r,t)$ intersect both at short, say r_1 , and at long distances, say r_2 , indicating the existence of ions with low and high mobility, i.e. $G_s(r,t) > G_g(r,t)$ for $r < r_1$ and $G_s(r,t) > G_g(r,t)$ for $r > r_2$, respectively (see for example Figure 3.10e). The spatial correlation between the groups of ions with different mobility is examined by calculating all the relevant pair distribution functions $g(r)$. The formation of clusters with ions of high mobility has been previously reported in other imidazolium-based ILs as $[\text{C}_2\text{mim}^+][\text{NO}_3^-]$ ⁵⁴, $[\text{C}_4\text{mim}^+][\text{Cl}^-]$ ⁵² and $[\text{C}_4\text{mim}^+][\text{PF}_6^-]$ ⁵⁶.

Figure 3.12 shows the radial distribution functions between the centers of mass of dynamically distinguishable cations and anions calculated at 298.15 K and $t = 500$ ps for (a) $[\text{C}_4\text{mim}^+][\text{Tf}_2\text{N}^-]$, (b) $[\text{C}_8\text{mim}^+][\text{Tf}_2\text{N}^-]$ and (c) $[\text{C}_{12}\text{mim}^+][\text{Tf}_2\text{N}^-]$, in

comparison with the overall $g(r)$ between anion-cation centres of mass in the bulk. The term “bulk” refers to the total radial distribution function calculated without any discrimination on the ions’ mobility. The subsets of ions considered in the calculations of $g(r)$ consist of the 8-10 % most immobile (if present) and mobile ions.

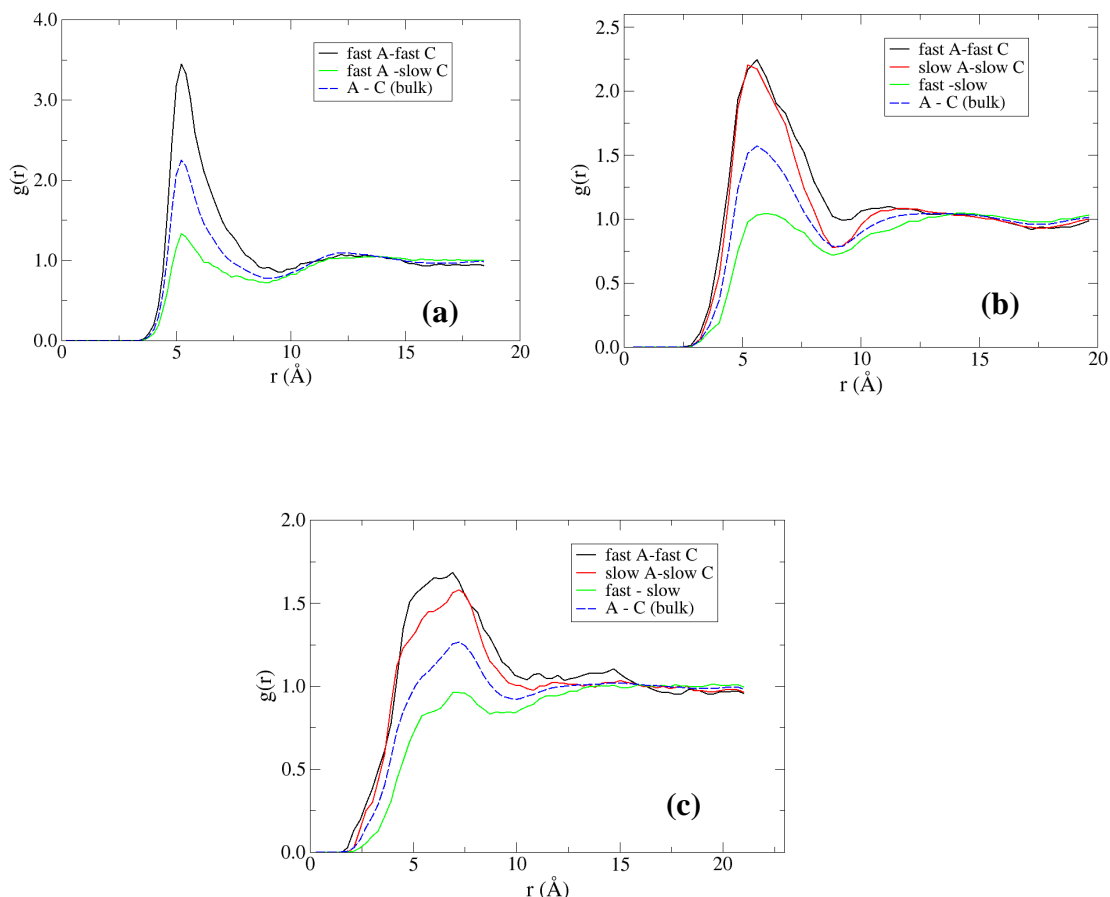


Figure 3.12: Radial distribution functions between the centers of mass of dynamically distinguishable cations and anions calculated at 298.15 K for $t = 500$ ps. (a) $[\text{C}_4\text{mim}^+][\text{Tf}_2\text{N}^-]$, (b) $[\text{C}_8\text{mim}^+][\text{Tf}_2\text{N}^-]$ and (c) $[\text{C}_{12}\text{mim}^+][\text{Tf}_2\text{N}^-]$.

These plots clearly depict that there is a strong spatial correlation between anions and cations of the same mobility (fast-fast or slow-slow) as indicated by the higher peak of the $g(r)$ in comparison with the $g(r)$ in the bulk, while ions of different mobility (fast-slow) are less correlated in space. Clusters consisting of either mobile or immobile ions are formed in the bulk, while it is less likely to find a mobile ion in the neighbourhood of an immobile counterion. Subsets of immobile and mobile cations are present in all systems at intermediate times and even at higher

temperatures, while no immobile anions are detected in case of $[\text{C}_4\text{mim}^+][\text{Tf}_2\text{N}^-]$ at all time scales and temperatures. The pair correlation function between fast anions – fast cations exhibits a much higher peak than the one that corresponds to the $g(r)$ in the bulk $[\text{C}_4\text{mim}^+][\text{Tf}_2\text{N}^-]$ (Figure 3.12a), and as the alkyl tail becomes longer the peak becomes wider but in all cases it is observed at the same distance with the corresponding one of the bulk. Similar behaviour is observed for slow anion - slow cation pair correlation functions for $[\text{C}_8\text{mim}^+][\text{Tf}_2\text{N}^-]$ (Figure 3.12b) and $[\text{C}_{12}\text{mim}^+][\text{Tf}_2\text{N}^-]$ (Figure 3.12c), in which slow anions are also present. Furthermore, the anion-anion pair distribution function shows similar characteristics: fast-fast and slow-slow anion correlation is more intense than the one in the bulk, while it is less likely to find anions of different mobility close to each other, as shown in Figure 3.13. These observations are much weaker when calculating the corresponding cation-cation correlation functions as depicted in Figure 3.14.

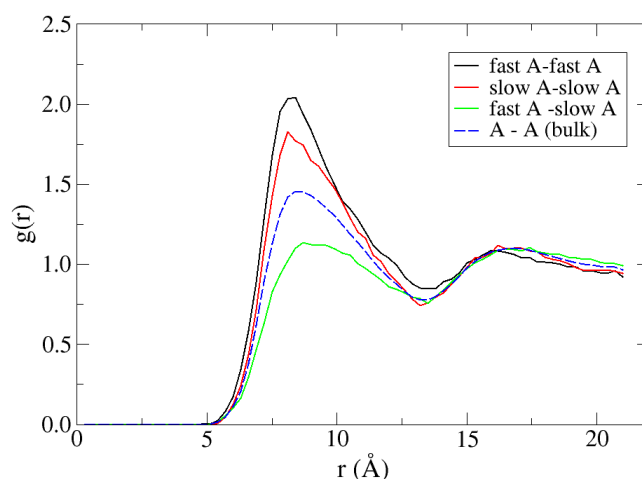


Figure 3.13: Radial distribution functions at 298.15 K for $t = 500$ ps between the centers of mass of fast and slow anions of $[\text{C}_{12}\text{mim}^+][\text{Tf}_2\text{N}^-]$.

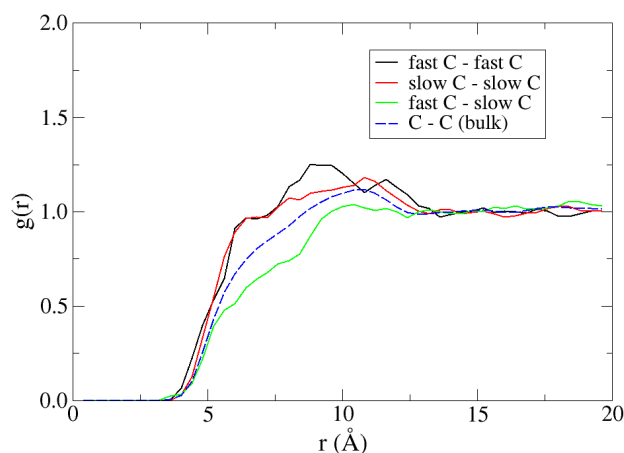


Figure 3.14: Radial distribution functions at 298.15 K for $t = 500$ ps between the centers of mass of fast and slow cations of $[\text{C}_8\text{mim}^+][\text{Tf}_2\text{N}^-]$.

The time evolution of the spatial organization of the mobile cations and anions is shown in Figure 3.15a and 3.15b for $[\text{C}_4\text{mim}^+][\text{Tf}_2\text{N}^-]$ and $[\text{C}_8\text{mim}^+][\text{Tf}_2\text{N}^-]$, respectively, at 298.15 K and $t = 10$ -1000 ps. The tendency of fast ions to approach their fast counterions is already present at 10 ps and the peak has reached its highest value in a time interval of 100 ps. At the same time, the probability of fast anions to be in the neighbourhood of other fast anions maximizes at approximately 300 ps for the case of $[\text{C}_4\text{mim}^+][\text{Tf}_2\text{N}^-]$, as shown in Figure 3.16.

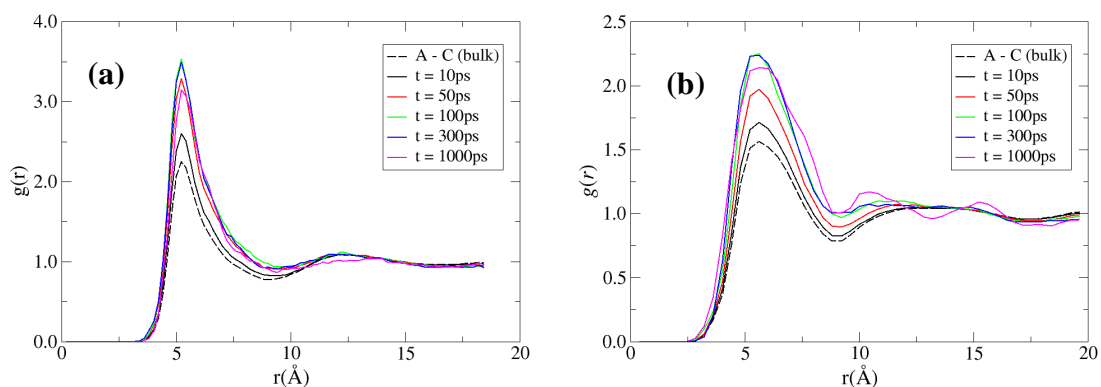


Figure 3.15: Radial distribution functions between the centers of mass of fast cations and fast anions calculated at 298.15 K for $t = 10, 50, 100, 300$ and 1000 ps. (a) $[\text{C}_4\text{mim}^+][\text{Tf}_2\text{N}^-]$ and (b) $[\text{C}_8\text{mim}^+][\text{Tf}_2\text{N}^-]$.

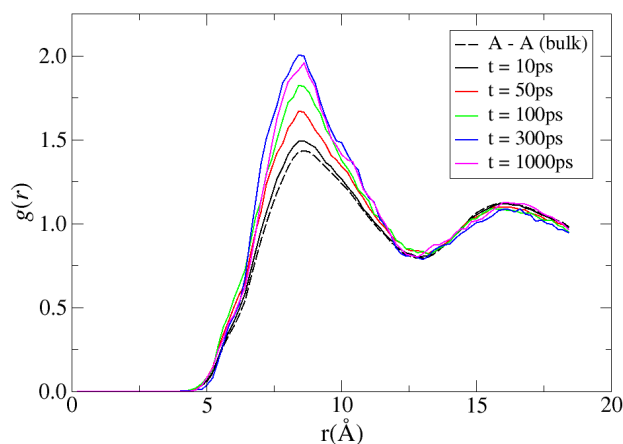


Figure 3.16: Radial distribution functions between the centers of mass of fast anions of $[\text{C}_4\text{mim}^+][\text{Tf}_2\text{N}^-]$ calculated at 298.15 K for $t = 10, 50, 100, 300$ and 1000 ps.

3.5 Conclusions

The force field for $[\text{C}_4\text{mim}^+][\text{Tf}_2\text{N}^-]$, $[\text{C}_8\text{mim}^+][\text{Tf}_2\text{N}^-]$ and $[\text{C}_{12}\text{mim}^+][\text{Tf}_2\text{N}^-]$ was further optimized in order to attain good agreement with the experimental data on transport properties, by uniformly scaling the charge distribution to yield a $\pm 0.75e^-$ total ionic charge. Long MD simulations of several tens of nanoseconds were performed in order to calculate the transport properties of the three ILs mentioned above and analyze their complex dynamic behaviour focusing on the investigation of microscopic heterogeneity phenomena. The results of the optimized force field on density, ion self-diffusion coefficients and viscosity exhibit a significant improvement in the agreement with the experimental data. Detailed analysis of the ions' translational motion reveals anisotropy in the ions' diffusion: there is a preferential movement along the direction of the alkyl tail for the cation and along the direction of the vector that connects the two sulfurs for the anion. The heterogeneous nature of the dynamics is quantified by the non-Gaussian parameter and is further analyzed by comparing the self-part of the Van Hove function to the expected Gaussian distribution. For the longest alkyl tails, the heterogeneity in the dynamics becomes more pronounced and is preserved for several nanoseconds at low temperatures. Subsets of “fast” and “slow” ions are defined by the deviation between the van Hove function and the Gaussian distribution. Dynamically distinguishable ions are found to be strongly correlated in space forming clusters of ions of the same mobility.

Chapter 4

Imidazolium-Based [TCM⁻] Ionic Liquids: Optimization of an All-atom Force Field and Prediction of Thermodynamic, Structure and Transport Properties

Imidazolium-based tricyanomethanide ([TCM⁻]) ILs are reported to be excellent candidates for use in a number of applications since the strong charge delocalization leads to a weak ion pairing and, hence, to low viscosities and melting temperatures^{95,97}. Computational studies of this IL family are limited to one study of 1-ethyl-3-methylimidazolium [TCM⁻] performed by Borodin¹⁶⁶ using an efficient but very complex and computationally expensive many-body polarizable force field. Only Martin *et al.*²³⁴ performed simulations of a [TCM⁻] IL that incorporated a phosphonium-based cation, namely 1-ethyl-1-methylphospholinium, using a classical all-atom force field. On the other hand, over the last decade imidazolium-based cations have been largely studied computationally and therefore, a variety of well-validated force fields can be found in the literature^{163-164,167,205,219}.

The present chapter focuses on the optimization of a classical force field for the molecular simulation of imidazolium-based [TCM⁻] ILs. The IL [C₄mim⁺][TCM⁻] was used as test system for the optimization procedure which mainly concerned the determination of the [TCM⁻] Lennard-Jones (LJ) parameters and the appropriate charge distribution and scaling factor for the total ionic charge. The proposed optimized force field is validated against experimental data by performing MD simulations of the [C_{*n*}mim⁺][TCM⁻] ILs, with *n* = 2, 4, 8 being the number of carbon atoms in the alkyl tail, at various temperatures and at atmospheric pressure. Results on density and transport properties, namely self-diffusivities and viscosities, are in very good agreement with experimental data revealing the ability of the new force field to reliably reproduce the behaviour of imidazolium-based [TCM⁻] ILs in a wide temperature range. Structural properties were calculated and the complex dynamical behaviour was thoroughly investigated.

4.1 Simulation Details

Results presented in this chapter were obtained by long classical MD simulations of 100 $[\text{C}_n\text{mim}^+][\text{TCM}^-]$, $n = 2, 4, 8$, ion pairs performed with the software NAMD¹⁹⁷ using a classical all-atom force field of a functional form given in Eq. 2.1. The initial structures were built using the Rotational Isomeric State (RIS) model²⁰⁰ as modified by Theodorou and Suter^{201,202} available in MAPS²⁰³. The ions were placed in the simulation box at the experimental density, if available, or at the value calculated by extrapolating the available experimental data. A conjugate gradient energy minimization procedure of 10^5 steps was applied to eliminate the atomic overlaps. Afterwards, a 20-50 ns simulation in the isobaric-isothermal ensemble (NPT) was performed in order to calculate the density and relax the system. Finally, simulations in the canonical ensemble (NVT) of the order of 20-50 ns were performed at the mean density as obtained from the NPT simulations, in order to calculate the transport properties. Snapshots were stored every 1 ps during each simulation and the Lorentz-Berthelot mixing rules were used to calculate the force field parameters between unlike atoms.

Control of the temperature was performed using a Langevin piston with a 5 ps^{-1} damping factor while the Nosé-Hoover barostat was used for the pressure control with oscillation period equal to 200 fs and a damping factor of 100 fs. Electrostatic interactions were handled by means of particle-mesh Ewald method, while the electrostatic interactions between atoms connected with three bonds were scaled by a factor of 0.5. The reversible reference system propagator algorithm (rRESPA^{76,204}) was used as a multiple time step algorithm with a 1 fs reference time step in order to speed up the MD simulations. Short-range non-bonded van der Waals interactions were calculated every 2 fs and the full electrostatic interactions were computed every 4 fs. A cutoff distance of 12 \AA was used to truncate the van der Waals interactions using a switching function beyond 10.5 \AA . A long-range correction was applied to the system's energy and virial to account for the neglected van der Waals forces due to switching and cutoff of the Lennard-Jones potential.

System size effects were investigated by simulating systems with 100 and 300 ion pairs of $[\text{C}_4\text{mim}^+][\text{TCM}^-]$ at 298.15 K and 363.15 K at various ensembles in order to calculate the density and the self-diffusion coefficients. At both temperatures, the

calculations of density and self-diffusion coefficient were statistically the same for the two different system sizes.

4.2 Force Field Optimization

The $[\text{C}_4\text{mim}^+][\text{TCM}^-]$ IL was chosen as a benchmark system and all the simulations at this stage were performed at 298.15 K and at atmospheric pressure. The cations' bonded and LJ parameters were obtained from Cadena and Maginn¹⁶⁷, Cadena *et al.*²⁰⁵ and Liu *et al.*²¹⁹. Bonded and LJ parameters for the $[\text{TCM}^-]$ anion were available only for the case of a $[\text{TCM}^-]$ IL that incorporated the cation 1-ethyl-1-methylphospholinium. These were found in a technical report by Martin *et al.*²³⁴ of a project that aimed at the development of a generic methodology for the parameterization of classical force fields for ILs, which, however, failed. Direct use of the $[\text{TCM}^-]$ LJ and bonded parameters from this report resulted in two orders of magnitude from experimental results on diffusivity, as will be shown below. The force field optimization procedure focused on (i) calculation of the effect of the charge distribution on the properties of interest, (ii) the appropriate choice of the charges' scaling factor to effectively incorporate polarizability and charge transfer effects and, at the same time, (iii) the necessary modification needed for the anion's LJ parameters in order to attain good agreement with the experimental data for the density and the self-diffusivity. The experimental data for density of $[\text{C}_4\text{mim}^+][\text{TCM}^-]$ used for comparison were taken from Ref. 107, whereas experimental measurement of the self-diffusion coefficient of $[\text{C}_4\text{mim}^+]$ was performed in the Institute of Chemical Reaction Engineering²³⁵ of the University of Erlangen-Nuremberg following the procedure that is described in Ref. 156.

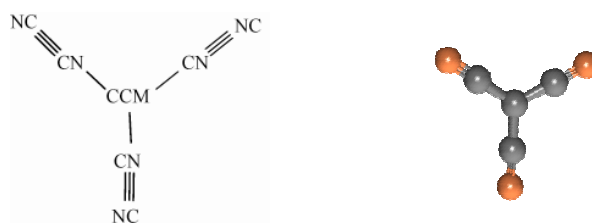
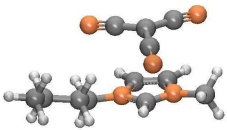
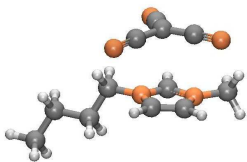
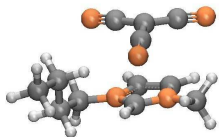
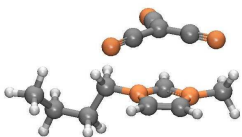


Figure 4.1: The labeling of the atoms of $[\text{TCM}^-]$.

The partial charges were calculated quantum mechanically using three different schemes. The calculations were performed using: (a) isolated ions, (b) four minimum energy conformations of the ion pair and (c) on two ion pairs of

[C₄mim⁺][TCM⁻] in order to meaningfully estimate the scaling factor of the atomic charge distribution to be used in the proposed force field. The charges as calculated on isolated ions will be abbreviated “ISO” and the charges as calculated using four minimum energy relevant conformations of the ionic pair will be referred to as “4RC”. All quantum mechanical calculations were performed by Dr. Jörg-Rüdiger Hill of Scienomics²⁰³ using Møller-Plesset perturbation theory (MP2). More information on the procedure followed for the calculation of the charges can be found in Ref. 236. In all charge distributions, necessary modifications were performed in the anion’s charges in order to reassure that atoms in symmetrical positions have the same charge. In Table 4.1 the four minimum energy conformations of [C₄mim⁺][TCM⁻] used to calculate the 4RC charges are shown together with the energy values of each conformation.

Table 4.1: The conformers of [C₄mim⁺][TCM⁻] and their relative energies as calculated by Scienomics²⁰³.

Structure	Relative MP2 energy / [kJ/mol]	Structure	Relative MP2 energy / [kJ/mol]
	0.0		4.7
	2.0		5.1

The mean total ionic charge obtained by the four relevant conformations is $\pm 0.7355e^-$ which is lower than $1e^-$ due to charge transfer effects. As already mentioned above, additional quantum mechanical calculations were performed on two ion pairs of [C₄mim⁺][TCM⁻] in order to meaningfully estimate the scaling factor of the atomic charge distribution to be used in the proposed force field. The total ionic charge from the two pairs of ions resulted in $\pm 0.710121e^-$, lower than the value obtained by the

conformations of one ionic pair, which is indicative of the strength of the charge transfer effects on these systems.

For each set of parameters, long MD simulations were performed following the procedure that is described at Section 4.1. In Table 4.2 the simulation results on density and diffusivity as calculated using directly the 4RC charges as obtained from the quantum mechanical calculations and different sets of LJ parameters are reported and compared with the experimental measurements. Using directly the anion's LJ parameters of Martin *et al.*²³⁴ resulted in 1.3% higher density compared to the experimental value whereas the value of the cation's self-diffusion coefficient is $0.05 \cdot 10^{-7} \text{ cm}^2/\text{s}$, two orders of magnitude lower than the experimental value which is $3.95 \cdot 10^{-7} \text{ cm}^2/\text{s}$ (see the first, highlighted line of Table 4.2).

Through systematic modification of only the anion's LJ parameters, an increase by an order of magnitude of the calculated self-diffusion coefficients was achieved, which, however, is still one order of magnitude lower than the experimental value. The best prediction of the cationic self-diffusivity using the 4RC charge scheme was obtained with a total 70 % reduction in the initial ϵ value of CCM (from 0.08 to 0.024 kcal/mol), 35 % reduction in the ϵ values of CN (from 0.2 to 0.13 kcal/mol) and NC (from 0.6 to 0.39 kcal/mol) (see the second highlighted line of Table 4.2) (see Fig. 4.1 for the labeling of the atoms of [TCM⁻]).

Subsequently, the effort was focused on the investigation of the appropriate scaling factor to reduce the total ionic charge in order to achieve better predictions of the transport properties. Necessary modest modifications in the LJ parameters were also performed at this stage in order to keep the deviation from the experimental density below 1.5%. The 4RC charge distribution was uniformly scaled to lower total ionic charge, namely to values $\pm 0.65e^-$ and $0.6e^-$.

Table 4.2: Simulation results for density and diffusivity of $[\text{C}_4\text{mim}^+][\text{TCM}^-]$ at 298.15 K using the 4RC set of charges and modified Lennard-Jones parameters for the anion. The deviation from the experimental density is stated in the parenthesis. (Note that: $R_{\text{mim}} = \sigma\sqrt[6]{2}$).

LJ for CCM		LJ for CN		LJ for NC		ρ (gr/cm ³)	D_{an} (10 ⁻⁷ cm ² /s)	D_{cat} (10 ⁻⁷ cm ² /s)
ϵ (kcal/mol)	$R_{\text{mim}}/2$ (Å)	ϵ (kcal/mol)	$R_{\text{mim}}/2$ (Å)	ϵ (kcal/mol)	$R_{\text{mim}}/2$ (Å)	Exp. ¹⁰⁷ 1.0473	-	Exp. ²³⁵ 3.95
0.08	1.99	0.2	1.75	0.6	1.85	1.061 (+1.3%)	0.05	0.05
0.08	2.2089	0.2	1.75	0.6	1.85	1.061 (+1.3%)	0.06	0.075
0.08	1.99	0.15	1.75	0.45	1.85	1.0537 (+0.6%)	0.1	0.16
0.06	1.99	0.15	1.75	0.45	1.85	1.047 (-0.02%)	0.26	0.18
0.04	1.99	0.15	1.75	0.45	1.85	1.0447 (-0.2%)	0.16	0.16
0.024	1.99	0.15	1.75	0.45	1.85	1.0417 (-0.5%)	0.32	0.25
0.052	1.99	0.13	1.75	0.39	1.85	1.038 (-0.9%)	0.37	0.28
0.4	1.99	0.13	1.75	0.39	1.85	1.035 (-1.2%)	0.42	0.38
0.024	1.99	0.13	1.75	0.39	1.85	1.032 (-1.5%)	0.56	0.6
0.024	1.0	0.13	1.75	0.39	1.85	1.032 (-1.5%)	0.58	0.38
0.06	1.99	0.15	1.75	0.24	1.85	1.0417 (-0.5%)	0.3	0.3
0.024	1.99	0.15	1.75	0.24	1.85	1.0356 (-1.1%)	0.4	0.3

In Table 4.3 the simulation results for density and diffusivity are shown along with the various anion's LJ-parameter-sets used together with the 4RC charge distribution uniformly scaled to $\pm 0.65e^-$. In the first highlighted line, the results using the unmodified LJ parameters for the anion are shown. It is interesting to compare these results to the ones shown in the first line of Table 4.2: only by uniformly scaling the 4RC charge distribution to give a $\pm 0.65e^-$ total ionic charge resulted in better

predictions for the density (only 0.5% deviation) and, more importantly, in two times faster self-diffusivities. By making modifications in the LJ parameters, we obtained one and a half orders of magnitude higher diffusivities and only 0.1% deviation from the experimental density, as shown in second highlighted row of Table 4.3. These results were obtained by lowering 70 % in total the ϵ value of CCM (from 0.08 to 0.024 kcal/mol), by 35 % the ϵ values of CN (from 0.2 to 0.13 kcal/mol) and NC (from 0.6 to 0.39 kcal/mol) and by reducing the $R_{\text{min}}/2$ of NC from 1.85 to 1.75 Å (see Fig. 4.1 for the labeling of the atoms of [TCM⁻]).

Table 4.3: Simulation results for density and diffusivity of [C₄mim⁺][TCM⁻] at 298.15 K using the 4RC scaled at 0.65e⁻ set of charges and modified Lennard-Jones parameters for the anion. The deviation from the experimental density is stated in the parenthesis.

LJ for CCM		LJ for CN		LJ for NC		ρ (gr/cm ³)	D_{an} (10 ⁻⁷ cm ² /s)	D_{cat} (10 ⁻⁷ cm ² /s)
ϵ (kcal/mol)	$R_{\text{min}}/2$ (Å)	ϵ (kcal/mol)	$R_{\text{min}}/2$ (Å)	ϵ (kcal/mol)	$R_{\text{min}}/2$ (Å)	Exp. ¹⁰⁷ 1.0473	-	Exp. ²³⁵ 3.95
0.08	1.99	0.2	1.75	0.6	1.85	1.0532 (+0.5%)	0.17	0.1
0.08	1.99	0.15	1.75	0.45	1.85	1.0335 (-1.3%)	0.65	0.4
0.08	1.99	0.15	1.5	0.45	1.85	1.0318 (-1.5%)	1.4	1.0
0.08	1.99	0.15	1.85	0.45	1.85	1.0288 (-1.7%)	0.62	0.47
0.024	1.99	0.13	1.75	0.39	1.7	1.0624 (+1.4%)	1.85	1.45
0.024	1.99	0.13	1.75	0.39	1.75	1.0483 (-0.1%)	1.8	1.6

In Table 4.4 the simulation results for density and diffusivity of [C₄mim⁺][TCM⁻] at 298.15 K and 363.14 K are shown with the various anion's LJ parameter sets used together with the 4RC charge distribution uniformly scaled to a $\pm 0.6e^-$ total ionic charge. Results using the data set that performed at best with the 4RC charge distribution scaled to $\pm 0.65e^-$ are also shown for comparison. Lowering the ions' total charge to 0.6e⁻ and slightly modifying the anion's LJ parameters to preserve accuracy in the density resulted in less than 40% deviation for the cation's self-diffusion coefficient as shown in the highlighted row of Table 4.4. The corre-

sponding LJ parameter set of this set of charges differ from the one with the 4RC charges scaled to $0.65e^-$ only in the value of $R_{\text{mim}}/2$ of NC which was lower and equal to 1.7 \AA .

Table 4.4: Optimized Lennard-Jones parameters for [TCM⁻] anion and simulation results for [C₄mim⁺][TCM⁻] at 298.15 K and 363.14 K using charges from the 4RC procedure.

<i>T</i> (K)	Total Ion Charge (e^-)	LJ for CCM		LJ for CN		LJ for NC		ρ (gr/cm ³)	D_{an} (10 ⁻⁷ cm ² /s)	D_{cat} (10 ⁻⁷ cm ² /s)
		ϵ (kcal/ mol)	$R_{\text{mim}}/2$ (\AA)	ϵ (kcal/ mol)	$R_{\text{mim}}/2$ (\AA)	ϵ (kcal/ mol)	$R_{\text{mim}}/2$ (\AA)	Exp. ¹⁰⁷ 1.0473	-	Exp. ²³⁵ 3.95
298. 15	0.65	0.024	1.99	0.13	1.75	0.39	1.75	1.0483 (-0.1%)	1.8	1.6
363. 14	0.65	0.024	1.99	0.13	1.75	0.39	1.75	0.9968 (-0.8%)	12.4	10.4
298. 15	0.6	0.024	1.99	0.13	1.75	0.39	1.7	1.0518 (+0.4%)	3.48	2.45
363. 14	0.6	0.024	1.99	0.13	1.75	0.39	1.7	0.9992 (-0.5%)	16.7	13.9

The performance of the set of charges obtained by quantum mechanical calculations on the isolated ions (ISO) was also tested having them first uniformly scaled to various values of total ionic charge, such as $0.75e^-$, $0.7e^-$ and $0.65e^-$ and using different LJ parameters. In Table 4.5 the optimum LJ parameter sets are shown as used with the ISO charge distribution scaled to $0.7e^-$ and $0.65e^-$ with the results on density and ions' self-diffusivities for [C₄mim⁺][TCM⁻] at 298.15 K and 363.14 K. The best agreement on both density and self-diffusivity calculations with the experimental data were obtained using the ISO charge distribution scaled to $0.65e^-$ (see two last rows of Table 4.5): the deviation between the calculated and the experimental value is less than 7% which is lower than the uncertainty in both experimental measurements and in simulation results.

In the analysis that follows, the ISO scheme was chosen to be used aiming at retaining a degree of transferability in the proposed force field. The ISO set of charges scaled to $0.7e^-$ total ionic charge is chosen to be used as being the optimum one to realistically represent the IL systems at hand according to the quantum mechanical calculations performed on a small ion cluster of [C₄mim⁺][TCM⁻] that resulted in an

average value of $\pm 0.71e^-$ for each ion (see Fig. 4.2). The deviation between experimental and calculated self-diffusivity values is reasonably low at 298.15 K whereas the lack of experimental data for diffusivity at 363.15 K hinders the validation at higher temperatures. The final values of the anion's LJ parameters that are proposed to be used with the ISO charge scheme scaled to $\pm 0.7e$ are shown in the highlighted rows of Table 4.5.

Table 4.5: Optimized Lennard-Jones parameters for [TCM⁻] anion and simulation results for [C₄mim⁺][TCM⁻] at 298.15 K and 363.14 K using charges from the ISO procedure.

<i>T</i> (K)	Total Ion Charge (e ⁻)	LJ for CCM		LJ for CN		LJ for NC		ρ (gr/cm ³)	D_{an} (10 ⁻⁷ cm ² /s)	D_{cat} (10 ⁻⁷ cm ² /s)
		ϵ (kcal/ mol)	$R_{min}/2$ (Å)	ϵ (kcal/ mol)	$R_{min}/2$ (Å)	ϵ (kcal/ mol)	$R_{min}/2$ (Å)	Exp. ¹⁰⁷ 1.0473	-	Exp. ²³⁵ 3.95
298. 15	0.7	0.024	1.99	0.13	1.75	0.39	1.7	1.0556 (+0.8%)	2.4	2.0
363. 14	0.7	0.024	1.99	0.13	1.75	0.39	1.7	1.0031 (-0.2%)	-	-
298. 15	0.7	0.024	1.99	0.13	1.75	0.39	1.72	1.050 (+0.3%)	2.8	2.7
363. 14	0.7	0.024	1.99	0.13	1.75	0.39	1.72	0.9979 (-0.7%)	-	-
298. 15	0.65	0.024	1.99	0.13	1.75	0.39	1.685	1.0506 (+0.3%)	3.69	3.69
363. 14	0.65	0.024	1.99	0.13	1.75	0.39	1.685	0.9960 (-0.7%)	19.4	17.7

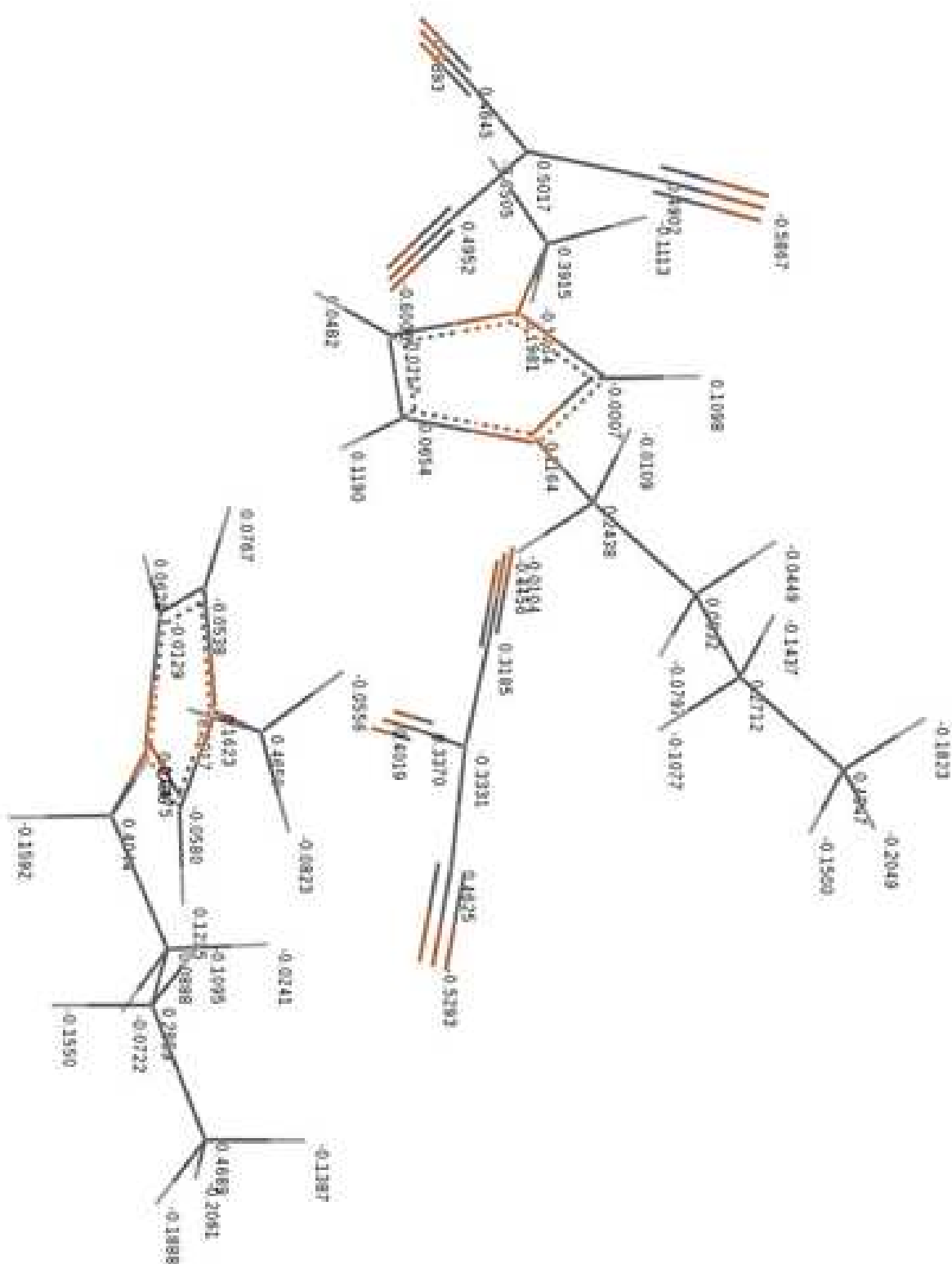


Figure 4.2: The structure of two pairs of $[C_4mim^+][TCM^-]$ with charges obtained quantum mechanically.

4.3 Force Field Validation and Prediction of Properties

The proposed force field that was optimized for the case of $[\text{C}_4\text{mim}^+][\text{TCM}^-]$ at 298.15 K is validated against experimental data by performing MD simulations at various temperatures. At the same time, the transferability of the new parameters for $[\text{TCM}^-]$ when paired with other imidazolium-based cations having different alkyl chain lengths was also studied. For this, simulations of three ILs, namely, $[\text{C}_2\text{mim}^+][\text{TCM}^-]$, $[\text{C}_4\text{mim}^+][\text{TCM}^-]$ and $[\text{C}_8\text{mim}^+][\text{TCM}^-]$, were performed at three temperatures: 298.15 K, 363.14 K and 398.15 K, and at atmospheric pressure.

4.3.1 Density and Structure Properties

Simulation results on density for the three ILs are shown in Figure 4.3 against experimental data^{16,107,109,237-239} versus temperature and, also, in Table B9 of Appendix B. The deviation between experimental data and simulation results is below than 1.3% for $[\text{C}_2\text{mim}^+][\text{TCM}^-]$, 0.9% for $[\text{C}_4\text{mim}^+][\text{TCM}^-]$ and 1.8% for $[\text{C}_8\text{mim}^+][\text{TCM}^-]$ at all temperatures.

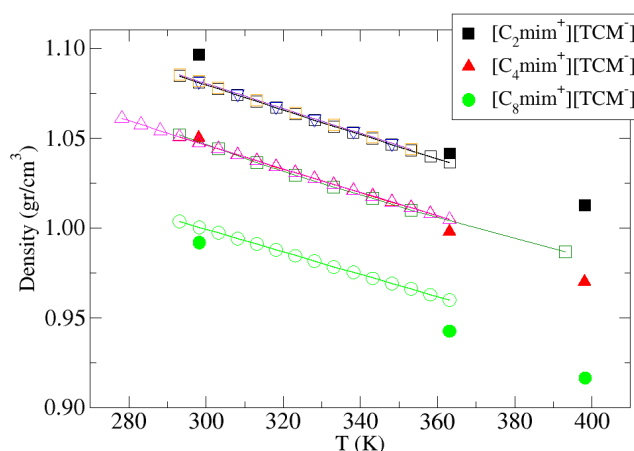


Figure 4.3: MD predictions for the density of $[\text{C}_n\text{mim}^+][\text{TCM}^-]$, $n = 2, 4, 8$ (full points). The lines with open points are experimental data for $[\text{C}_2\text{mim}^+][\text{TCM}^-]$ ^{107,237-238}, $[\text{C}_4\text{mim}^+][\text{TCM}^-]$ ^{16,107,239} and $[\text{C}_8\text{mim}^+][\text{TCM}^-]$ ¹⁰⁹.

Radial distribution functions (RDFs) between ions' centers of mass and between various atoms of the ions' have been calculated in order to study the microscopic structure of the ILs. In Figure 4.4 the RDFs between the centers of mass for anion-anion, anion-cation and cation-cation interactions are shown for (a) $[\text{C}_4\text{mim}^+][\text{TCM}^-]$, (b) $[\text{C}_4\text{mim}^+][\text{TCM}^-]$ and (c) $[\text{C}_8\text{mim}^+][\text{TCM}^-]$ at 298.15 K. Due

to the strong interaction between ions carrying opposite charge, the highest maximum is observed for the anion-cation RDF at 5 Å. The anion-anion RDF has two maxima: a small one at around 4 Å and a higher at 9 Å. This is unlike the anion-anion RDF calculated for $[C_n\text{mim}^+][\text{Tf}_2\text{N}^-]$ ILs (see Figure 2.2) that exhibits only one maximum at around 9 Å. The existence of this second, smaller maximum at short distance is attributed to the smaller size of the $[\text{TCM}^-]$ that allows a more uniform distribution of the anion around the cations compared to the case of the $[\text{Tf}_2\text{N}^-]$ ILs.

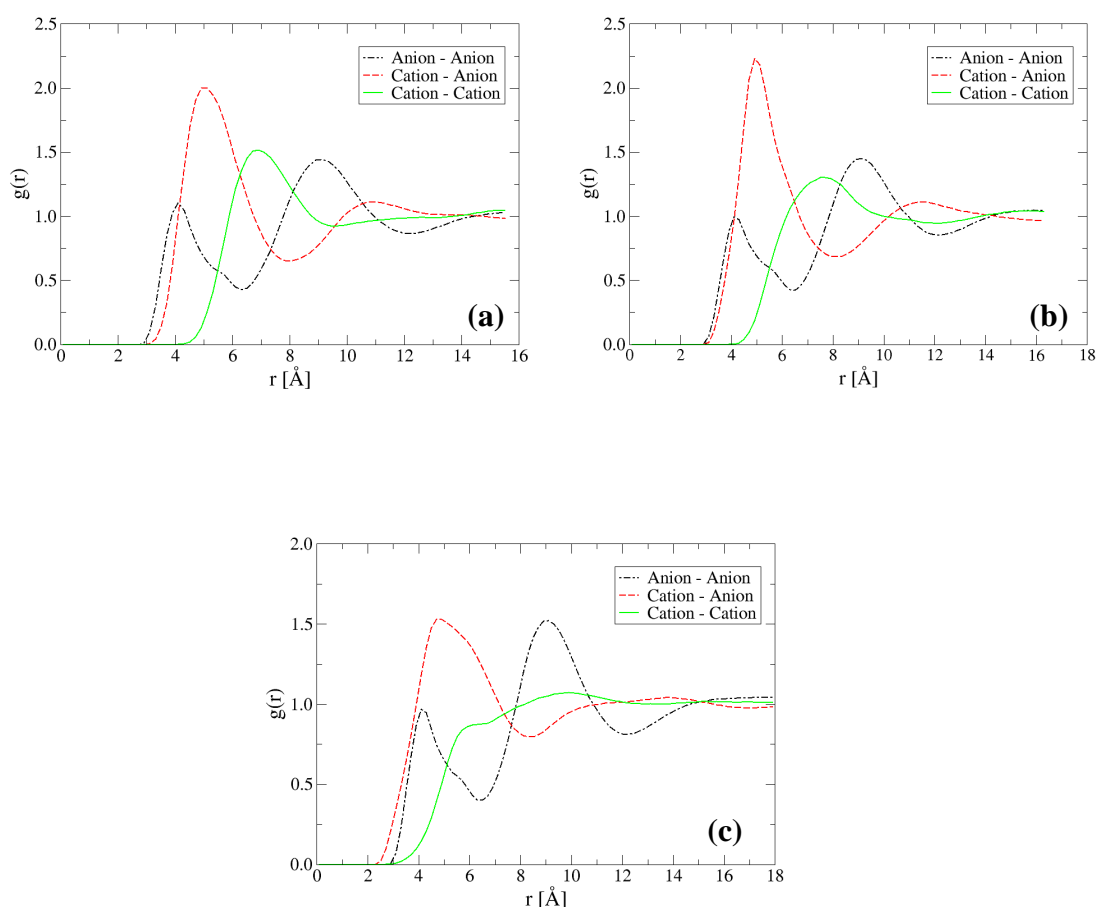


Figure 4.4: Radial distribution function $g(r)$ for the anion-anion (black), anion-cation (red) and cation-cation (green) center of mass of (a) $[\text{C}_2\text{mim}^+][\text{TCM}^-]$, (b) $[\text{C}_4\text{mim}^+][\text{TCM}^-]$ and (c) $[\text{C}_8\text{mim}^+][\text{TCM}^-]$ at 298.15 K.

Interestingly, the behaviour of the anion-cation $g(r)$ does not follow the same behaviour as the $[\text{Tf}_2\text{N}^-]$ ILs (see Figure 2.3) where the peak of the anion-cation $g(r)$ decreases as the alkyl tail becomes longer. In the $[\text{TCM}^-]$ ILs, the peak is less intense in $[\text{C}_2\text{mim}^+][\text{TCM}^-]$ (red line in Figure 4.4a), increases in $[\text{C}_4\text{mim}^+][\text{TCM}^-]$ (red line

in Figure 4.4b) to decrease again in $[\text{C}_8\text{mim}^+][\text{TCM}^-]$ (red line in Figure 4.4c). This behaviour is attributed to the location of the center of mass, which probably coincides with a more preferential position for the anion in the case of $[\text{C}_4\text{mim}^+][\text{TCM}^-]$.

More information on the microscopic structure can be obtained from RDFs between specific atoms on the ions. In Figure 4.5 the RDFs between the terminal carbons of the cation's alkyl tail are plotted for the three ILs at 298.15 K. For all the three ILs there is one maximum at around 4 Å that becomes more intense as the alkyl tail becomes longer, thus indicating the existence of tail aggregation phenomena. This is in accordance with previous simulation studies^{44,46,48-49,59} of imidazolium-based ILs and is attributed⁴⁹ to the almost neutral charge of the alkyl tail that results in stronger short-ranged van der Waals interactions which lead to the formation of almost neutrally charged non-polar domains. Comparison between the respective $g(r)$ for the cations' terminal carbon atoms in the $[\text{Tf}_2\text{N}^-]$ ILs at 298.15 K (Figure 2.4) reveals that there is a stronger tail aggregation phenomena in the $[\text{TCM}^-]$ ILs (Figure 2.5): the peak of $g(r)$ for the case of $[\text{C}_4\text{mim}^+][\text{Tf}_2\text{N}^-]$ is 1.75, whereas for the case of $[\text{C}_4\text{mim}^+][\text{TCM}^-]$ is 1.9 and, the peak of $g(r)$ for the case of $[\text{C}_8\text{mim}^+][\text{Tf}_2\text{N}^-]$ is 1.8, whereas for the case of $[\text{C}_8\text{mim}^+][\text{TCM}^-]$ is 2.25.

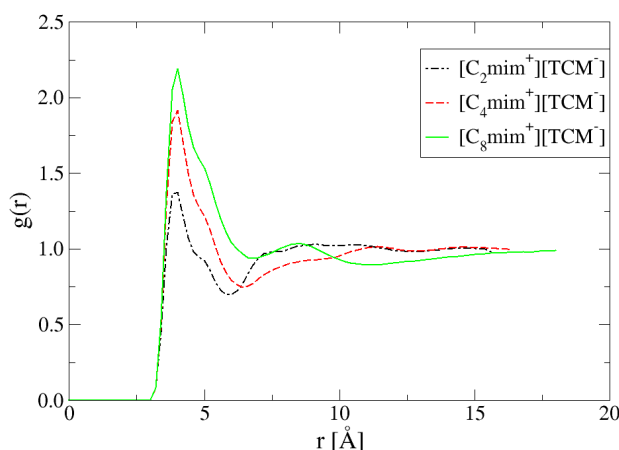


Figure 4.5: Radial distribution function $g(r)$ between the terminal carbon atoms in the cation's alkyl chain of $[\text{C}_2\text{mim}^+][\text{TCM}^-]$ (black), $[\text{C}_4\text{mim}^+][\text{TCM}^-]$ (red) and $[\text{C}_8\text{mim}^+][\text{TCM}^-]$ (green) at 298.15 K.

At the same time, as the alkyl tail becomes longer the anion is found to be more strongly correlated with the imidazolium ring that carries the highest positive charge,

as shown in Figure 4.6 where the RDFs between the C2 carbon which is located on the most charged part of the imidazolium ring and the most negatively charged atom of the anion, the nitrogen NC, are plotted for all three ILs at 298.15 K. The first, intense maximum appears at all cases at around 3 Å, whereas there are two small peaks at longer distances which correspond to the other two, same-type nitrogens NC.

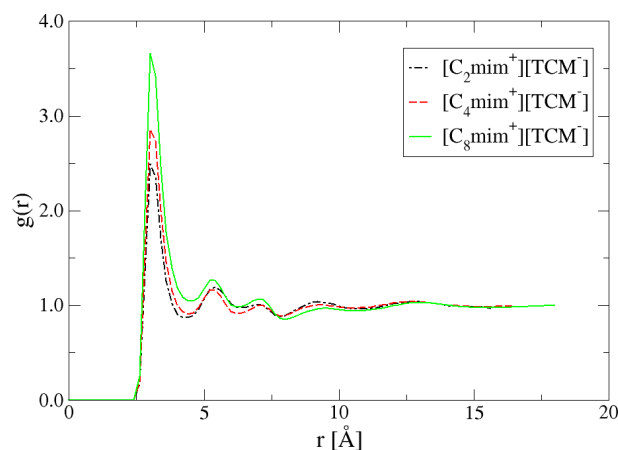


Figure 4.6: Radial distribution function $g(r)$ between the C2 carbon of the cation's imidazolium ring and the NC nitrogen of the anion for $[C_2mim^+][TCM^-]$ (black), $[C_4mim^+][TCM^-]$ (red) and $[C_8mim^+][TCM^-]$ (green) at 298.15 K.

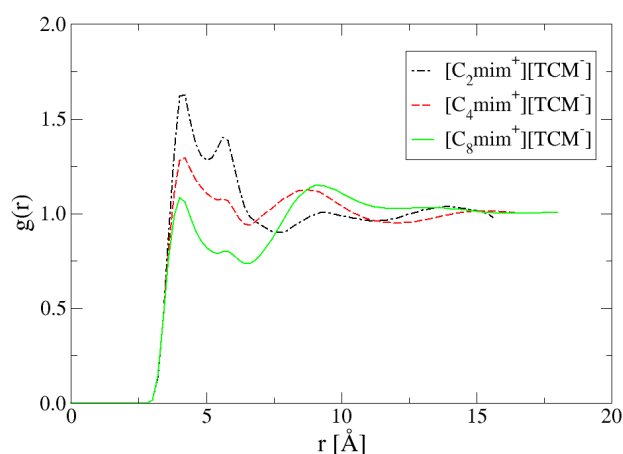


Figure 4.7: Radial distribution function $g(r)$ between the terminal carbon of the cation's alkyl tail and the central carbon CCM of the anion for $[C_2mim^+][TCM^-]$ (black), $[C_4mim^+][TCM^-]$ (red) and $[C_8mim^+][TCM^-]$ (green) at 298.15 K.

Similarly, the anion's oxygen atoms in the $[\text{Tf}_2\text{N}]^-$ ILs, that are the most negatively charged atoms, are found to be located near the C2 carbon atom of the imidazolium ring near which the highest positive charge is located (see Figure 2.5). The fact that $[\text{TCM}]^-$ is stronger correlated with the charged part of the cation for the cases of longer alkyl tails is also established by the fact that $[\text{TCM}]^-$ is found to be less associated with the terminal part of the almost neutral alkyl tail (see Figure 4.7).

The relative configuration of the anion with respect to the imidazolium ring is investigated by calculation of radial angular distribution functions $g(r, \theta)$ with r being the distance between the C2 carbon atom in the imidazolium ring and the NC nitrogen of the anion, and θ being either the angle that is formed by the vector \mathbf{r} and the plane of the imidazolium ring (Figure 4.8) or the angle that is formed by the plane of the imidazolium ring and the mean plane of the anion (Figure 4.9). In both Figures, the green areas correspond to values of r and θ of higher probability.

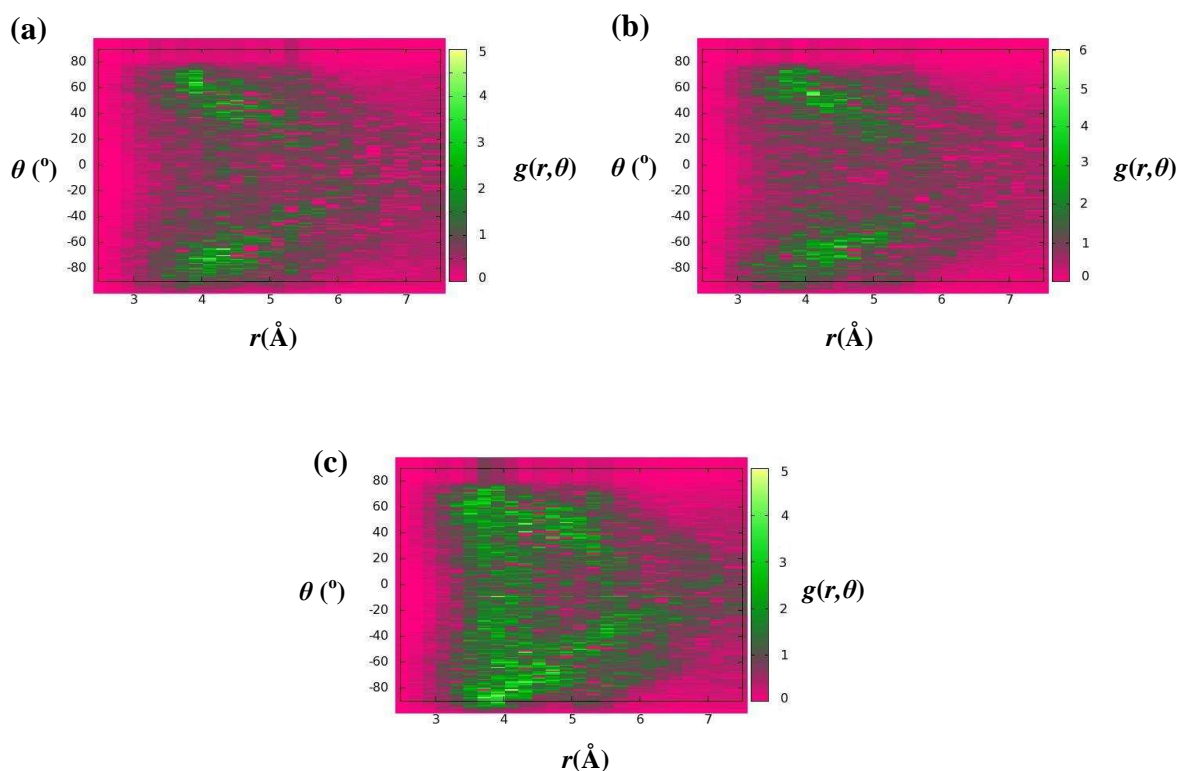


Figure 4.8: Radial Angular Distribution Functions (RADF) for (a) $[\text{C}_2\text{mim}^+][\text{TCM}^-]$, (b) $[\text{C}_4\text{mim}^+][\text{TCM}^-]$ and (c) $[\text{C}_8\text{mim}^+][\text{TCM}^-]$ at 298.15 K with r being the distance between the C2 carbon atom of the imidazolium ring and the NC nitrogen atom of the anion and θ is the angle formed by the main plain of the imidazolium ring and the vector \mathbf{r} .

Figure 4.8 can be directly compared to Figure 2.8 where the RADFs for the $[\text{Tf}_2\text{N}^-]$ ILs are shown with r being the distance between the C2 carbon atom and θ the angle between the vector, \mathbf{r} , and the mean plane of the imidazolium ring. Unlike the $[\text{Tf}_2\text{N}^-]$ ILs where the anion was clearly found above and below the imidazolium ring, the $[\text{TCM}^-]$ anion is found to be more uniformly distributed around the imidazolium ring: the areas with the highest probability span all the range of the angles, especially for the longer alkyl tails as can be seen in Figure 4.8c for the case of $[\text{C}_8\text{mim}^+][\text{TCM}^-]$. For the cases of $[\text{C}_2\text{mim}^+][\text{TCM}^-]$ and $[\text{C}_4\text{mim}^+][\text{TCM}^-]$, two areas below and above the imidazolium ring are found to be more likely occupied by anions, but this is not as clear as in the case of the $[\text{Tf}_2\text{N}^-]$ ILs (Figure 2.7).

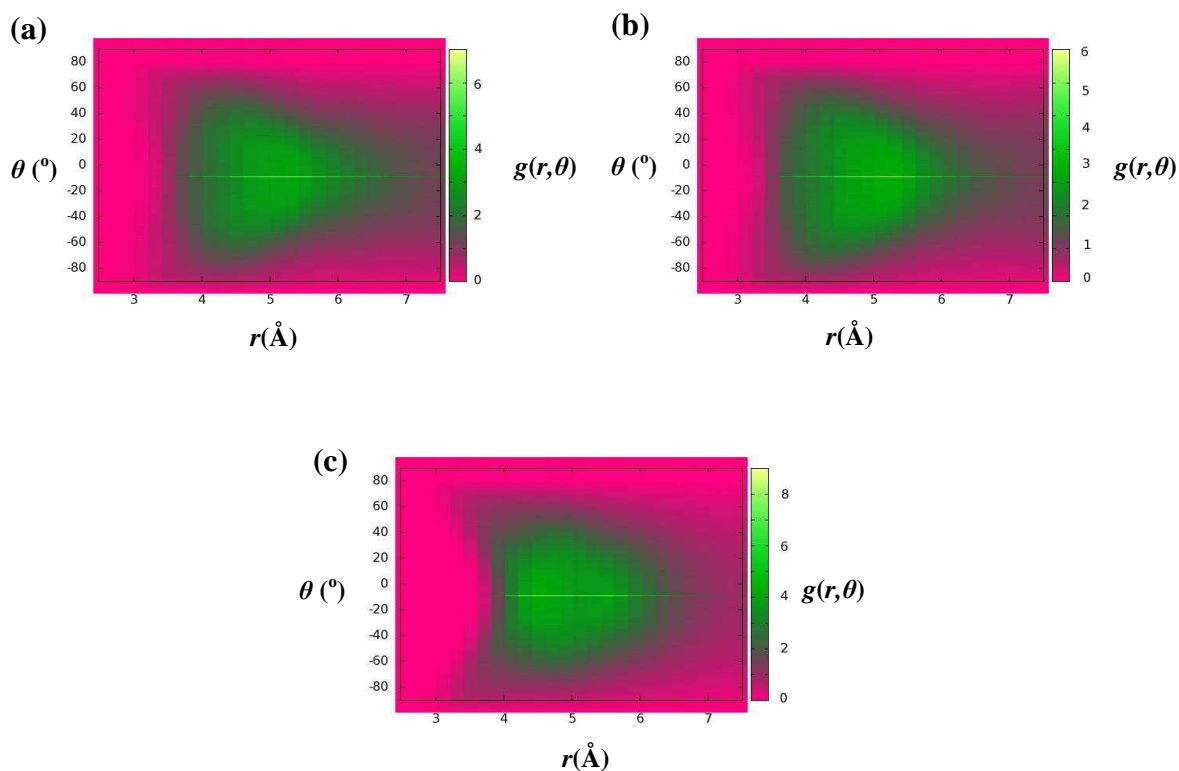


Figure 4.9: Radial Angular Distribution Functions (RADF) for (a) $[\text{C}_2\text{mim}^+][\text{TCM}^-]$, (b) $[\text{C}_4\text{mim}^+][\text{TCM}^-]$ and (c) $[\text{C}_8\text{mim}^+][\text{TCM}^-]$ at 298.15 K with r being the distance between the C2 carbon atom of the imidazolium ring and the NC nitrogen atom of the anion and θ is the angle formed by the main plain of the imidazolium ring and the main plane of the anion.

The relative orientation of the anion with respect to the imidazolium ring is analyzed by RADFs with r being the distance between the C2 carbon atom of the imidazolium ring and the NC nitrogen atom of the anion and θ is the angle formed by the main plain of the imidazolium ring and the main plane of the anion were

calculated and are shown in Figure 4.9 for all ILs at 298.15 K. It becomes clear from these plots that there is no preferential orientation of the anion with respect to the cation's imidazolium ring.

4.3.2 Transport Properties

Then Einstein relationship (Eq. 2.9) was used for the calculation of the self-diffusion coefficients of the ions' center of mass in the Fickian regime which is identified by a slope being equal to unity in the $\log(\text{MSD})$ versus $\log(t)$ plot.

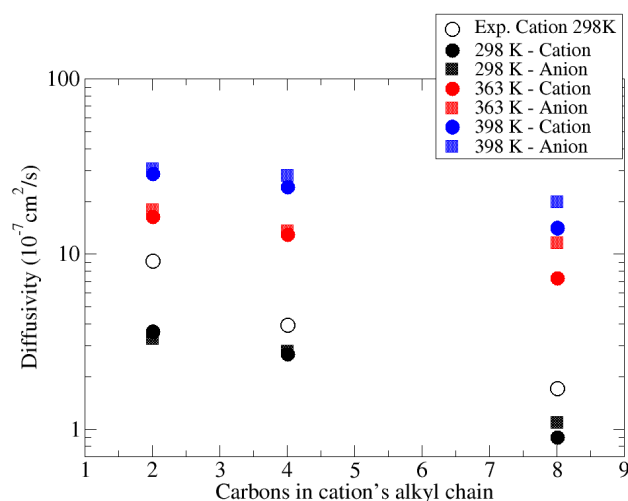


Figure 4.10: Self-diffusion coefficients of the anion (circles) and the cation (squares) versus the atom of carbon atoms in the cation's alkyl tail as calculated at 298.15 K (black), 363.15 K (red) and 398.15 (blue). The open circles are the experimental measurements (see acknowledgments) of the cation's diffusivity at 298.15 K.

In Figure 4.10 the calculated ions' diffusivities for the three ILs at all temperatures are plotted as a function of the number of the carbon atoms in the cation's alkyl tail. Experimental NMR measurements²³⁵ for the cations' diffusivity at 298.15 K for all ILs are also plotted for comparison and appear to be in satisfactory agreement with the simulation results. It is also obvious from Figure 4.10 that as the alkyl tail becomes longer the ions' diffusivity decreases. For the case of smaller (and lighter) cations e.g. $[\text{C}_2\text{mim}^+]$ (mass 111.1645 amu) that has a mass comparable to one of the $[\text{TCM}^-]$ anion (90.0629 amu), the self-diffusion coefficients of the two counterions are similar. As the cation's alkyl tail becomes longer, and thus the cation heavier (mass of $[\text{C}_4\text{mim}^+] = 139.2175$ amu, mass of $[\text{C}_8\text{mim}^+] = 195.3235$ amu), the anion's self-diffusion coefficient is systematically higher at all temperatures. How-

ever, no experimental data on anions diffusivity are currently available. The calculated ionic diffusivities are also given in Table B10 of Appendix B.

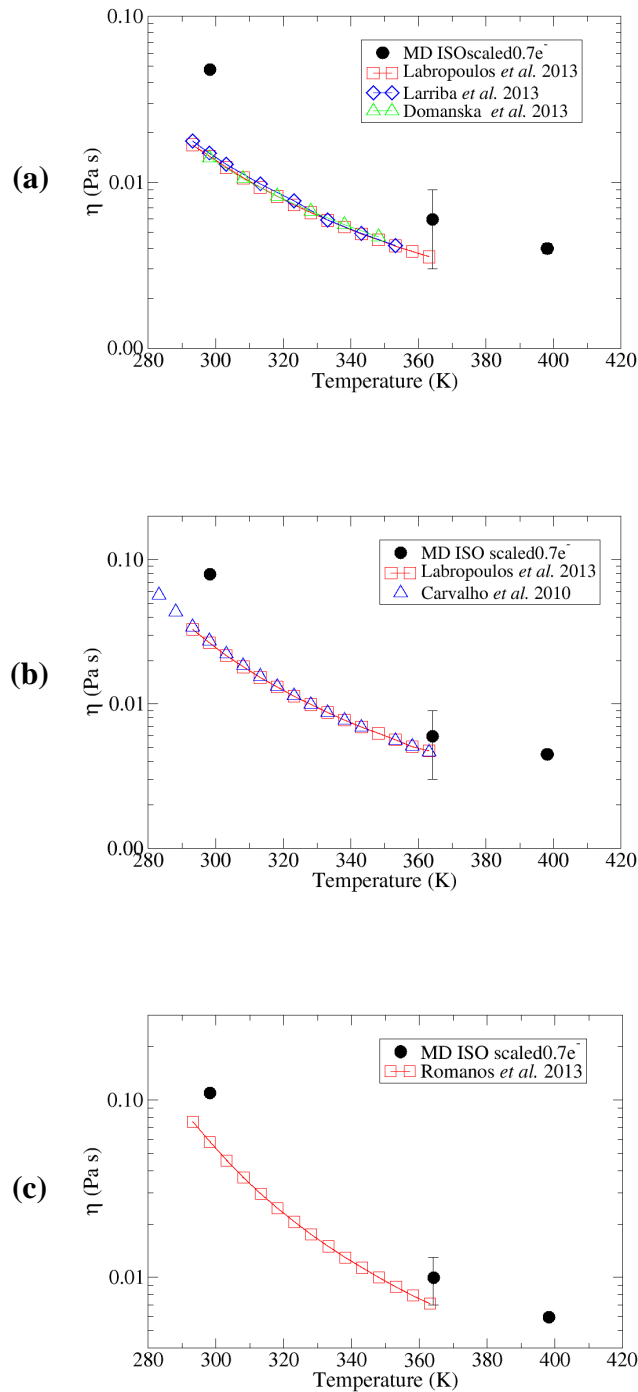


Figure 4.11: Viscosity calculations from simulation (full points) as a function of temperature against experimental data (lines with open points) for (a) $[C_2mim^+][TCM]^{107,238,240}$, (b) $[C_4mim^+][TCM]^{107,239}$ and (c) $[C_5mim^+][TCM]^{109}$.

Shear viscosity calculations were performed using the Green-Kubo relationship (Eq. 2.11) by integrating the stress correlation function calculated at the last section of each productive NVT run during which the information of the pressure was stored each 8 fs. The viscosity was estimated by the integral plateau value after re-assuring that the pressure autocorrelation function was fluctuating around zero. In Figure 4.11 shear viscosity calculations for (a) $[\text{C}_2\text{mim}^+][\text{TCM}^-]$, (b) $[\text{C}_4\text{mim}^+][\text{TCM}^-]$ and (c) $[\text{C}_8\text{mim}^+][\text{TCM}^-]$ are shown as a function of temperature and are compared to experimental data^{107,109,238-240}. The agreement between the experimental and the predicted values is reasonably good with the temperature dependence of the viscosity being captured quite well for all ILs. There is a very small overestimation in the predicted values in accordance with the slightly higher values of the self-diffusivities; nevertheless, this difference is acceptable since shear viscosity, being a collective property, is prone to errors both in terms of simulation (sensitivity of the stress correlation function the intra-molecular vibrational modes) and experiment (sensitivity to impurities). Shear viscosity calculations are also provided in Table B11 of Appendix B.

4.3.3 Anisotropy in Cation's Translational Motion

The translational motion of the cations' center of mass was analyzed along axes specified by their geometry as described in Section 3.4.1 for the $[\text{TF}_2\text{N}^-]$ ILs. In particular, the displacement of a center of mass during a time interval $t - t_0$ was projected to the axes specified by the cation's geometry at time t_0 : the vector NN that connects the two nitrogens in the imidazolium ring, the normal vector to the imidazolium ring, the vector NNp that is perpendicular to the former and the end-to-end vector N3-Ct of the alkyl tail (see Figure 4.12).

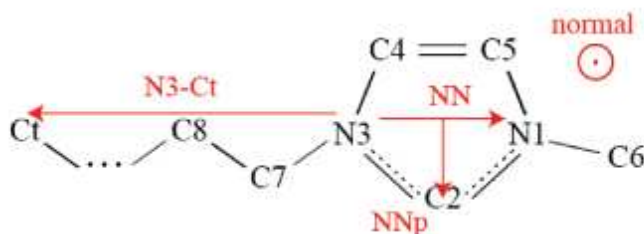


Figure 4.12: The vectors defined on the cation along which the translational motion of the center of mass was analyzed.

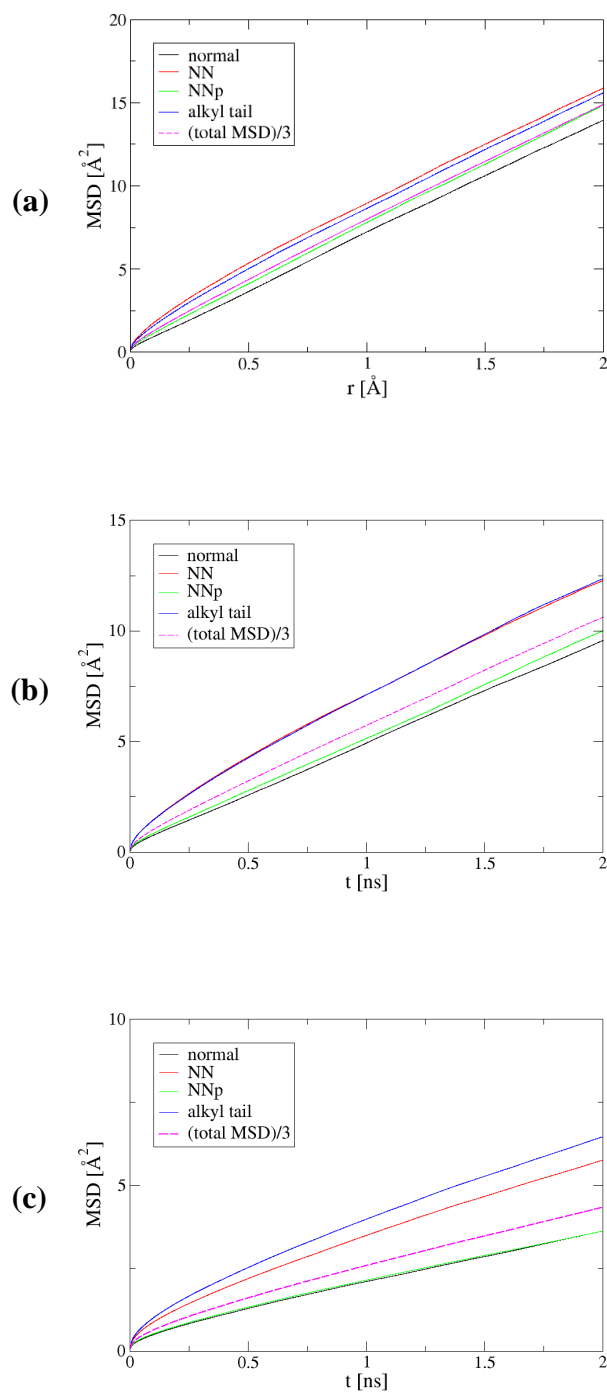


Figure 4.13: Mean square displacement (MSD) at 298.15 K calculated along the direction of the cations' vectors NN (red), NNp (green), the normal to them vector (red) and the alkyl tail (blue) compared to the 1/3 of the total MSD of the center of mass for (a) $[\text{C}_2\text{mim}^+][\text{TCM}^-]$, (b) $[\text{C}_4\text{mim}^+][\text{TCM}^-]$ and (c) $[\text{C}_8\text{mim}^+][\text{TCM}^-]$.

In Figure 4.13 the mean square displacements (MSDs) along these axes are plotted against the 1/3 of the total MSD for the three ILs at 298.15 K. The movement

along the axes for the $[\text{C}_2\text{mim}^+]$ cation, which has the shortest alkyl tail, has very small deviations from what is expected by the total MSD. However, there is a slightly enhanced movement along the NN vector, a fact that becomes more pronounced as the alkyl tail becomes longer. In the case of $[\text{C}_8\text{mim}^+]$, the alkyl tail has become heavier than the rest of the cation, and this results in a 50% higher MSD along the N3-Ct vector of the alkyl tail than the 1/3 of the total MSD.

These findings are in accordance with the results concerning the $[\text{Tf}_2\text{N}^-]$ ILs presented in Chapter 3 and also with the similar observations of Liu and Maginn⁵¹ for $[\text{C}_4\text{mim}^+][\text{Tf}_2\text{N}^-]$. This anisotropy in the cations' translational motion is preserved over long timescales and is preserved even in the Fickian regime at 298.15 K. As the temperature increases this behaviour is observed only in $[\text{C}_4\text{mim}^+][\text{TCM}^-]$ and $[\text{C}_8\text{mim}^+][\text{TCM}^-]$ and is present only in short times scales.

4.3.4 Cluster Formation of Dynamically Distinguishable Ions

Following the analysis presented in Section 3.4.2, the heterogeneity in the dynamics of $[\text{TCM}^-]$ ILs is quantified by the calculation of the non-Gaussian parameter $\alpha_2(t)$ (Eq. 3.2).

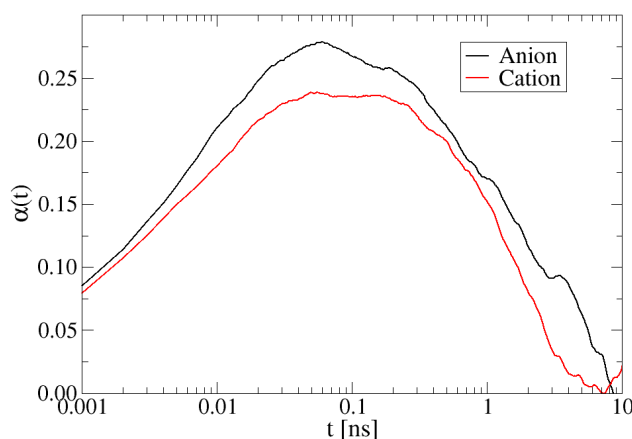


Figure 4.14: Non-Gaussian parameter $\alpha_2(t)$ for the anion (black) and the cation (red) of $[\text{C}_4\text{mim}^+][\text{TCM}^-]$ calculated at 298.15 K.

Figure 4.14 depicts the presence of dynamic heterogeneity in $[\text{C}_4\text{mim}^+][\text{TCM}^-]$ at 298.15 K. In case of a Gaussian distribution of $|\mathbf{r}_i(t) - \mathbf{r}_i(t_0)|$, $\alpha_2(t)$ is zero while any deviations from it indicate the presence of heterogeneities in the dynamics. As the temperature increases, $\alpha_2(t)$ reaches zero faster whereas its maximum is less intense

and is observed at shorter timescales being in accordance with similar observations made for [Tf₂N⁻] ILs (Section 3.4.2).

The presence of dynamically distinguishable ions is quantified by the deviation of the self-part of the van Hove function $G_s(\mathbf{r}, t)$ (Eq. 3.3) from the expected Gaussian distribution (Eq. 3.6). The $G_s(\mathbf{r}, t)$ is the probability that a particle is at position $\mathbf{r}_i(t)$ at time t given that it was located at $\mathbf{r}_i(0)$ at time 0. From the deviations of the $G_s(\mathbf{r}, t)$ from the Gauss distribution at short and long distances one can identify ions that have moved less or more than the expected. The same procedure as presented in detail in Section 3.4.2 was followed here for the identification of these ions.

The percentage of the ions that cause the deviations from the Gaussian distribution is found to be around 8% for all ILs at 298.15 K. RDFs between ions that are found to move faster and slower than the expected have been calculated in order to study how these ions are correlated in space. In Figure 4.15 RDFs between dynamically distinguishable ions of [C₄mim⁺][TCM⁻] at 298.15 K are plotted against the total $g(r)$

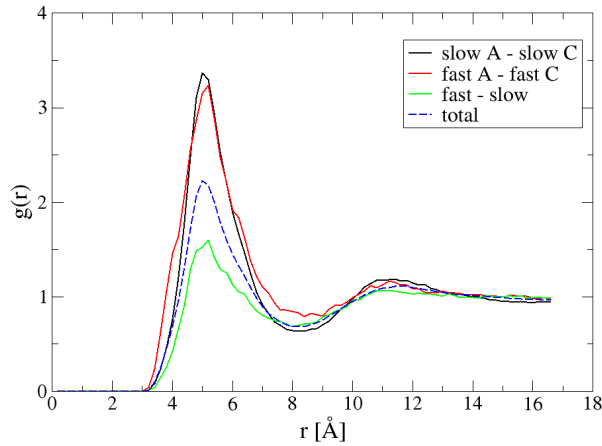


Figure 4.15: Radial distribution functions between the centers of mass of slow anions – slow cations (black), fast anions – fast cations (red) and fast – slow anions and cations (green) plotted against the total $g(r)$ (blue dotted line) as calculated without any discrimination on the dynamic nature of the ions. Calculated for [C₄mim⁺][TCM⁻] at 298.15 K for $t = 500$ ps.

as calculated with no discrimination on the dynamic behaviour of the ions. All the RDFs have the same pattern and their maxima appear at the same distances. However, the RDFs between fast anions – fast cations and slow anions – slow cations exhibit a

much more intense maximum compared to the total RDF whereas, on the other hand, the RDF between fast and slow ions has a much lower maximum. Same observations have been made for all ILs under study and for the cation-cation and anion-anion RDFs as well. These findings indicate the formation of clusters in the bulk that are compromised by dynamically distinguishable ions being in accordance with similar findings for the [Tf₂N⁻] ILs.

4.4 Conclusions

A classical atomistic force field is proposed for imidazolium-based ILs that incorporate the anion tricyanomethanide ([TCM⁻]). The optimization of the force field was performed on the basis of only the density and cation's self-diffusion coefficient of [C₄mim⁺][TCM⁻] at 298.15 K and 1 bar by tuning the Lennard-Jones parameters of the anion and simultaneously testing various charge distributions. The charge distribution that is based on quantum mechanical calculations performed on isolated ions is finally chosen as it has the asset of transferability, unlike the charge distributions calculated on four minimum configurations of the ion pair. Polarizability and charge transfer effects are incorporated in a simplified effective way into the system by uniformly scaling the atomic charges to yield an ions' total charge of $\pm 0.7e$ as dictated by the quantum mechanical study performed on a small ion cluster.

The performance of the optimized force field was tested at higher temperatures, namely 363.15 K and 398.15 K, and for ILs with cations having shorter and longer alkyl tails. The good agreement between the predicted and the measured densities and transport properties of all ILs under study confirms the good performance of the force field for imidazolium-based [TCM⁻] ILs. The proposed force field captures well the temperature dependence of the density and the viscosity, whereas the lack of experimental data on self-diffusivities at higher temperatures hinders the verification of its predictive ability at higher temperatures. The anion is found to be more mobile than cations with long alkyl tails, whereas it has comparable self-diffusivities with the smaller and equally heavy cation [C₂mim⁺].

Further analysis on the ions' translational motion revealed anisotropy in the cations' translational motion with an enhanced movement along the vector that connects the two nitrogen atoms in the imidazolium ring and along the end-to-end vector of the alkyl tail. The heterogeneity in the dynamics of the ILs under study is

detected through the calculation of the non-Gaussian parameter. The non-Gaussian character of the dynamics results in the existence of dynamically distinguishable ions that are found to be highly correlated in space. Extensive study on the structural properties of the ILs revealed a trend for aggregation of the cation's alkyl tail that is more pronounced for the longer chains. The anion is found to be more preferably situated near the imidazolium ring and, more precisely, the anion's nitrogen atoms, which carry the most negative charge, are found closer to the C2 carbon atom of the imidazolium ring, that is, at the most positively area of the cation.

Chapter 5

Permeability Properties of [TF₂N⁻] and [TCM⁻] Imidazolium-Based Ionic Liquids to Gases

ILs are classified among the most attractive candidate sorbents for CO₂ capture and separation from post-combustion flue gases, fulfilling at the same time many of the environmental aspects of the post-combustion CO₂ capture (PCC)¹¹³⁻¹¹⁴. The ultimate goal of the present thesis is the implementation of a molecular simulation methodology for the understanding of the relation between the ionic chemical structure and the material's macroscopic properties, as well as, the prediction of permeability and selectivity properties of technologically relevant ILs based on the accurate molecular modeling of sorbate-sorbent interactions. In the present chapter, the diffusivity and solubility of CO₂, CH₄, Ar, O₂ and N₂ in [C_nmim⁺][TF₂N⁻], $n = 4, 8, 12$ and [C_nmim⁺][TCM⁻], $n = 2, 4, 8$ are studied in a wide temperature range and at atmospheric pressure.

5.1 Force Fields

The formula of the all-atom force field used is given in Eq. (2.1). The bonded and the LJ parameters for the [TF₂N⁻] ILs were obtained directly from the literature^{167,205-206} and the charges calculated quantum-mechanically on ion pairs⁵⁹ were uniformly scaled to give a total ion charge of $\pm 0.75e^-$, as described in Section 3.2. All bonded and the cations' Lennard-Jones parameters for the [TCM⁻] ILs were obtained directly from the literature^{167,205,219,234} and the anion's Lennard-Jones parameters were optimized as shown in Section 4.2. The EPM2 atomistic force field²⁴¹ was used for CO₂ and the TraPPE-UA²⁴² for CH₄. Atomistic force field parameters were obtained from Stan *et al.*²⁴³ for Ar, Rivera *et al.*²⁴⁴ for N₂ and Miyano²⁴⁵ for O₂. All force field parameters are given in Appendix C.

5.2 Simulation Details

Initial configurations were generated by adding the gas molecules in well equilibrated structures of the pure ILs. A 10⁵ steps conjugate gradient energy minimization procedure was applied to eliminate the atomic overlaps and MD simulations of the order of 15 - 30 ns depending on the system, in the isobaric-

isothermal ensemble (NPT) were performed in order to further equilibrate the energy and calculate the density. Subsequently, simulations of the order of 40 – 60 ns were performed in order to calculate the diffusivities of the gas molecules and of the ions' center of mass.

The Lorentz-Berthelot mixing rules were used to calculate the force field parameters between unlike atoms while snapshots were stored every 1 ps during each simulation. A Langevin piston method was used for the temperature control with a 5 ps^{-1} damping factor, while the Nosé-Hoover barostat was used for the pressure control with oscillation period equal to 200 fs and damping factor 100 fs. Electrostatics were handled by means of particle-mesh Ewald method while the reversible reference system propagator algorithm (rRESPA)^{76,204} was used as a multiple time step algorithm with a 1 fs reference time step in order to speed up the MD simulations. Short-range non-bonded van der Waals interactions were calculated every 2 fs, while full electrostatic interactions were computed every 4 fs. A cutoff distance of 12 Å was used to truncate the van der Waals interactions. A long-range correction was applied to the system's energy and virial to account for the neglected van der Waals forces due to switching and cutoff of the LJ potential.

5.3 Results and Discussion

In this Section results on gas diffusivities and solubilities to the ILs under study, are presented. Additionally, selectivity properties of the ILs to the gases of interest are shown.

5.3.1 Gas Diffusivities

At first, long MD simulations were performed at atmospheric pressure in systems of 5 gas molecules in 100 ionic pairs of $[\text{C}_n\text{mim}^+][\text{TF}_2\text{N}^-]$, $n = 4, 8, 12$ at temperatures 298.15, 348.15 and 398.15 K. Long simulations of 10 gas molecules in 100 ion pairs of $[\text{C}_n\text{mim}^+][\text{TCM}^-]$, $n = 2, 4, 8$ were performed at temperatures 298.15, 363.15 and 398.15 K. All the details about the duration and simulation parameters are presented in Section 5.2.

The gas diffusivities in the Fickian regime were calculated using the Einstein relation (see Eq. 2.9). In Tables 5.1 and 5.2 the diffusivities of CO_2 , CH_4 , N_2 and Ar are shown as calculated for the $[\text{TF}_2\text{N}^-]$ and $[\text{TCM}^-]$ ILs respectively. The calculated values are of the order of $10^{-6} \text{ cm}^2/\text{s}$, that is, one order of magnitude higher than the ion

self-diffusivities, in agreement with experimental measurements in ILs²⁴⁶⁻²⁵¹. Densities and self-diffusivities of the ions' center of mass were not affected by addition of the gas molecules in the bulk. The gas molecules are found to have slightly higher diffusivity when diluted in the [TCM] ILs rather than in the [TF₂N] ILs. However, in each IL all gases have comparable diffusivities and for that, the solubility is expected to control the selectivity properties of the ILs, a fact that is also supported by experimentalists²⁵².

Table 5.1 Gas diffusivities in the [C_nmim⁺][TF₂N⁻], $n = 4, 8, 12$ at various temperatures.

Temperature (K)	D (10^{-6} cm ² /s)			
	CO ₂	CH ₄	Ar	N ₂
[C ₄ mim ⁺][Tf ₂ N ⁻]				
298.15	1.3	1.5	2.6	2.0
348.15	5.5	6.7	6.7	5.0
398.15	11.2	11.9	15.4	13.5
[C ₈ mim ⁺][Tf ₂ N ⁻]				
298.15	1.1	1.2	1.7	1.7
348.15	4.4	3.8	5.2	4.8
398.15	10.2	10.5	10.1	13.9
[C ₁₂ mim ⁺][Tf ₂ N ⁻]				
298.15	1.4	1.0	1.7	1.2
348.15	3.6	4.0	5.9	6.8
398.15	12.3	9.6	11.2	11.9

In Figure 5.1 the CO₂ diffusivities as calculated in the [Tf₂N] ILs are plotted against experimental data²⁴⁶⁻²⁵⁰ found in the literature. Additionally, in Figure 5.2 the CO₂ diffusivities calculated in the [TCM] ILs are plotted against recent experimental measurements provided by collaborating experimental groups²⁵³⁻²⁵⁴ in the framework of IOLICAP project¹⁹⁶ (no experimental data on diffusivity or solubility could be found in the literature for [TCM] ILs). The temperature dependence of the gas diffusivity is captured relatively well; however, there is a deviation between the calculated

and the experimental values. Nevertheless, both experimental and predicted gas diffusivities are on the same order of magnitude which is considered satisfactory with MD results underestimating the experimental gas diffusivities, especially at low pressures. Experimental measurement of low pressure gas diffusivity is itself a very challenging task due to the sensitivity of the results to the sample's impurities and the method used. This is reflected to the scattering in the CO₂ experimental diffusivities plotted in Figures 5.1 and 5.2. Estimation of the statistical error in the predicted values requires additional extremely long independent MD runs.

Table 5.2 Gas diffusivities in the [C_nmim⁺][TCM⁻], $n = 2, 4, 8$ at various temperatures.

Temperature (K)	D (10 ⁻⁶ cm/s)			
	CO ₂	CH ₄	Ar	N ₂
[C ₂ mim ⁺][TCM ⁻]				
298.15	2.3	3.0	3.4	2.8
363.15	7.9	9.9	11.4	11.2
398.15	14.4	13.7	16.9	21.6
[C ₄ mim ⁺][TCM ⁻]				
298.15	2.0	2.3	3.0	3.1
363.15	7.4	9.0	10.7	9.7
398.15	11.0	18.0	16.1	15.9
[C ₈ mim ⁺][TCM ⁻]				
298.15	1.6	1.5	2.0	1.8
363.15	8.5	9.1	9.6	9.6
398.15	15.7	14.6	16.8	16.7

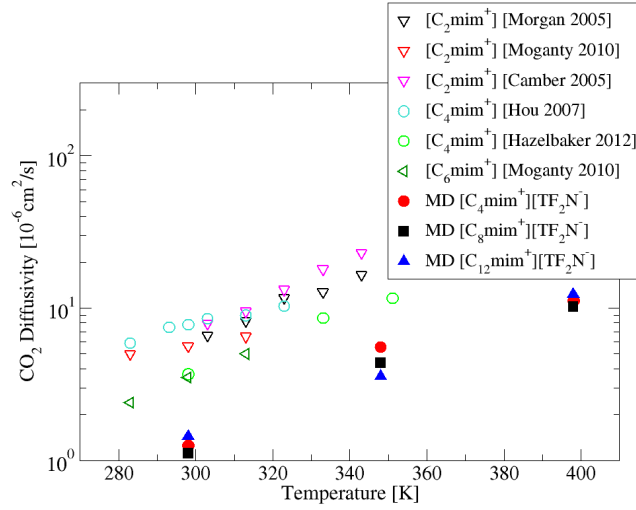


Figure 5.1: MD diffusivity of CO₂ as calculated for the [TF₂N] ILs plotted against experimental data²⁴⁶⁻²⁵⁰.

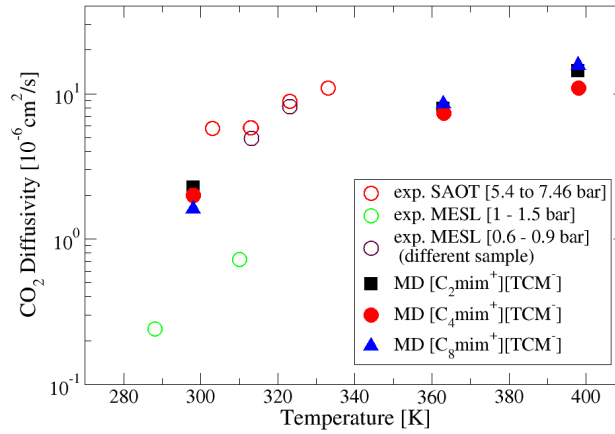


Figure 5.2: MD diffusivity of CO₂ as calculated for the [TCM] ILs plotted against experimental data provided in the framework of IOLICAP project¹⁹⁶.

5.3.2 Gas Solubility - Henry's Law Constant

The solubility of CO₂, N₂, CH₄, Ar and O₂ in both IL families has been calculated using the Widom test-particle insertion methodology²⁵⁵. In the infinite dilution limit, the solubility is the inverse of the Henry's law constant, H , which is defined as:

$$H_i \equiv \lim_{x_i \rightarrow 0} \frac{f_i}{x_i} \quad (5.1)$$

where f_i is the fugacity of component i and x_i is the mole fraction of i in the solvent. The Henry's law constant is related to the excess chemical potential, μ^{ex} , through the following expression²⁵⁶:

$$H_i = \rho RT \exp(\beta \mu_i^{ex}) \quad (5.2)$$

where ρ is the density of the liquid and $\beta = 1/kT$ the inverse temperature. The excess chemical potential can be computed using Widom's test particle insertion method²⁵⁵, in which a test gas molecule is randomly inserted in the fluid and the interaction energy between the test molecule and the material is measured. The excess chemical potential is calculated in the NVT ensemble via the expression:

$$\mu_i^{ex} = -k_B T \ln \int ds_{N+1} \langle \exp(-\beta \Delta U) \rangle_N \quad (5.3)$$

where ΔU is the difference in the potential energy after the insertion of the test gas molecule minus the internal energy of the gas molecule. For each system $2 \times 10^6 - 5 \times 10^6$ total insertions of one gas molecule in random position and orientation, if necessary, were performed. The last part of the trajectories from the production NVT run of the pure IL was used and 10^3 total insertions were performed at each configuration. For CH_4 and Ar, which are modeled as spheres, only random positions were generated and 2×10^6 total insertions were performed in a number of 2×10^3 configurations. For the remaining gases, O_2 , N_2 and CO_2 , both random positions and orientations were generated and 3×10^6 total insertions in 3×10^3 total configurations were performed for O_2 and N_2 . In case of CO_2 , 5×10^6 total insertions in a total number of 5×10^3 configurations, were needed for the convergence of the mean value of the excess chemical potential μ^{ex} and the calculation of the Henry's law constant. An example of such a running average is given in Figure 5.3 where the mean value of μ^{ex} is plotted against the number of total insertions for the case of CO_2 in $[\text{C}_8\text{mim}^+][\text{TCM}^-]$ at 298.15 K.

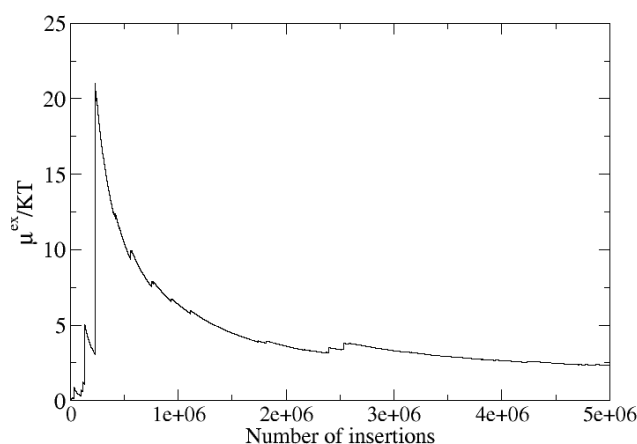


Figure 5.3: The mean value of μ^{ex}/KT as a function of the number of total insertions for the case of CO_2 in $[\text{C}_8\text{mim}^+][\text{TCM}^-]$ at 298.15 K.

In Figure 5.4, the Henry's law constant of the various gases is plotted against temperature for (a) $[\text{C}_4\text{mim}^+][\text{Tf}_2\text{N}^-]$, (b) $[\text{C}_8\text{mim}^+][\text{Tf}_2\text{N}^-]$ and (c) $[\text{C}_{12}\text{mim}^+][\text{Tf}_2\text{N}^-]$. Experimental measurements for CO_2 and CH_4 in $[\text{C}_4\text{mim}^+][\text{Tf}_2\text{N}^-]$ obtained from the literature^{249,257} are also plotted. Results from molecular simulation are in excellent agreement with the experimental data. In Figure 5.5 the calculated values of Henry's law constant is plotted against temperature for (a) $[\text{C}_2\text{mim}^+][\text{TCM}^-]$, (b) $[\text{C}_4\text{mim}^+][\text{TCM}^-]$ and (c) $[\text{C}_8\text{mim}^+][\text{TCM}^-]$. Experimental measurements for CO_2 and N_2 provided by MESL²⁵³ are in excellent agreement with the predicted values. Calculated gas Henry's law constant for the $[\text{TF}_2\text{N}^-]$ and $[\text{TCM}^-]$ ILs are also given in Tables 5.3 and 5.4 respectively together with the error bars calculated using the block averaging method.

The gases CH_4 and Ar are found to be similarly soluble and their solubility is found to increase at higher temperatures in all $[\text{TCM}^-]$ ILs, whereas in the $[\text{Tf}_2\text{N}^-]$ ILs their solubility remains almost unchangeable with temperature, apart from the case of $[\text{C}_{12}\text{mim}^+][\text{Tf}_2\text{N}^-]$ where is found to decrease as the temperature increases. Similarly, the temperature dependence of the solubility of N_2 increases with temperature in the $[\text{TCM}^-]$ ILs and remains almost unchangeable in the $[\text{Tf}_2\text{N}^-]$ ILs.

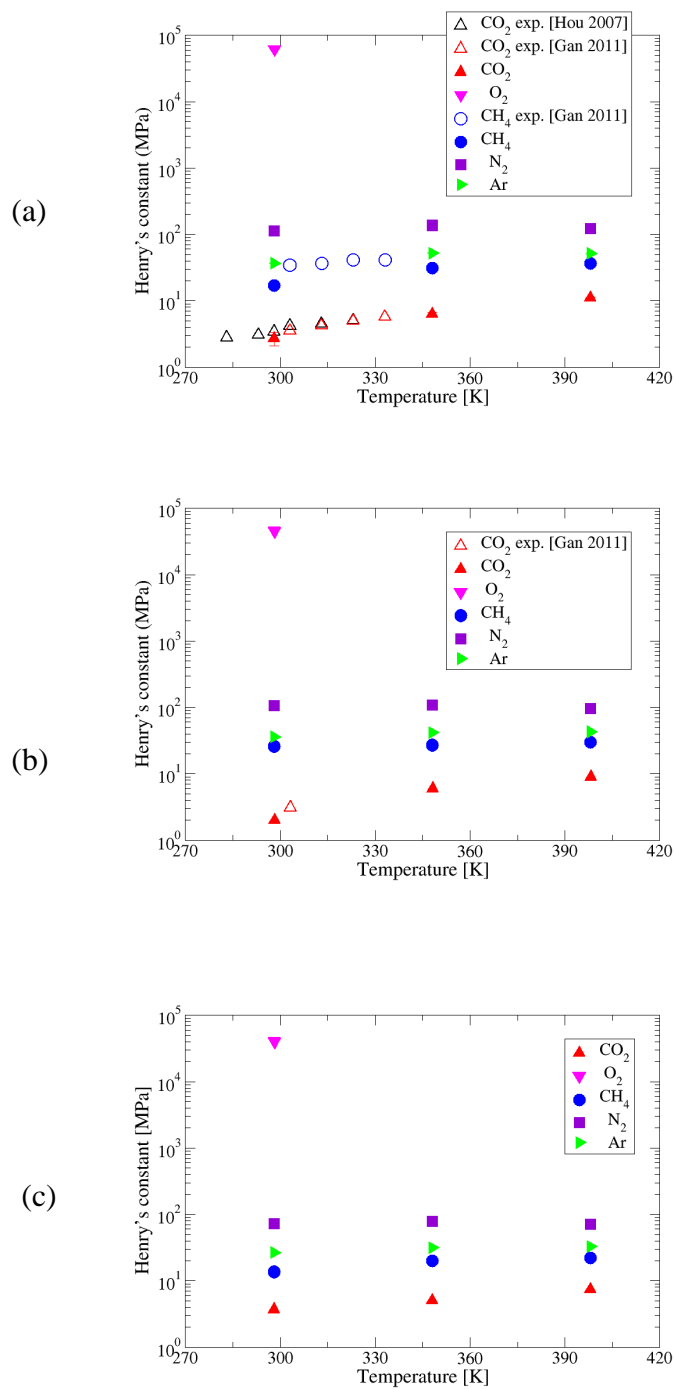


Figure 5.4: Calculation of Henry's Law constants for CO₂, CH₄, Ar, N₂ and O₂ are plotted against temperature for (a) $[C_4mim^+][Tf_2N^-]$, (b) $[C_8mim^+][Tf_2N^-]$ and (c) $[C_{12}mim^+][Tf_2N^-]$.

Experimental measurements for CO₂ and CH₄ in $[C_4mim^+][Tf_2N^-]$ ^{249,257} and for CO₂ in $[C_8mim^+][Tf_2N^-]$ ²⁵⁷ are also shown (open points).

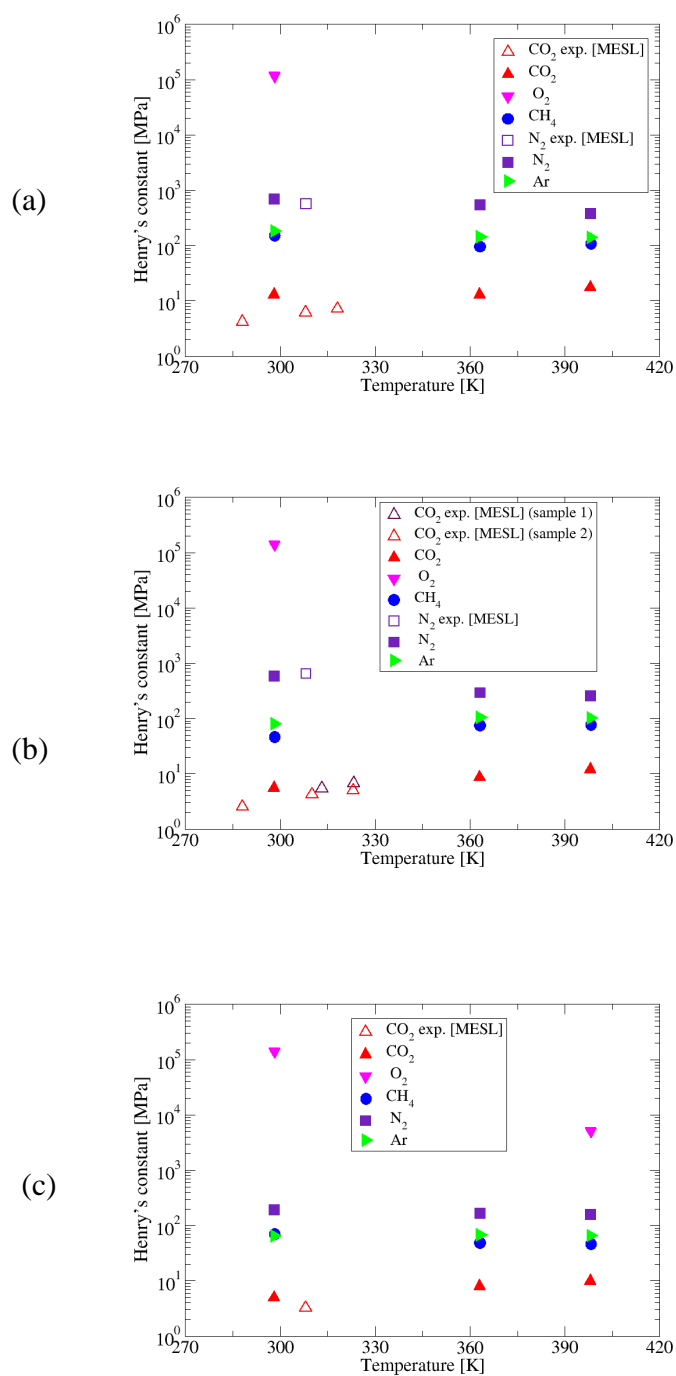


Figure 5.5: Henry's Law constant for CO₂, CH₄, Ar, N₂ and O₂ are plotted against temperature for (a) $[C_2mim^+][TCM^-]$, (b) $[C_4mim^+][TCM^-]$ and (c) $[C_8mim^+][TCM^-]$. Experimental data²⁵³ for CO₂ and N₂ are also plotted for comparison (open points).

Molecular simulation results are in excellent agreement with experimental measurements of the N₂ solubility in the [TCM⁻] ILs provided by MESL²⁵³. Additionally, CO₂ is found to be the most soluble of the gases in both [TCM⁻] and [Tf₂N⁻] ILs with the calculated values being in agreement with all the available experimental measurements^{249,253,257}. It can be concluded from data in Figures 5.4 and 5.5 that at ambient conditions the solubilities of CO₂ and N₂ differ by one and a half orders of magnitude in the [Tf₂N⁻] ILs and by more than two orders of magnitude in the [TCM⁻] ILs.

Solubility calculations for oxygen have been performed at 298.15 K for all ILs in order to get an indication of its solubility at ambient conditions. Two solubility values of O₂ at 398.15 K are shown for [C₈mim⁺][Tf₂N⁻] and [C₈mim⁺][TCM⁻]. It is very interesting to notice that in both ILs the solubility of oxygen increases as the temperature rises unlike the solubility of CO₂ that is found to decrease with the increase of temperature, being in agreement with experimental measurements of O₂ and CO₂ solubility in [C₄mim⁺][BF₄⁻]²⁵⁸.

Table 5.3 Gas Henry's law constant for [C_{*n*}mim⁺][Tf₂N⁻], *n* = 4, 8, 12 at various temperatures. Error bars have been calculated with the block averaging method.

Temperature (K)	<i>H</i> (MPa)			
	CO ₂	CH ₄	Ar	N ₂
[C ₄ mim ⁺][Tf ₂ N ⁻]				
298.15	2.7±0.6	17.3±0.8	36.9±0.4	114±14
348.15	6.3±0.4	32±3	52.4±0.9	137±3
398.15	11.1±0.3	36.7±0.2	51.7±0.9	122±1
[C ₈ mim ⁺][Tf ₂ N ⁻]				
298.15	2.0±0.3	26±6	36±5	106±12
348.15	6±1	27±1	42±1	109±2
398.15	9.0±0.6	30±2	43±1	97±2
[C ₁₂ mim ⁺][Tf ₂ N ⁻]				
298.15	4±2	14±3	27±4	73±4
348.15	5.1±0.6	20.2±0.8	31.5±0.8	78±2
398.15	7.4±0.1	22.3±0.2	33.0±0.5	71±1

Table 5.4 Gas Henry's law constant for $[C_n\text{mim}^+][\text{TCM}^-]$, $n = 2, 4, 8$ at various temperatures.

Error bars have been calculated with the block averaging method.

Temperature (K)	H (MPa)			
	CO_2	CH_4	Ar	N_2
$[\text{C}_2\text{mim}^+][\text{TCM}^-]$				
298.15	13±4	151±1	184±24	690±42
363.15	13±3	98±3	143±2	539±6
398.15	17.6±0.3	108±4	141±3	373±25
$[\text{C}_4\text{mim}^+][\text{TCM}^-]$				
298.15	5.6±0.9	47±12	82±6	582±46
363.15	8.7±0.2	76±8	104.6±0.2	291±10
398.15	12±2	77±3	103.5±0.2	255±6
$[\text{C}_8\text{mim}^+][\text{TCM}^-]$				
298.15	5±3	70±19	68±11	192±35
363.15	8±3	49±1	67.4±0.4	165±8
398.15	10±2	46.0±0.1	66±2	158±7

5.3.3 Permeability and Selectivity Properties of Ionic Liquids

The permeability, P_i , of a material (membrane, zeolite, etc.) to a component i (where i can be either a liquid or a gas) is calculated by the product of the diffusion coefficient of i through the material, D_i , and the solubility of i , S_i :

$$P_i = D_i \times S_i \quad (5.4)$$

Then, for a pair of gases i and j , the selectivity, a_{ij} , is calculated by the expression:

$$a_{ij} = \frac{P_i}{P_j} = \frac{D_i \times S_i}{D_j \times S_j} \quad (5.5)$$

and since solubility, S , and the Henry's law constant, H , are inversely proportional in the infinite dilution limit, the selectivity, a_{ij} , of a material to the components i and j is also given by:

$$a_{ij} = \frac{P_i}{P_j} = \frac{D_i \times H_i^{-1}}{D_j \times H_j^{-1}} \quad (5.6)$$

Equation 5.6 was used for the estimation of the selectivity properties of the ILs to the gases. In Figure 5.6 the selectivities of CO₂ over Ar, CH₄ and N₂ at 298.15 K are shown for (a) the [Tf₂N⁻] ILs and (b) the [TCM⁻] ILs and are plotted as a function of the number of carbon numbers in the cationic alkyl chain.

As shown in Section 5.3.2, there is a great difference in the Henry's law constant of CO₂ and N₂ in both IL families. However, this difference is found to be larger in the [TCM⁻] ILs. Given that the gas diffusivities are similar, as shown in Section 5.3.1, the selectivity of CO₂ over N₂ is expected to be higher in the [TCM⁻] ILs than in the [Tf₂N⁻] ILs. Indeed, as shown in Figure 5.6 the highest selectivity of CO₂/N₂ in the [Tf₂N⁻] ILs is observed for [C₈mim⁺][Tf₂N⁻] and is equal to 31.3, whereas the highest selectivity in the [TCM⁻] ILs is observed for [C₄mim⁺][TCM⁻] and is equal to 67. Experimental selectivities²⁵⁹ of CO₂/N₂ for [C₄mim⁺][Tf₂N⁻] are in excellent agreement with our calculations whereas no experimental measurements of selectivity were found in the literature for the [TCM⁻] ILs. The calculated selectivities of Figure 5.6 are also given in Table 5.5 for the [Tf₂N⁻] ILs and in Table 5.6 for the [TCM⁻] ILs.

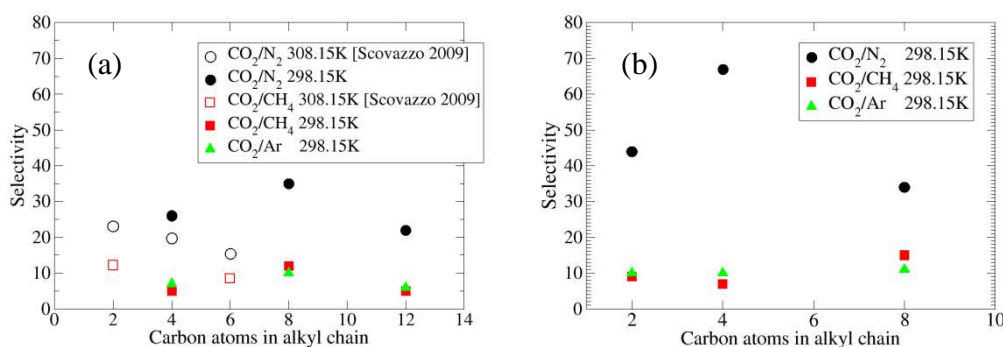


Figure 5.6: Selectivity for the gas pairs CO₂/N₂, CO₂/Ar, CO₂/CH₄ at room temperature and at atmospheric pressure of (a) [C_nmim⁺][Tf₂N⁻], $n = 4, 8, 12$, and (b) [C_nmim⁺][TCM⁻], $n = 2, 4, 8$. Experimental selectivities²⁶⁰ of CO₂/N₂ and CO₂/CH₄ in [C_nmim⁺][Tf₂N⁻] are also plotted.

Table 5.5: Selectivities for $[C_n\text{mim}^+][\text{Tf}_2\text{N}^-]$, $n = 4, 8, 12$ at 298.15 K and atmospheric pressure.

IL	CO_2/N_2	CO_2/CH_4	CO_2/Ar
$[\text{C}_4\text{mim}^+][\text{Tf}_2\text{N}^-]$	26	5	7
$[\text{C}_8\text{mim}^+][\text{Tf}_2\text{N}^-]$	35	12	10
$[\text{C}_{12}\text{mim}^+][\text{Tf}_2\text{N}^-]$	22	5	6

Table 5.6: Selectivities for $[C_n\text{mim}^+][\text{TCM}^-]$, $n = 2, 4, 8$ at 298.15 K and atmospheric pressure.

IL	CO_2/N_2	CO_2/CH_4	CO_2/Ar
$[\text{C}_2\text{mim}^+][\text{TCM}^-]$	44	9	10
$[\text{C}_4\text{mim}^+][\text{TCM}^-]$	67	7	10
$[\text{C}_8\text{mim}^+][\text{TCM}^-]$	34	15	11

5.4 Conclusions

The permeability properties of two imidazolium-based families of ILs, namely $[C_n\text{mim}^+][\text{Tf}_2\text{N}^-]$, $n = 4, 8, 12$, and $[C_n\text{mim}^+][\text{TCM}^-]$, $n = 2, 4, 8$, to the gases CO_2 , N_2 , O_2 , Ar and CH_4 have been studied through the calculation of the gas diffusivities and solubilities at the infinite dilution limit, since permeability is the product of these two properties. For the calculation of the gas diffusivities extremely long MD simulations were performed at various temperatures and at atmospheric pressure. The solubility was calculated in the Henry's regime using the Widom's test particle insertion method in the well equilibrated trajectories of the pure ILs.

Gas diffusivities were found to be of the order of $10^{-6}\text{cm}^2/\text{s}$, one order of magnitude higher than the ions' self-diffusivities, being in reasonable agreement with the experimental data. The gas diffusivities in the $[\text{TCM}^-]$ ILs were found to be slightly higher than the ones in the $[\text{Tf}_2\text{N}^-]$ ILs. The calculated solubilities were at all cases in excellent agreement with the available experimental data. The solubility of O_2 is extremely low and is found to increase with temperature, whereas CO_2 solubility is

found to decrease with temperature, being in agreement with the experimental observations on $[\text{C}_4\text{mim}^+][\text{BF}_4^-]$ ²⁵⁸. The solubility of CO_2 was found to be one and a half orders of magnitude higher than the one of N_2 in the $[\text{Tf}_2\text{N}^-]$ ILs, and more than two orders of magnitude higher in the $[\text{TCM}^-]$ ILs. As a result, both IL families have high CO_2/N_2 selectivities. The CO_2/N_2 selectivity at ambient conditions was in between 21.9 – 31.3 for the $[\text{Tf}_2\text{N}^-]$ ILs, with the highest value observed for $[\text{C}_8\text{mim}^+][\text{Tf}_2\text{N}^-]$. The $[\text{TCM}^-]$ ILs have higher CO_2/N_2 selectivities and are calculated in the range 45.2 – 67, with $[\text{C}_4\text{mim}^+][\text{TCM}^-]$ being the most selective for CO_2/N_2 separation. The extracted selectivities for the two imidazolium-based $[\text{Tf}_2\text{N}^-]$ and $[\text{TCM}^-]$ IL families render the $[\text{TCM}^-]$ ILs very promising candidates for use in CO_2 capture and gas separation technologies.

Chapter 6

Conclusions and Proposed Future Work

The interest for ILs has increased dramatically over the last years, a fact that is reflected to a plethora of computational and experimental studies aiming at the determination of their properties. The present thesis focused on the systematic computational study of imidazolium-based ILs that incorporated two different anions, namely bis-trifluoromethylsulfonfyl ($[\text{Tf}_2\text{N}^-]$) and tricyanomethanide ($[\text{TCM}^-]$). The goal was to study the molecular mechanisms of the systems and to predict macroscopic properties that are relevant to carbon capture technologies and, more precisely, for the capture of CO_2 from a flue gas stream of a coal-fired power plant. A wealth of information has been extracted related to the microscopic behaviour of the materials and on the effect of temperature, the anion structure and the cationic alkyl chain length to the systems' properties.

6.1 Concluding Remarks

Very long MD simulations of the order of several tens of nanoseconds of $[\text{C}_n\text{mim}^+][\text{TF}_2\text{N}^-]$, $n = 4, 8, 12$, and $[\text{C}_n\text{mim}^+][\text{TCM}^-]$, $n = 2, 4, 8$, were performed in a wide temperature range and at atmospheric pressure in order to evaluate thermodynamic, structural, dynamic, permeability and selectivity properties of interest. The complex dynamics of ILs required extremely long MD simulations in order to obtain reliable results of transport properties, especially at room temperature.

Incorporation of polarizability and charge transfer effects is crucial for the accurate prediction of the transport properties. In conjunction to these effects, quantum mechanical calculations performed on ion pairs and on a small cluster of ions indicated a reduced total ionic charge. Scaling the total ionic charge to lower than unity values is an effective alternative to using polarizable force fields that involve complex functional forms and are more computationally demanding. Imidazolium-based tricyanomethanide ($[\text{TCM}^-]$) ILs were studied for the first time using an optimized classical force field. The optimized force field incorporates charges calculated quantum mechanically on isolated ions to attain a transferable set of parameters, with effective incorporation of polarizability and charge transfer effects

by uniformly scaling the atomic charges to lower total values. The validation of the new force field revealed its accuracy towards the calculation of both density and transport properties.

The density of the $[\text{TF}_2\text{N}^-]$ ILs was found to be higher than of the one of the $[\text{TCM}^-]$ ILs. The spatial organization of ILs was analyzed through radial and radial-angular correlation functions. At all cases, the microscopic structure of these systems was retained at much longer distances compared to ordinary molecular liquids. Non-polar cationic alkyl tails exhibited a tendency for aggregation, a phenomenon which becomes more pronounced for the longer alkyl chain lengths. At the same time, the anions were found to be highly spatially correlated with the cation's imidazolium ring where the positive charge is located. The $[\text{TCM}^-]$ was found to be more uniformly distributed around the imidazolium ring whereas the $[\text{TF}_2\text{N}^-]$ was preferably located above and below the mean plane of the imidazolium ring.

The complex dynamic behaviour of ILs has been studied through the prediction of transport properties, such as ionic self-diffusivities, the calculation of relaxation times of different parts of the ions and the analysis of the ionic translational motion at different time scales and along various directions. The extremely sluggish dynamics of these materials resembles the ones of polymers, with a wide range of relaxation times characterizing their segmental dynamics, especially at ambient temperature where very long simulations were necessary in order to obtain reliable calculations of the transport properties. The $[\text{Tf}_2\text{N}^-]$ ILs were found to have a higher viscosity than the $[\text{TCM}^-]$ ILs with the ions' diffusivity been lower in the $[\text{Tf}_2\text{N}^-]$ ILs than the one in the $[\text{TCM}^-]$ ILs. The ionic translation motion was found to be highly anisotropic: there was a preferential movement along the direction of the alkyl tail for the cation and along the direction of the vector that connects the two sulfurs for the $[\text{Tf}_2\text{N}^-]$ anion. The strong heterogeneous dynamics of ILs was characterized by deviations from a Gaussian behaviour of the distribution probability of the mean square displacement. These dynamic heterogeneity phenomena were more pronounced in the case of cations with longer alkyl chains and are preserved for several nanoseconds at room temperatures. Dynamically distinguishable ions were found to be strongly correlated in space forming clusters of ions of the same mobility.

The permeability properties of the ILs to CO₂, N₂, Ar, CH₄ and O₂ were studied through the calculation of the gas diffusivities and solubilities in order to identify which of the two IL families is most suitable for the capture of CO₂. The gas diffusivities were found to be of the order of 10⁻⁶cm²/s, one order of magnitude higher than the ionic ones, being in good agreement with experimental measurements. All gases had comparable diffusivities, with the ones calculated in the [TCM⁻] ILs being slightly higher than in the [Tf₂N⁻] ILs. This fact indicates that solubility is the key factor that determines the gas selectivity in ILs. Solubility calculations were performed in the Henry regime using the Widom particle insertion method. The solubility of O₂ is extremely low and was found to increase with temperature, while the inverse was observed for CO₂ solubility. The solubility of CO₂ was found to be one and a half orders of magnitude higher than the one of N₂ in the [Tf₂N⁻] ILs and two orders of magnitude higher in the [TCM⁻] ILs. In imidazolium-based [Tf₂N⁻] ILs the selectivity of CO₂/N₂ ranges from 21.9 – 31.3 while the [TCM⁻] ILs exhibit much higher CO₂/N₂ selectivity with [C₄mim⁺][TCM⁻] performing best (CO₂/N₂ selectivity = 67). Consequently, imidazolium-based [TCM⁻] ILs are recognized as very promising candidates for use in CO₂ separation technologies.

6.2 Proposed Future Work

The diversity of ILs necessitates the unfolding of the link between chemical structure and macroscopic behaviour, as well as, the development of screening strategies for the choice of an appropriate IL for a given application. Within this scope, the present thesis may be the basis for future work in various directions.

The anion [TCM⁻] has been rarely used in computational studies of ILs. However, it seems to be a very good candidate for use in ILs for lower densities, viscosities and good permeability properties. The [TCM⁻] force field proposed in the present thesis could definitely be used for the study of [TCM⁻] based ILs incorporating different families of cations.

Further investigation of the permeability properties of the [Tf₂N⁻] and [TCM⁻] ILs to different gases of various-sized molecules would be of great interest for their potential use in other separation processes. Additionally, study of the permeability properties of ILs confined in zeolite frameworks or carbon nanotubes would give

insight into the performance of supported ionic liquid membranes (SILM) for separation processes.

Another promising field of research is the study of the properties of mixtures of two or more ILs or ILs with water or other solvents in order to examine the effect of the composition on the various properties of interest. Additionally, the present work could also be extended to the calculation of several other properties, such as ionic conductivity. This would be of a high technological interest for the potential use of these ILs to dye-sensitized solar cells. Moreover, different methods could also be used for the simulation of these ILs. For example, the use of non-equilibrium MD simulations for the calculation of viscosity would be very valuable towards the estimation of the most appropriate method to safely calculate viscosity for systems with so complex dynamics.

As far as CO₂ capture technologies are concerned, it is of great importance to study more IL families, either incorporating a different cation, an anion that can react with CO₂ or even poly-ILs. For that, it would be necessary to develop multi-scale modelling methods, such as, the use of hybrid quantum mechanical and classical simulations or the implementation of coarse grained models that would accelerate the simulations enabling the computational study of ILs with more complex chemical structure.

Appendix A: Force Field Parameters for the [Tf₂N⁻] Ionic Liquids

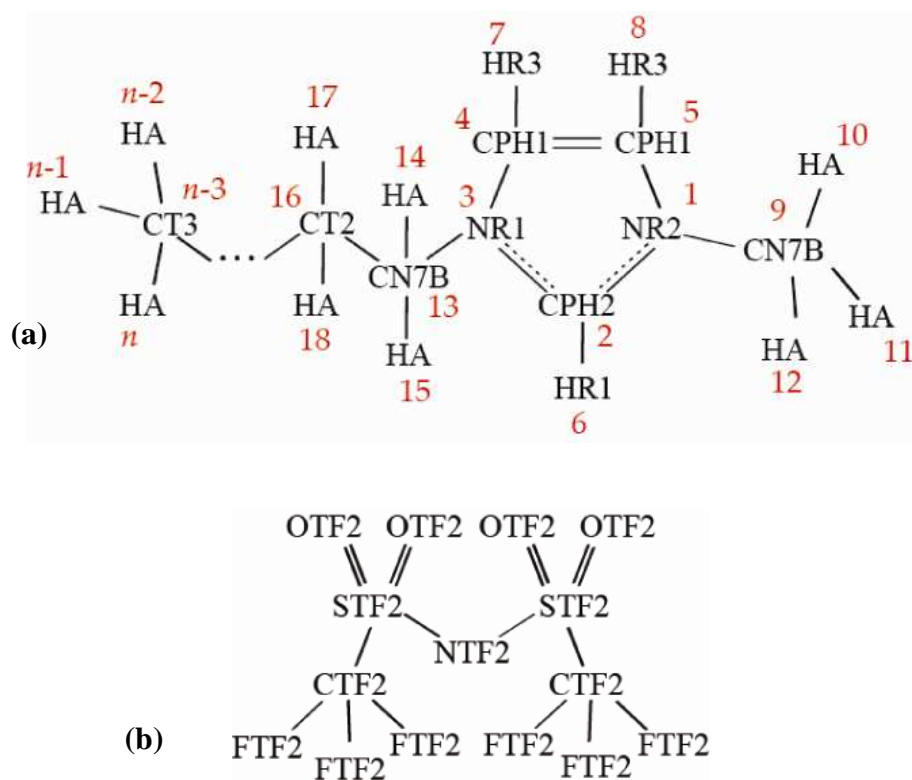


Figure A1: Atomic labeling for (a) [C_nmim⁺], $n > 2$ and (b) [Tf₂N⁻].

Table A1: Bond force constants (k_b) and equilibrium bond distances (b_0).[C₄mim⁺], [C₈mim⁺], [C₁₂mim⁺] [All parameters from Ref. 167]

Atom 1	Atom 2	K_b (kcal mol ⁻¹ Å ⁻²)	b_0 (Å)
CN7B	NR1	220.00	1.4762
CN7B	NR2	220.00	1.4762
CPH1	NR1	400.00	1.3819
CPH1	NR2	400.00	1.3819
CPH2	NR1	400.00	1.3366
CPH2	NR2	400.00	1.3366
CPH1	CPH1	410.00	1.3610
CPH2	HR1	340.00	1.0779
CPH1	HR3	365.00	1.0775
CN7B	HA	309.00	1.0889
CT2	HA	309.00	1.0954
CT3	HA	322.00	1.0935
CN7B	CT2	200.00	1.5308
CT2	CT2	222.50	1.5373
CT2	CT3	222.50	1.5314

[Tf₂N⁻] [All parameters from Ref. 206]

Atom 1	Atom 2	K_b (kcal mol ⁻¹ Å ⁻²)	b_0 (Å)
CTF2	FTF2	441.80	1.3230
CTF2	STF2	235.42	1.8180
STF2	OTF2	637.07	1.4420
NTF2	STF2	372.01	1.5700

Table A2: Bond angle bending parameters (k_θ) and equilibrium angles (θ_0).[C₄mim⁺], [C₈mim⁺], [C₁₂mim⁺] [All parameters from Ref. 167]

Atom 1	Atom 2	Atom 3	K_θ (kcal mol ⁻¹ rad ⁻²)	θ_0 (deg)
CT2	CN7B	NR1	140.00	112.34
CPH1	NR1	CPH2	130.00	108.25
CPH1	NR2	CPH2	130.00	108.25
HA	CN7B	NR1	30.00	109.41
HA	CN7B	NR2	30.00	109.41
HR1	CPH2	NR1	25.00	125.44
HR1	CPH2	NR2	25.00	125.44
NR1	CPH1	CPH1	130.00	107.28
NR2	CPH1	CPH1	130.00	107.28
NR1	CPH2	NR2	130.00	109.11
HR3	CPH1	CPH1	25.00	130.74
NR2	CPH1	HR3	25.00	122.04
NR1	CPH1	HR3	25.00	122.04
HA	CN7B	HA	35.50	108.44
HA	CN7B	CT2	33.40	111.68
HA	CT2	CN7B	33.40	109.13
CN7B	CT2	CT2	58.35	111.50
CT2	CT2	CT3	58.00	112.34
CT2	CT2	CT2	58.00	112.34
HA	CT2	HA	35.50	106.13
HA	CT3	HA	35.50	107.24
CT2	CT2	HA	26.50	108.43
CT2	CT3	HA	34.60	111.62
CT3	CT2	HA	34.60	109.47
CN7B	NR2	CPH2	130.00	125.75
CN7B	NR1	CPH2	130.00	125.75

CN7B	NR2	CPH1	130.00	125.67
CN7B	NR1	CPH1	130.00	125.67

[Tf₂N⁻] [All parameters from Ref. 206]

Atom 1	Atom 2	Atom 3	K _θ (kcal mol ⁻¹ rad ⁻²)	θ _o (deg)
FTF2	CTF2	FTF2	93.33	107.10
STF2	CTF2	FTF2	82.93	111.80
CTF2	STF2	OTF2	103.97	102.60
OTF2	STF2	OTF2	115.80	118.50
OTF2	STF2	NTF2	94.51	113.60
CTF2	STF2	NTF2	97.51	100.20
STF2	NTF2	STF2	80.19	125.60

Table A3: Dihedral angle parameters.[C₄mim⁺], [C₈mim⁺], [C₁₂mim⁺] [All parameters from Refs. 167,205]

Atom 1	Atom 2	Atom 3	Atom 4	K _z (kcal mol ⁻¹)	n	δ (deg)
CPH2	NR1	CPH1	CPH1	14	2	180
CPH2	NR2	CPH1	CPH1	14	2	180
NR1	CPH1	CPH1	NR2	14	2	180
NR1	CPH2	NR2	CPH1	14	2	180
NR2	CPH2	NR1	CPH1	14	2	180
HR1	CPH2	NR1	CPH1	3	2	180
HR1	CPH2	NR2	CPH1	3	2	180
HR3	CPH1	CPH1	HR3	2	2	180
CPH1	CPH1	NR1	CN7B	0	1	0
CPH1	CPH1	NR2	CN7B	0	1	0
HR3	CPH1	NR2	CPH2	3	2	180
HR3	CPH1	NR1	CPH2	3	2	180
NR1	CPH1	CPH1	HR3	3	2	180
NR2	CPH1	CPH1	HR3	3	2	180
NR1	CPH2	NR2	CN7B	0	2	180
NR2	CPH2	NR1	CN7B	0	2	180
HR1	CPH2	NR1	CN7B	0	2	180
HR1	CPH2	NR2	CN7B	0	2	180
HR3	CPH1	NR1	CN7B	0	2	180
HR3	CPH1	NR2	CN7B	0	2	180
CPH2	NR1	CN7B	HA	0.195	2	180
CPH2	NR2	CN7B	HA	0.195	2	180
CPH1	NR2	CN7B	HA	0	3	0
CPH1	NR1	CN7B	HA	0	3	0
CPH2	NR1	CN7B	CT2	0.1	3	180
CPH1	NR1	CN7B	CT2	0.2	4	0

NR1	CN7B	CT2	CT2	0	3	0
HA	CT2	CT3	HA	0.16	3	0
CT2	CT2	CT3	HA	0.16	3	0
NR1	CN7B	CT2	HA	0	3	0
CN7B	CT2	CT2	CT3	0.15	1	0
HA	CN7B	CT2	HA	0.195	3	0
CT2	CT2	CN7B	HA	0.195	3	0
HA	CT2	CT2	CN7B	0.195	3	0
HA	CT2	CT2	HA	0.195	3	0
HA	CT2	CT2	CT3	0.195	3	0
CN7B	CT2	CT2	CT2	0.15	1	0
HA	CT2	CT2	CT2	0.19	3	0
CT2	CT2	CT2	CT2	0.15	1	0
CT2	CT2	CT2	CT3	0.15	1	0

[Tf₂N⁻] [All parameters from Ref. 206]

Atom 1	Atom 2	Atom 3	Atom 4	k _z (kcal mol ⁻¹)	n	δ (deg)
FTF2	CTF2	STF2	OTF2	0.1734	3	0
STF2	NTF2	STF2	OTF2	-0.0018	3	0
FTF2	CTF2	STF2	NTF2	0.1580	3	0
STF2	NTF2	STF2	CTF2	7.8329	1	0
				-2.4904	2	180
				-0.7636	3	0

Table A4: Improper dihedral angle parameters.[C₄mim⁺], [C₈mim⁺], [C₁₂mim⁺] [All parameters from Ref. 167]

Atom 1	Atom 2	Atom 3	Atom 4	k _ψ (kcal mol ⁻¹ rad ⁻²)	ψ (deg)
CPH2	NR1	NR2	HR1	0.5	0
NR1	CPH1	CPH2	CN7B	0.6	0
NR2	CPH1	CPH2	CN7B	0.6	0
CPH1	CPH1	NR2	HR3	0.5	0
CPH1	CPH1	NR1	HR3	0.5	0

Table A5: Lennard-Jones parameters. Note that $\sigma = R_{\min} / \sqrt[6]{2}$

[All parameters from Refs. 167,205]

Atom	ε (kcal mol ⁻¹)	R _{min} /2(Å)
CPH1	0.050	1.800
NR1	0.200	1.850
CPH2	0.050	1.800
NR2	0.200	1.850
HR3	0.0078	1.468
HR1	0.046	0.900
CN7B	0.020	2.275
HA	0.022	1.320
CT3	0.080	2.060
CT2	0.055	2.175
NTF2	0.170	1.824
STF2	0.250	1.992
OTF2	0.210	1.661
FTF2	0.053	1.656
CTF2	0.066	1.964

Table A6: Partial Atomic Charges (e) from six minimum energy conformations of the ionic pairs.

Atom type	[C ₄ mim ⁺]	Atom type	[C ₈ mim ⁺]	Atom type	[C ₁₂ mim ⁺]	Numbering
NR1	0.146046	NR1	0.155009	NR1	0.149592	1
CPH1	-0.006432	CPH1	0.011546	CPH1	0.005189	2
NR2	0.092254	NR2	0.027923	NR2	0.050562	3
CPH2	-0.193107	CPH2	-0.169840	CPH2	-0.175725	4
CPH2	-0.152475	CPH2	-0.160453	CPH2	-0.158008	5
HR1	0.208287	HR1	0.197022	HR1	0.207767	6
HR2	0.205544	HR2	0.198474	HR2	0.199575	7
HR2	0.184183	HR2	0.184331	HR2	0.182227	8
CN7B	-0.171877	CN7B	-0.186531	CN7B	-0.182722	9
HA	0.119267	HA	0.123623	HA	0.121004	10
HA	0.148216	HA	0.152725	HA	0.153862	11
HA	0.087322	HA	0.089925	HA	0.089753	12
CN7B	0.005903	CN7B	0.155001	CN7B	0.095302	13
HA	0.054165	HA	0.022300	HA	0.034711	14
HA	0.045561	HA	0.003636	HA	0.020004	15
CT2	0.076942	CT2	0.060322	CT2	0.098184	16
HA	-0.029155	HA	-0.032668	HA	-0.043171	17
HA	0.000652	HA	-0.003523	HA	-0.007750	18
CT2	0.227458	CT2	0.062203	CT2	0.075731	19
HA	-0.024423	HA	-0.000414	HA	-0.007673	20
HA	-0.051806	HA	-0.027449	HA	-0.031506	21
CT3	-0.261600	CT2	0.060301	CT2	0.002472	22
HA	0.061505	HA	-0.014134	HA	-0.004679	23
HA	0.051733	HA	-0.022204	HA	-0.013223	24
HA	0.136136	CT2	-0.012540	CT2	0.076959	25
		HA	-0.012890	HA	-0.028846	26
		HA	-0.007224	HA	-0.023033	27

	CT2	0.031916	CT2	0.037414	28
	HA	-0.020670	HA	-0.026376	29
	HA	-0.012408	HA	-0.017055	30
	CT2	0.263208	CT2	0.119874	31
	HA	-0.068022	HA	-0.046106	32
	HA	-0.073391	HA	-0.049613	33
	CT3	-0.203852	CT2	0.105810	34
	HA	0.228740	HA	0.141455	35
	HA	-0.057544	HA	-0.137253	36
	HA	-0.072053	CT2	-0.016077	37
			HA	-0.014312	38
			HA	-0.016138	39
			CT2	0.029556	40
			HA	-0.019406	41
			HA	-0.018442	42
			CT2	0.231526	43
			HA	-0.053892	44
			HA	-0.053922	45
			CT3	-0.219089	46
			HA	0.039365	47
			HA	0.044249	48
			HA	0.038943	49

Partial charges for [Tf ₂ N ⁻] (<i>e</i>)					
[C ₄ mim ⁺][Tf ₂ N ⁻]		[C ₈ mim ⁺][Tf ₂ N ⁻]		[C ₁₂ mim ⁺][Tf ₂ N ⁻]	
CTF2	0.348789	CTF2	0.286260	CTF2	0.286641
FTF2	-0.131010	FTF2	-0.140461	FTF2	-0.139892
STF2	0.858581	STF2	1.005400	STF2	0.891159
OTF2	-0.534882	OTF2	-0.484953	OTF2	-0.457205
NTF2	-0.449452	NTF2	-0.671137	NTF2	-0.674497

Table A7: Partial Atomic Charges (e^-) from six minimum energy conformations of the ionic pair uniformly scaled to $\pm 0.75e^-$ total ionic charge.

Atom type [C ₄ mim ⁺]	Atom type [C ₈ mim ⁺]	Atom type [C ₁₂ mim ⁺]	numbering
NR2 0.114066	NR2 0.133613	NR2 0.113661	1
CPH2 -0.005023	CPH2 0.009953	CPH2 0.003943	2
NR1 0.072051	NR1 0.024070	NR1 0.038418	3
CPH1 -0.150818	CPH1 -0.146402	CPH1 -0.133520	4
CPH1 -0.119084	CPH1 -0.138310	CPH1 -0.120058	5
HR1 0.162674	HR1 0.169833	HR1 0.157867	6
HR3 0.160531	HR3 0.171085	HR3 0.151642	7
HR3 0.143848	HR3 0.158893	HR3 0.138461	8
CN7B -0.134237	CN7B -0.160790	CN7B -0.138837	9
HA 0.093148	HA 0.106563	HA 0.091942	10
HA 0.115758	HA 0.131649	HA 0.116908	11
HA 0.068199	HA 0.077515	HA 0.068197	12
CN7B 0.004610	CN7B 0.133611	CN7B 0.072413	13
HA 0.042303	HA 0.019223	HA 0.026374	14
HA 0.035583	HA 0.003134	HA 0.015200	15
CT2 0.060092	CT2 0.051998	CT2 0.074603	16
HA -0.022770	HA -0.028160	HA -0.032802	17
HA 0.000509	HA -0.003037	HA -0.005889	18
CT2 0.177646	CT2 0.053619	CT2 0.057542	19
HA -0.019075	HA -0.000357	HA -0.005830	20
HA -0.040461	HA -0.023661	HA -0.023939	21
CT3 -0.204311	CT2 0.051979	CT2 0.001878	22
HA 0.048036	HA -0.012184	HA -0.003555	23
HA 0.040404	HA -0.019140	HA -0.010047	24
HA 0.106323	CT2 -0.010809	CT2 0.058475	25
	HA -0.011111	HA -0.021918	26
	HA -0.006227	HA -0.017501	27

	CT2 0.027512	CT2 0.028428	28
	HA -0.017818	HA -0.020041	29
	HA -0.010696	HA -0.012959	30
	CT2 0.226885	CT2 0.091083	31
	HA -0.058635	HA -0.035033	32
	HA -0.063263	HA -0.037697	33
	CT3 -0.175720	CT2 0.080397	34
	HA 0.197174	HA 0.107481	35
	HA -0.049603	HA -0.104288	36
	HA -0.062110	CT2 -0.012216	37
		HA -0.010875	38
		HA -0.012262	39
		CT2 0.022457	40
		HA -0.014745	41
		HA -0.014013	42
		CT2 0.175919	43
		HA -0.040949	44
		HA -0.040971	45
		CT3 -0.166469	46
		HA 0.029911	47
		HA 0.033622	48
		HA 0.029590	49

Partial charges for [Tf ₂ N ⁻] (e ⁻)			
[C ₄ mim ⁺][Tf ₂ N ⁻]		[C ₈ mim ⁺][Tf ₂ N ⁻]	
CTF2	0.272407	CTF2	0.246756
FTF2	-0.102320	FTF2	-0.121077
STF2	0.670558	STF2	0.866655
OTF2	-0.417747	OTF2	-0.418029
NTF2	-0.351024	NTF2	-0.578520

CTF2	0.217797
FTF2	-0.106293
STF2	0.677125
OTF2	-0.347396
NTF2	-0.512500

Table A8: Mass density calculations for the three ILs at different temperatures and 1 bar using charges scaled to $\pm 0.75e^-$ total ionic charge. In all cases, the statistical uncertainty is less than 0.001.

T (K)	Mass Density (gr/cm ³)		
	[C ₄ mim ⁺][Tf ₂ N ⁻]	[C ₈ mim ⁺][Tf ₂ N ⁻]	[C ₁₂ mim ⁺][Tf ₂ N ⁻]
298.15	1.4357	1.322	1.236
348.15	1.3791	1.270	1.1886
398.15	1.3213	1.220	1.140

Table A9: Anions' and cations' self-diffusion coefficients of the center of mass for the three ILs at different temperatures and 1 bar using charges scaled to $\pm 0.75e^-$ total ionic charge.

T (K)	Self Diffusion Coefficients (10 ⁻⁷ cm ² /s)					
	[C ₄ mim ⁺][Tf ₂ N ⁻]		[C ₈ mim ⁺][Tf ₂ N ⁻]		[C ₁₂ mim ⁺][Tf ₂ N ⁻]	
	Anion	Cation	Anion	Cation	Anion	Cation
298.15	1.0	1.9	0.6	0.5	0.4	0.4
348.15	3.8	6.9	3.3	3.2	2.5	2.2
398.15	10.2	16.2	8.6	7.6	7.5	7.0

Table A10: Viscosity calculations for the three ILs at different temperatures and 1 bar using charges scaled to $\pm 0.75e^-$ total ionic charge.

T (K)	Viscosity (Pa*s)		
	[C ₄ mim ⁺][Tf ₂ N ⁻]	[C ₈ mim ⁺][Tf ₂ N ⁻]	[C ₁₂ mim ⁺][Tf ₂ N ⁻]
298.15	0.075	0.12	0.17
348.15	0.025	0.04	0.035
398.15	0.007	0.007	0.008

Appendix B: Force Field Parameters for the [TCM⁻] Ionic Liquids

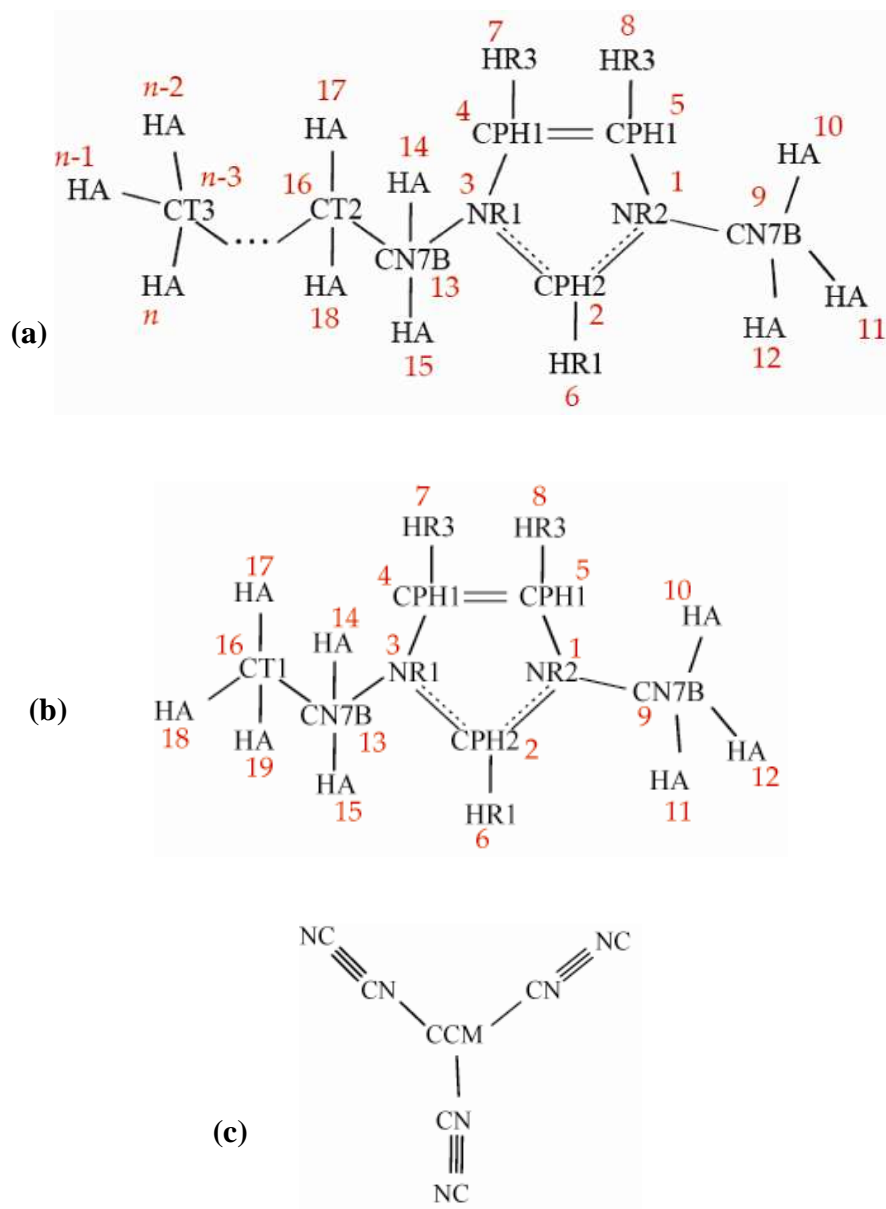


Figure B1: Atomic labeling for (a) [C_nmim⁺], $n > 2$ and (b) [C₂mim⁺] and (c) [TCM⁻].

Table B1: Charges for [TCM⁻] anion calculated as isolated ion and averaged over multiple ion pair conformations.

Atom	Charge for isolated ion	Average charge	Standard deviation
CCM	-0.5110	-0.4903	0.0095
CN	0.5653	0.4690	0.0100
CN	0.5668	0.4872	0.0046
CN	0.5654	0.4845	0.0166
NC	-0.7292	-0.5625	0.0176
NC	-0.7288	-0.5507	0.0129
NC	-0.7286	-0.5727	0.0110
Total	-1.0000	-0.7355	

Table B2: Charges for [C₄mim⁺] cation calculated as isolated ion and averaged over multiple ion pair conformations

Atom	Charge for isolated ion	Average charge	Standard deviation
NR2	0.1110	0.1664	0.0320
CPH2	0.0054	-0.0849	0.0383
NR1	0.1124	0.1632	0.0557
CPH1	0.0025	0.0032	0.0575
CPH1	0.0353	0.0069	0.0382
HR1	0.1030	0.1326	0.0110
HR3	0.0808	0.0424	0.0402
HR3	0.0604	0.0348	0.0205
CN7B	0.4505	0.4601	0.0368
HA	-0.0896	-0.1643	0.0414

HA	-0.0686	-0.1301	0.0734
HA	-0.0781	-0.0270	0.0035
CN7B	0.3270	0.2498	0.1307
HA	-0.0656	0.0170	0.0364
HA	-0.0448	-0.0796	0.0957
CT2	0.0903	0.1861	0.0721
HA	-0.0382	-0.0802	0.0504
HA	-0.0667	-0.1106	0.0251
CT2	0.2489	0.2262	0.1532
HA	-0.0933	-0.0988	0.0758
HA	-0.0927	-0.1239	0.0482
CT3	0.3018	0.4702	0.1075
HA	-0.0973	-0.1566	0.0368
HA	-0.0947	-0.1748	0.0317
HA	-0.0997	-0.1925	0.0198
Total	1.0000	0.7355	

Table B3: Bond force constants (k_b) and equilibrium bond distances (b_0).[C₂mim⁺], [C₄mim⁺], [C₈mim⁺] [All parameters from Refs. 167,219]

Atom 1	Atom 2	K_b (kcal mol ⁻¹ Å ⁻²)	b_0 (Å)
CN7B	NR1	220.00	1.4762
CN7B	NR2	220.00	1.4762
CPH1	NR1	400.00	1.3819
CPH1	NR2	400.00	1.3819
CPH2	NR1	400.00	1.3366
CPH2	NR2	400.00	1.3366
CPH1	CPH1	410.00	1.3610
CPH2	HR1	340.00	1.0779
CPH1	HR3	365.00	1.0775
CN7B	HA	309.00	1.0889
CT2	HA	309.00	1.0954
CT3	HA	322.00	1.0935
CN7B	CT2	200.00	1.5308
CT2	CT2	222.50	1.5373
CT2	CT3	222.50	1.5314
CT1	CN7B	309.78	1.526
CT1	HA	339.88	1.090

[TCM] [All parameters from Ref. 234]

Atom 1	Atom 2	K_b (kcal mol ⁻¹ Å ⁻²)	b_0 (Å)
CCM	CN	430.00	1.408
CN	NC	1210.0	1.167

Table B4: Bond angle bending parameters (k_θ) and equilibrium angles (θ_0).[C₂mim⁺], [C₄mim⁺], [C₈mim⁺] [All parameters from Refs. 167,219]

Atom 1	Atom 2	Atom 3	K_θ (kcal mol ⁻¹ rad ⁻²)	θ_0 (deg)
CT2	CN7B	NR1	140.00	112.34
CPH1	NR1	CPH2	130.00	108.25
CPH1	NR2	CPH2	130.00	108.25
HA	CN7B	NR1	30.00	109.41
HA	CN7B	NR2	30.00	109.41
HR1	CPH2	NR1	25.00	125.44
HR1	CPH2	NR2	25.00	125.44
NR1	CPH1	CPH1	130.00	107.28
NR2	CPH1	CPH1	130.00	107.28
NR1	CPH2	NR2	130.00	109.11
HR3	CPH1	CPH1	25.00	130.74
NR2	CPH1	HR3	25.00	122.04
NR1	CPH1	HR3	25.00	122.04
HA	CN7B	HA	35.50	108.44
HA	CN7B	CT2	33.40	111.68
HA	CT2	CN7B	33.40	109.13
CN7B	CT2	CT2	58.35	111.50
CT2	CT2	CT3	58.00	112.34
CT2	CT2	CT2	58.00	112.34
HA	CT2	HA	35.50	106.13
HA	CT3	HA	35.50	107.24
CT2	CT2	HA	26.50	108.43
CT2	CT3	HA	34.60	111.62
CT3	CT2	HA	34.60	109.47
CN7B	NR2	CPH2	130.00	125.75

CN7B	NR1	CPH2	130.00	125.75
CN7B	NR2	CPH1	130.00	125.67
CN7B	NR1	CPH1	130.00	125.67
HA	CT1	HA	33.94	109.5
HA	CT1	CN7B	38.00	109.5
HA	CN7B	CT1	38.00	109.5
NR1	CN7B	CT1	70.03	112.2

[TCM] [All parameters from Ref. 234]

Atom 1	Atom 2	Atom 3	K_{θ} (kcal mol ⁻¹ rad ⁻²)	θ_0 (deg)
NC	CN	CCM	30.0	179.99
CN	CCM	CN	44.0	120.00

Table B5: Dihedral angle parameters.[C₂mim⁺], [C₄mim⁺], [C₈mim⁺] [All parameters from Refs. 167,205,219]

Atom 1	Atom 2	Atom 3	Atom 4	K _χ (kcal mol ⁻¹)	n	δ (deg)
CPH2	NR1	CPH1	CPH1	14	2	180
CPH2	NR2	CPH1	CPH1	14	2	180
NR1	CPH1	CPH1	NR2	14	2	180
NR1	CPH2	NR2	CPH1	14	2	180
NR2	CPH2	NR1	CPH1	14	2	180
HR1	CPH2	NR1	CPH1	3	2	180
HR1	CPH2	NR2	CPH1	3	2	180
HR3	CPH1	CPH1	HR3	2	2	180
CPH1	CPH1	NR1	CN7B	0	1	0
CPH1	CPH1	NR2	CN7B	0	1	0
HR3	CPH1	NR2	CPH2	3	2	180
HR3	CPH1	NR1	CPH2	3	2	180
NR1	CPH1	CPH1	HR3	3	2	180
NR2	CPH1	CPH1	HR3	3	2	180
NR1	CPH2	NR2	CN7B	0	2	180
NR2	CPH2	NR1	CN7B	0	2	180
HR1	CPH2	NR1	CN7B	0	2	180
HR1	CPH2	NR2	CN7B	0	2	180
HR3	CPH1	NR1	CN7B	0	2	180
HR3	CPH1	NR2	CN7B	0	2	180
CPH2	NR1	CN7B	HA	0.195	2	180
CPH2	NR2	CN7B	HA	0.195	2	180
CPH1	NR2	CN7B	HA	0	3	0
CPH1	NR1	CN7B	HA	0	3	0
CPH2	NR1	CN7B	CT2	0.1	3	180
CPH1	NR1	CN7B	CT2	0.2	4	0

NR1	CN7B	CT2	CT2	0	3	0
HA	CT2	CT3	HA	0.16	3	0
CT2	CT2	CT3	HA	0.16	3	0
NR1	CN7B	CT2	HA	0	3	0
CN7B	CT2	CT2	CT3	0.15	1	0
HA	CN7B	CT2	HA	0.195	3	0
CT2	CT2	CN7B	HA	0.195	3	0
HA	CT2	CT2	CN7B	0.195	3	0
HA	CT2	CT2	HA	0.195	3	0
HA	CT2	CT2	CT3	0.195	3	0
CN7B	CT2	CT2	CT2	0.15	1	0
HA	CT2	CT2	CT2	0.19	3	0
CT2	CT2	CT2	CT2	0.15	1	0
CT2	CT2	CT2	CT3	0.15	1	0
HA	CT1	CN7B	HA	0.30	3	0
HA	CT1	CN7B	NR1	0.3198	3	0
CT1	CN7B	NR1	CPH2	-0.4718	1	0
CT1	CN7B	NR1	CPH1	0.3561	1	0

[TCM⁻] [All parameters from Ref. 234]

Atom 1	Atom 2	Atom 3	Atom 4	k_z (kcal mol ⁻¹)	n	δ (deg)
NC	CN	CCM	CN	0.00	2	180

Table B6: Improper dihedral angle parameters.

[C₂mim⁺], [C₃mim⁺], [C₈mim⁺] [All parameters from Ref. 167]

Atom 1	Atom 2	Atom 3	Atom 4	k_{ψ} (kcal mol ⁻¹ rad ⁻²)	ψ (deg)
CPH2	NR1	NR2	HR1	0.5	0
NR1	CPH1	CPH2	CN7B	0.6	0
NR2	CPH1	CPH2	CN7B	0.6	0
CPH1	CPH1	NR2	HR3	0.5	0
CPH1	CPH1	NR1	HR3	0.5	0

[TCM-] [All parameters from Ref. 234]

Atom 1	Atom 2	Atom 3	Atom 4	k_{ψ} (kcal mol ⁻¹ rad ⁻²)	ψ (deg)
CCM	CN	CN	NC	26.7	0

Table B7: Lennard-Jones parameters. Note that $\sigma = R_{\text{min}} / \sqrt[6]{2}$

[All cation parameters from Refs. 167,205,219]

Atom	ϵ (kcal mol ⁻¹)	$R_{\text{min}}/2(\text{\AA})$
CPH1	0.050	1.800
NR1	0.200	1.850
CPH2	0.050	1.800
NR2	0.200	1.850
HR3	0.0078	1.468
HR1	0.046	0.900
CN7B	0.020	2.275
HA	0.022	1.320
CT3	0.080	2.060
CT2	0.055	2.175
CT1	0.1094	1.0982
CCM	0.024	1.99
CN	0.13	1.75
NC	0.39	1.72

Table B8: Partial Atomic Charges (e^-) from isolated ions uniformly scaled to $\pm 0.7e^-$ total ionic charge.

Atom type [C ₂ mim ⁺]	Atom type [C ₄ mim ⁺]	Atom type [C ₈ mim ⁺]	numbering
NR2 7.913710E-02	NR2 7.768320E-02	NR2 6.190170E-02	1
CPH2 8.136100E-03	CPH2 3.794700E-03	CPH2 8.299900E-03	2
NR1 7.993650E-02	NR1 7.871360E-02	NR1 6.596870E-02	3
CPH1 5.217100E-03	CPH1 1.753500E-03	CPH1 2.936640E-02	4
CPH1 1.804740E-02	CPH1 2.470790E-02	CPH1 2.322880E-02	5
HR1 7.331800E-02	HR1 7.207620E-02	HR1 8.014580E-02	6
HR3 5.905410E-02	HR3 5.658100E-02	HR3 3.577910E-02	7
HR3 4.886630E-02	HR3 4.231150E-02	HR3 3.391850E-02	8
CN7B 2.942317E-01	CN7B 3.153423E-01	CN7B 3.280578E-01	9
HA -5.328260E-02	HA -6.275360E-02	HA -5.464060E-02	10
HA -3.957730E-02	HA -4.802770E-02	HA -6.730640E-02	11
HA -4.628890E-02	HA -5.465670E-02	HA -6.161330E-02	12
CN7B 2.350215E-01	CN7B 2.288811E-01	CN7B 2.044350E-01	13
HA -4.897480E-02	HA -4.591720E-02	HA -2.954420E-02	14
HA -3.369590E-02	HA -3.136210E-02	HA -4.034450E-02	15
CT1 1.361640E-01	CT2 6.320860E-02	CT2 7.145040E-02	16
HA -3.310860E-02	HA -2.674910E-02	HA -3.868270E-02	17
HA -5.320350E-02	HA -4.666690E-02	HA -3.035410E-02	18
HA -2.899820E-02	CT2 1.742440E-01	CT2 1.474193E-01	19
	HA -6.531070E-02	HA -5.246360E-02	20
	HA -6.488090E-02	HA -5.276950E-02	21
	CT3 2.112537E-01	CT2 1.053262E-01	22
	HA -6.813660E-02	HA -4.761120E-02	23
	HA -6.630610E-02	HA -4.840010E-02	24
	HA -6.978370E-02	CT2 1.391250E-01	25
		HA -5.651730E-02	26
		HA -5.659500E-02	27

		CT2 1.241422E-01	28
		HA -5.793060E-02	29
		HA -5.741540E-02	30
		CT2 1.438031E-01	31
		HA -6.833680E-02	32
		HA -6.801130E-02	33
		CT3 2.492252E-01	34
		HA -8.511160E-02	35
		HA -9.185680E-02	36
		HA -8.608810E-02	37

Partial charges for [TCM ⁻] (e ⁻)	numbering
CCM -3.576790E-01	1
CN 3.960887E-01	2
NC -5.101957E-01	3
CN 3.960887E-01	4
NC -5.101957E-01	5
CN 3.960887E-01	6
NC -5.101957E-01	7

Table B9: Mass density calculations for the three ILs at different temperatures and 1 bar. In all cases, the statistical uncertainty is less than 0.001.

<i>T</i> (K)	Mass Density (gr/cm ³)		
	[C ₂ mim ⁺][TCM ⁻]	[C ₄ mim ⁺][TCM ⁻]	[C ₈ mim ⁺][TCM ⁻]
298.15	1.0963	1.0500	0.9918
363.15	1.0414	0.09979	0.9427
398.15	1.0125	0.9698	0.9166

Table B10: Anions' and cations' self-diffusion coefficients of the center of mass for the three ILs at different temperatures and 1 bar.

<i>T</i> (K)	Self Diffusion Coefficients ($10^{-7}\text{cm}^2/\text{s}$)					
	[C ₂ mim ⁺][TCM ⁻]		[C ₄ mim ⁺][TCM ⁻]		[C ₈ mim ⁺][TCM ⁻]	
	Anion	Cation	Anion	Cation	Anion	Cation
298.15	3.3	3.6	2.8	2.7	1.1	0.9
363.15	18.0	16.4	13.6	13.0	11.6	7.3
398.15	30.7	28.8	28.2	24.2	20.0	14.1

Table B11: Viscosity calculations for the three ILs at different temperatures and 1 bar.

<i>T</i> (K)	Viscosity (Pa*s)		
	[C ₂ mim ⁺][TCM ⁻]	[C ₄ mim ⁺][TCM ⁻]	[C ₈ mim ⁺][TCM ⁻]
298.15	0.048	0.08	0.11
363.15	0.006 ₃	0.006 ₃	0.01 ₃
398.15	0.004 ₃	0.0045 ₃	0.006 ₃

Appendix C: Force Field Parameters for Gasses

Figure C1: Labeling of the particles for (a) CO₂, (b) N₂, (c) O₂, (d) Ar and, (e) CH₄.

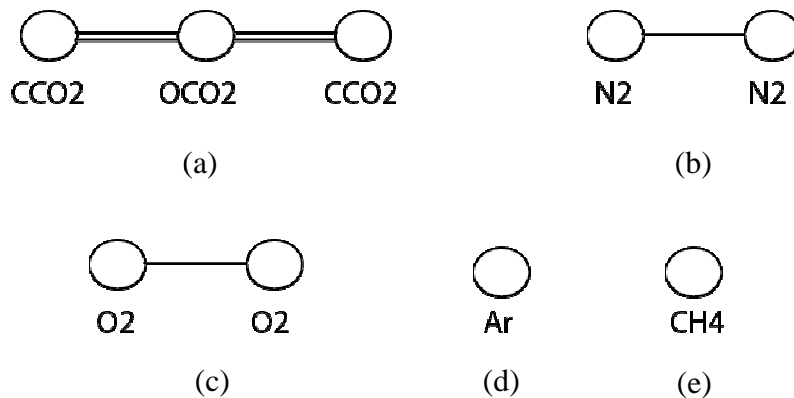


Table C1: Bond force constants (k_b) and equilibrium bond distances (b_0).

[All parameters from Refs. 241,244]

Atom 1	Atom 2	K_b (kcal mol ⁻¹ Å ⁻²)	b_0 (Å)
CCO2	OCCO2	900.00	1.1490
O2	O2	600.00	1.2100
N2	N2	1000.0	1.0897

Table C2: Bond angle bending parameters (k_θ) and equilibrium angles (θ_0).

[All parameters from Ref. 241]

Atom 1	Atom 2	Atom 3	K_θ (kcal mol ⁻¹ rad ⁻²)	θ_0 (deg)
CCO2	OCO2	CCO2	295.40	180.00

Table C3: Lennard-Jones parameters. Note that $\sigma = R_{\min} / \sqrt[6]{2}$

[All parameters from Refs. 241-245]

Atom	ϵ (kcal mol ⁻¹)	$R_{\min}/2(\text{\AA})$
CCO2	0.0559	1.5473
OCO2	0.1600	1.7022
CH4	0.2941	2.0930
Ar	0.2385	1.9082
O2	0.0956	1.7005
N2	0.0715	1.8577

Table C4: Partial Atomic Charges (e⁻).

[Parameters from Ref. 241]

Atom	Atomic Charge (e ⁻)
CCO2	0.6512
OCO2	-0.3256

References

- 1 Fredlake, C. P., Crosthwaite, J. M., Hert, D. G., Aki, S. N. V. K. & Brennecke, J. F. Thermophysical properties of imidazolium-based ionic liquids. *Journal of Chemical and Engineering Data* **49**, 954-964, (2004).
- 2 Maginn, E. J. Molecular simulation of ionic liquids: Current status and future opportunities. *Journal of Physics Condensed Matter* **21**, (2009).
- 3 Walden, P. Molecular weights and electrical conductivity of several fused salts. *Bull. Acad. Sci. St. Petersburg*, 405-422, (1914).
- 4 Wilkes, J. S. & Zaworotko, M. J. Air and water stable 1-ethyl-3-methylimidazolium based ionic liquids. *Journal of the Chemical Society, Chemical Communications*, 965-967, (1992).
- 5 Cooper, E. I. & O'Sullivan, E. J. M. *New, stable, ambient-temperature molten salts in the "Eighth International Molten Salts Symposium"*. Vol. 92-16 386-396 (eds. R.J. Gale, G. Blomgren and H. Kojima, The electrochemical Society, Inc. Pennington, New Jersey, 1992).
- 6 Plechkova, N. V. & Seddon, K. R. Applications of ionic liquids in the chemical industry. *Chemical Society Reviews* **37**, 123-150, (2008).
- 7 Gordon, C. M., Muldoon, M. J., Wagner, M., Hilgers, C., Davis, J. H. & Wasserscheid, P. in *Ionic Liquids in Synthesis* 7-55 (Wiley-VCH Verlag GmbH & Co. KGaA, 2008).
- 8 Seddon, K. R., Stark, A. & Torres, M. J. Influence of chloride, water, and organic solvents on the physical properties of ionic liquids. *Pure and Applied Chemistry* **72**, 2275-2287, (2000).
- 9 Deetlefs, M. & Seddon, K. R. in *Handbook of Green Chemistry* (Wiley-VCH Verlag GmbH & Co. KGaA, 2010).
- 10 Tokuda, H., Hayamizu, K., Ishii, K., Susan, M. A. B. H. & Watanabe, M. Physicochemical Properties and Structures of Room Temperature Ionic Liquids. 1. Variation of Anionic Species. *The Journal of Physical Chemistry B* **108**, 16593-16600, (2004).
- 11 Tokuda, H., Hayamizu, K., Ishii, K., Susan, M. A. B. H. & Watanabe, M. Physicochemical Properties and Structures of Room Temperature Ionic Liquids. 2. Variation of Alkyl Chain Length in Imidazolium Cation. *The Journal of Physical Chemistry B* **109**, 6103-6110, (2005).
- 12 Gomes De Azevedo, R., Esperança, J. M. S. S., Szydlowski, J., Visak, Z. P., Pires, P. F., Guedes, H. J. R. & Rebelo, L. P. N. Thermophysical and thermodynamic properties of ionic liquids over an extended pressure range: [bmim][NTf₂] and [hmim][NTf₂]. *Journal of Chemical Thermodynamics* **37**, 888-899, (2005).
- 13 Hardacre, C., Holbrey, J. D., McMath, S. E. J., Bowron, D. T. & Soper, A. K. Structure of molten 1,3-dimethylimidazolium chloride using neutron diffraction. *The Journal of Chemical Physics* **118**, 273-278, (2003).

- 14 Jacquemin, J., Husson, P., Padua, A. A. H. & Majer, V. Density and viscosity of several pure and water-saturated ionic liquids. *Green Chemistry* **8**, 172-180, (2006).
- 15 Jacquemin, J., Husson, P., Majer, V. & Costa Gomes, M. Influence of the Cation on the Solubility of CO₂ and H₂ in Ionic Liquids Based on the Bis(trifluoromethylsulfonyl)imide Anion. *Journal of Solution Chemistry* **36**, 967-979, (2007).
- 16 Gardas, R. L., Freire, M. G., Carvalho, P. J., Marrucho, I. M., Fonseca, I. M. A., Ferreira, A. G. M. & Coutinho, J. A. P. PpT measurements of imidazolium-based ionic liquids. *Journal of Chemical and Engineering Data* **52**, 1881-1888, (2007).
- 17 Wandschneider, A., Lehmann, J. K. & Heintz, A. Surface Tension and Density of Pure Ionic Liquids and Some Binary Mixtures with 1-Propanol and 1-Butanol. *Journal of Chemical & Engineering Data* **53**, 596-599, (2008).
- 18 Krummen, M., Wasserscheid, P. & Gmehling, J. Measurement of activity coefficients at infinite dilution in ionic liquids using the dilutor technique. *Journal of Chemical and Engineering Data* **47**, 1411-1417, (2002).
- 19 Heintz, A., Kulikov, D. V. & Verevkin, S. P. Thermodynamic properties of mixtures containing ionic liquids. 2. Activity coefficients at infinite dilution of hydrocarbons and polar solutes in 1-methyl-3-ethyl-imidazolium bis(trifluoromethyl-sulfonyl) amide and in 1,2-dimethyl-3-ethyl-imidazolium bis(trifluoromethyl-sulfonyl) amide using gas-liquid chromatography. *Journal of Chemical and Engineering Data* **47**, 894-899, (2002).
- 20 Esperança, J. M. S. S., Visak, Z. P., Plechkova, N. V., Seddon, K. R., Guedes, H. J. R. & Rebelo, L. P. N. Density, speed of sound, and derived thermodynamic properties of ionic liquids over an extended pressure range. 4. [C3mim][NTf₂] and [C5mim][NTf₂]. *Journal of Chemical and Engineering Data* **51**, 2009-2015, (2006).
- 21 Huddleston, J. G., Visser, A. E., Reichert, W. M., Willauer, H. D., Broker, G. A. & Rogers, R. D. Characterization and comparison of hydrophilic and hydrophobic room temperature ionic liquids incorporating the imidazolium cation. *Green Chemistry* **3**, 156-164, (2001).
- 22 Fitchett, B. D., Knepp, T. N. & Conboy, J. C. 1-Alkyl-3-methylimidazolium Bis(perfluoroalkylsulfonyl)imide Water-Immiscible Ionic Liquids: The Effect of Water on Electrochemical and Physical Properties. *Journal of the Electrochemical Society* **151**, E219-E225, (2004).
- 23 Kato, R. & Gmehling, J. Systems with ionic liquids: Measurement of VLE and γ_∞ data and prediction of their thermodynamic behavior using original UNIFAC, mod. UNIFAC(DO) and COSMO-RS(OI). *Journal of Chemical Thermodynamics* **37**, 603-619, (2005).
- 24 Kumelan, J., Pérez-Salado Kamps, Á., Tuma, D. & Maurer, G. Solubility of CO₂ in the ionic liquid [hmim][Tf₂N]. *The Journal of Chemical Thermodynamics* **38**, 1396-1401, (2006).
- 25 Muhammad, A., Abdul Mutalib, M. I., Wilfred, C. D., Murugesan, T. & Shafeeq, A. Thermophysical properties of 1-hexyl-3-methyl imidazolium based ionic liquids with tetrafluoroborate, hexafluorophosphate and bis(trifluoromethylsulfonyl)imide anions. *The Journal of Chemical Thermodynamics* **40**, 1433-1438, (2008).

- 26 Łachwa, J., Morgado, P., Esperança, J. M. S. S., Guedes, H. J. R., Canongia Lopes, J. N. & Rebelo, L. P. N. Fluid-Phase Behavior of {1-Hexyl-3-methylimidazolium Bis(trifluoromethylsulfonyl) Imide, [C6mim][NTf2], + C2–C8 n-Alcohol} Mixtures: Liquid–Liquid Equilibrium and Excess Volumes‡. *Journal of Chemical & Engineering Data* **51**, 2215-2221, (2006).
- 27 Widegren, J. A. & Magee, J. W. Density, Viscosity, Speed of Sound, and Electrolytic Conductivity for the Ionic Liquid 1-Hexyl-3-methylimidazolium Bis(trifluoromethylsulfonyl)imide and Its Mixtures with Water†. *Journal of Chemical & Engineering Data* **52**, 2331-2338, (2007).
- 28 Kandil, M. E., Marsh, K. N. & Goodwin, A. R. H. Measurement of the Viscosity, Density, and Electrical Conductivity of 1-Hexyl-3-methylimidazolium Bis(trifluoromethylsulfonyl)imide at Temperatures between (288 and 433) K and Pressures below 50 MPa. *Journal of Chemical & Engineering Data* **52**, 2382-2387, (2007).
- 29 Alonso, L., Arce, A., Francisco, M. & Soto, A. Measurement and Correlation of Liquid–Liquid Equilibria of Two Imidazolium Ionic Liquids with Thiophene and Methylcyclohexane. *Journal of Chemical & Engineering Data* **52**, 2409-2412, (2007).
- 30 Alonso, L., Arce, A., Francisco, M. a. & Soto, A. Liquid–Liquid Equilibria for [C8mim][NTf2] + Thiophene + 2,2,4-Trimethylpentane or + Toluene. *Journal of Chemical & Engineering Data* **53**, 1750-1755, (2008).
- 31 Alonso, L., Arce, A., Francisco, M. & Soto, A. (Liquid + liquid) equilibria of [C8mim][NTf2] ionic liquid with a sulfur-component and hydrocarbons. *The Journal of Chemical Thermodynamics* **40**, 265-270, (2008).
- 32 Zaitsau, D. H., Kabo, G. J., Strechan, A. A., Paulechka, Y. U., Tschersich, A., Verevkin, S. P. & Heintz, A. Experimental Vapor Pressures of 1-Alkyl-3-methylimidazolium Bis(trifluoromethylsulfonyl)imides and a Correlation Scheme for Estimation of Vaporization Enthalpies of Ionic Liquids. *The Journal of Physical Chemistry A* **110**, 7303-7306, (2006).
- 33 Tomé, L. I. N., Carvalho, P. J., Freire, M. G., Marrucho, I. M., Fonseca, I. M. A., Ferreira, A. G. M., Coutinho, J. A. P. & Gardas, R. L. Measurements and correlation of high-pressure densities of imidazolium-based ionic liquids. *Journal of Chemical and Engineering Data* **53**, 1914-1921, (2008).
- 34 Umecky, T., Kanakubo, M. & Ikushima, Y. Self-diffusion coefficients of 1-butyl-3-methylimidazolium hexafluorophosphate with pulsed-field gradient spin-echo NMR technique. *Fluid Phase Equilibria* **228–229**, 329-333, (2005).
- 35 Kanakubo, M., Harris, K. R., Tsuchihashi, N., Ibuki, K. & Ueno, M. Effect of Pressure on Transport Properties of the Ionic Liquid 1-Butyl-3-methylimidazolium Hexafluorophosphate. *The Journal of Physical Chemistry B* **111**, 2062-2069, (2007).
- 36 Holbrey, J. D. *et al.* in *Ionic Liquids in Synthesis* 57-174 (Wiley-VCH Verlag GmbH & Co. KGaA, 2008).
- 37 Aparicio, S., Atilhan, M. & Karadas, F. Thermophysical Properties of Pure Ionic Liquids: Review of Present Situation. *Industrial & Engineering Chemistry Research* **49**, 9580-9595, (2010).

- 38 de Andrade, J., Böes, E. S. & Stassen, H. A Force Field for Liquid State Simulations on Room Temperature Molten Salts: 1-Ethyl-3-methylimidazolium Tetrachloroaluminate. *The Journal of Physical Chemistry B* **106**, 3546-3548, (2002).
- 39 Takahashi, S., Suzuya, K., Kohara, S., Koura, N., Curtiss, L. A. & Saboungi, M.-L. Structure of 1-Ethyl-3-Methylimidazolium Chloroaluminates: Neutron Diffraction Measurements and ab initio Calculations. *Phys Chem (Munich)* **209**, 209-221, (1999).
- 40 Hardacre, C., McMath, S. E. J., Nieuwenhuyzen, M., Bowron, D. T. & Soper, A. K. Liquid structure of 1, 3-dimethylimidazolium salts. *Journal of Physics: Condensed Matter* **15**, S159, (2003).
- 41 Castner, E. W. & Wishart, J. F. Spotlight on ionic liquids. *Journal of Chemical Physics* **132**, (2010).
- 42 Triolo, A., Russina, O., Bleif, H. J. & Di Cola, E. Nanoscale segregation in room temperature ionic liquids. *Journal of Physical Chemistry B* **111**, 4641-4644, (2007).
- 43 Russina, O. *et al.* Morphology and intermolecular dynamics of 1-Alkyl-3-methylimidazolium bis{(trifluoromethane)sulfonyl}amide ionic liquids: Structural and dynamic evidence of nanoscale segregation. *Journal of Physics Condensed Matter* **21**, (2009).
- 44 Canongia Lopes, J. N. A. & Pádua, A. A. H. Nanostructural organization in ionic liquids. *Journal of Physical Chemistry B* **110**, 3330-3335, (2006).
- 45 Logotheti, G. E., Ramos, J. & Economou, I. G. Molecular Modeling of Imidazolium-Based [Tf₂N⁻] Ionic Liquids: Microscopic Structure, Thermodynamic and Dynamic Properties, and Segmental Dynamics. *The Journal of Physical Chemistry B* **113**, 7211-7224, (2009).
- 46 Pádua, A. A. H., Costa Gomes, M. F. & Canongia Lopes, J. N. A. Molecular solutes in ionic liquids: A structural perspective. *Accounts of Chemical Research* **40**, 1087-1096, (2007).
- 47 Wang, Y. & Voth, G. A. Unique spatial heterogeneity in ionic liquids. *Journal of the American Chemical Society* **127**, 12192-12193, (2005).
- 48 Wang, Y. & Voth, G. A. Tail aggregation and domain diffusion in ionic liquids. *Journal of Physical Chemistry B* **110**, 18601-18608, (2006).
- 49 Wang, Y., Jiang, W., Yan, T. & Voth, G. A. Understanding ionic liquids through atomistic and coarse-grained molecular dynamics simulations. *Accounts of Chemical Research* **40**, 1193-1199, (2007).
- 50 Ishida, T. & Shirota, H. Dicationic versus monocationic ionic liquids: Distinctive ionic dynamics and dynamical heterogeneity. *Journal of Physical Chemistry B* **117**, 1136-1150, (2013).
- 51 Liu, H. & Maginn, E. A molecular dynamics investigation of the structural and dynamic properties of the ionic liquid 1-n-butyl-3-methylimidazolium bis(trifluoromethanesulfonyl) imide. *Journal of Chemical Physics* **135**, (2011).

- 52 Urahata, S. M. & Ribeiro, M. C. C. Unraveling dynamical heterogeneity in the ionic liquid 1-butyl-3-methylimidazolium chloride. *Journal of Physical Chemistry Letters* **1**, 1738-1742, (2010).
- 53 Urahata, S. M. & Ribeiro, M. C. C. Single particle dynamics in ionic liquids of 1-alkyl-3-methylimidazolium cations. *The Journal of Chemical Physics* **122**, 024511, (2005).
- 54 Del Pópolo, M. G. & Voth, G. A. On the structure and dynamics of ionic liquids. *Journal of Physical Chemistry B* **108**, 1744-1752, (2004).
- 55 Hu, Z. & Margulis, C. J. Room-temperature ionic liquids: Slow dynamics, viscosity, and the red edge effect. *Accounts of Chemical Research* **40**, 1097-1105, (2007).
- 56 Hu, Z. & Margulis, C. J. Heterogeneity in a room-temperature ionic liquid: Persistent local environments and the red-edge effect. *Proceedings of the National Academy of Sciences of the United States of America* **103**, 831-836, (2006).
- 57 Habasaki, J. & Ngai, K. L. Molecular dynamics studies of ionically conducting glasses and ionic liquids: Wave number dependence of intermediate scattering function. *Journal of Chemical Physics* **133**, (2010).
- 58 Habasaki, J. & Ngai, K. L. Multifractal nature of heterogeneous dynamics and structures in glass forming ionic liquids. *Journal of Non-Crystalline Solids* **357**, 446-453, (2011).
- 59 Androulaki, E., Vergadou, N., Ramos, J. & Economou, I. G. Structure, thermodynamic and transport properties of imidazolium-based bis(trifluoromethylsulfonyl)imide ionic liquids from molecular dynamics simulations. *Molecular Physics* **110**, 1139-1152, (2012).
- 60 Gardas, R. L. & Coutinho, J. A. P. A group contribution method for viscosity estimation of ionic liquids. *Fluid Phase Equilibria* **266**, 195-201, (2008).
- 61 Weingärtner, H. Understanding ionic liquids at the molecular level: Facts, problems, and controversies. *Angewandte Chemie - International Edition* **47**, 654-670, (2008).
- 62 Xu, W., Cooper, E. I. & Angell, C. A. Ionic liquids: Ion mobilities, glass temperature, and fragilities. *J. Phys. Chem. B* **107**, 6170-6178, (2003).
- 63 Kob, W., Donati, C., Plimpton, S. J., Poole, P. H. & Glotzer, S. C. Dynamical heterogeneities in a supercooled Lennard-Jones liquid. *Physical Review Letters* **79**, 2827-2830, (1997).
- 64 Sillescu, H. Heterogeneity at the glass transition: a review. *Journal of Non-Crystalline Solids* **243**, 81-108, (1999).
- 65 Donati, C., Glotzer, S. C., Poole, P. H., Kob, W. & Plimpton, S. J. Spatial correlations of mobility and immobility in a glass-forming Lennard-Jones liquid. *Physical Review E* **60**, 3107, (1999).
- 66 Qian, J., Hentschke, R. & Heuer, A. On the origin of dynamic heterogeneities in glass-forming liquids. *The Journal of Chemical Physics* **111**, 10177-10182, (1999).

- 67 Chaudhuri, P., Sastry, S. & Kob, W. Tracking Heterogeneous Dynamics During the α Relaxation of a Simple Glass Former. *Physical Review Letters* **101**, 190601, (2008).
- 68 Ranko, R. Heterogeneous dynamics in liquids: fluctuations in space and time. *Journal of Physics: Condensed Matter* **14**, R703, (2002).
- 69 Jin, H., Li, X. & Maroncelli, M. Heterogeneous Solute Dynamics in Room Temperature Ionic Liquids. *The Journal of Physical Chemistry B* **111**, 13473-13478, (2007).
- 70 Mandal, P. K., Sarkar, M. & Samanta, A. Excitation-Wavelength-Dependent Fluorescence Behavior of Some Dipolar Molecules in Room-Temperature Ionic Liquids. *The Journal of Physical Chemistry A* **108**, 9048-9053, (2004).
- 71 Paul, A., Mandal, P. K. & Samanta, A. On the Optical Properties of the Imidazolium Ionic Liquids. *The Journal of Physical Chemistry B* **109**, 9148-9153, (2005).
- 72 Ito, N., Arzhantsev, S. & Maroncelli, M. The probe dependence of solvation dynamics and rotation in the ionic liquid 1-butyl-3-methyl-imidazolium hexafluorophosphate. *Chemical Physics Letters* **396**, 83-91, (2004).
- 73 Ito, N., Arzhantsev, S., Heitz, M. & Maroncelli, M. Solvation Dynamics and Rotation of Coumarin 153 in Alkylphosphonium Ionic Liquids. *The Journal of Physical Chemistry B* **108**, 5771-5777, (2004).
- 74 Aki, S. N. V. K., Brennecke, J. F. & Samanta, A. How polar are room-temperature ionic liquids? *Chemical Communications*, 413-414, (2001).
- 75 Köddermann, T., Ludwig, R. & Paschek, D. On the validity of Stokes-Einstein and Stokes-Einstein-Debye relations in ionic liquids and ionic-liquid mixtures. *ChemPhysChem* **9**, 1851-1858, (2008).
- 76 Tuckerman, M., Berne, B. J. & Martyna, G. J. Reversible multiple time scale molecular dynamics. *The Journal of Chemical Physics* **97**, 1990-2001, (1992).
- 77 Androulaki, E., Vergadou, N. & Economou, I. G. Analysis of the heterogeneous dynamics of imidazolium-based [Tf₂N⁻] ionic liquids using molecular simulation. *Molecular Physics*, doi: 10.1080/00268976.2014.906670.
- 78 Feng, R., Zhao, D. & Guo, Y. Revisiting Characteristics of Ionic Liquids: A Review for Further Application Development. *Journal of Environmental Protection* **01**, 95-104, (2010).
- 79 Wasserscheid, P. & Welton, T. in *Ionic Liquids in Synthesis* 689-704 (Wiley-VCH Verlag GmbH & Co. KGaA, 2008).
- 80 Phillips, B. S. & Zabinski, J. S. Ionic Liquid Lubrication Effects on Ceramics in a Water Environment. *Tribology Letters* **17**, 533-541, (2004).
- 81 Liu, H., Maginn, E., Visser, A. E., Bridges, N. J. & Fox, E. B. Thermal and transport properties of six ionic liquids: An experimental and molecular dynamics study. *Industrial and Engineering Chemistry Research* **51**, 7242-7254, (2012).

- 82 Weidlich, T., Stočes, M. & Švancara, I. *Sensing in Electroanalysis* Vol. null (edited by K. Vytrás and K. Kalcher, University Press Center, Pardubice, Czech Republic, 2010).
- 83 Ramkumar, S., Upul Wijayantha, K.-G., Velayutham, D. & Anandan, S. Synthesis of 1, 3-dihexyl-2-(phenylthio)-1H-benzo[d]imidazol-3-ium iodide—A new ionic liquid for dye sensitized solar cell applications. *Journal of Molecular Liquids* **193**, 185-188, (2014).
- 84 Lu, J., Yan, F. & Texter, J. Advanced applications of ionic liquids in polymer science. *Progress in Polymer Science* **34**, 431-448, (2009).
- 85 Sun, X. G. & Dai, S. Electrochemical investigations of ionic liquids with vinylene carbonate for applications in rechargeable lithium ion batteries. *Electrochimica Acta* **55**, 4618-4626, (2010).
- 86 Ramunno, M., Pohrer, B., Ebel, N., Wasserscheid, P. & Schlücker, E. 2771-2775.
- 87 Kondo, Y., Koyama, T., Tsuboi, R., Nakano, M., Miyake, K. & Sasaki, S. Tribological Performance of Halogen-Free Ionic Liquids as Lubricants of Hard Coatings and Ceramics. *Tribology Letters* **51**, 243-249, (2013).
- 88 Kubisa, P. Application of ionic liquids as solvents for polymerization processes. *Progress in Polymer Science* **29**, 3-12, (2004).
- 89 Shen, Y., Tang, H. & Ding, S. Catalyst separation in atom transfer radical polymerization. *Progress in Polymer Science* **29**, 1053-1078, (2004).
- 90 Quijano, G., Couvert, A. & Amrane, A. Ionic liquids: Applications and future trends in bioreactor technology. *Bioresource Technology* **101**, 8923-8930, (2010).
- 91 Yang, Z. & Pan, W. Ionic liquids: Green solvents for nonaqueous biocatalysis. *Enzyme and Microbial Technology* **37**, 19-28, (2005).
- 92 Marszalek, M., Fei, Z., Zhu, D.-R., Scopelliti, R., Dyson, P. J., Zakeeruddin, S. M. & Grätzel, M. Application of Ionic Liquids Containing Tricyanomethanide [C(CN)₃]⁻ or Tetracyanoborate [B(CN)₄]⁻ Anions in Dye-Sensitized Solar Cells. *Inorganic Chemistry* **50**, 11561-11567, (2011).
- 93 Bidikoudi, M., Stergiopoulos, T., Likodimos, V., Romanos, G. E., Francisco, M., Iliev, B., Adamova, G., Schubert, T. J. S. & Falaras, P. Ionic liquid redox electrolytes based on binary mixtures of 1-alkyl-methylimidazolium tricyanomethanide with 1-methyl-3-propylimidazolium iodide and implication in dye-sensitized solar cells. *Journal of Materials Chemistry A* **1**, 10474-10486, (2013).
- 94 Wang, P., Kantlehner, W., Mezger, J., Stoyanov, E. V., Zakeeruddin, S. M. & Grätzel, M. in *206th Electrochemical Society Meeting*. 37-44.
- 95 Dai, Q., Menzies, D. B., MacFarlane, D. R., Batten, S. R., Forsyth, S., Spiccia, L., Cheng, Y.-B. & Forsyth, M. Dye-sensitized nanocrystalline solar cells incorporating ethylmethylimidazolium-based ionic liquid electrolytes. *Comptes Rendus Chimie* **9**, 617-621, (2006).

- 96 Wang, P. *et al.* Charge Separation and Efficient Light Energy Conversion in Sensitized Mesoscopic Solar Cells Based on Binary Ionic Liquids. *Journal of the American Chemical Society* **127**, 6850-6856, (2005).
- 97 Wang, P., Zakeeruddin, S. M., Grätzel, M., Kantlehner, W., Mezger, J., Stoyanov, E. V. & Scherr, O. Novel room temperature ionic liquids of hexaalkyl substituted guanidinium salts for dye-sensitized solar cells. *Appl Phys A* **79**, 73-77, (2004).
- 98 Hagfeldt, A., Boschloo, G., Sun, L., Kloo, L. & Pettersson, H. Dye-Sensitized Solar Cells. *Chemical Reviews* **110**, 6595-6663, (2010).
- 99 Cao, Y., Zhang, J., Bai, Y., Li, R., Zakeeruddin, S. M., Grätzel, M. & Wang, P. Dye-sensitized solar cells with solvent-free ionic liquid electrolytes. *J. Phys. Chem. C* **112**, 13775-13781, (2008).
- 100 Kuang, D., Uchida, S., Humphry-Baker, R., Zakeeruddin, S. M. & Grätzel, M. Organic Dye-Sensitized Ionic Liquid Based Solar Cells: Remarkable Enhancement in Performance through Molecular Design of Indoline Sensitizers. *Angewandte Chemie International Edition* **47**, 1923-1927, (2008).
- 101 Zistler, M., Wachter, P., Schreiner, C., Fleischmann, M., Gerhard, D., Wasserscheid, P., Hinsch, A. & Gores, H. J. Temperature dependent impedance analysis of binary ionic liquid electrolytes for dye-sensitized solar cells. *Journal of the Electrochemical Society* **154**, B925-B930, (2007).
- 102 Kuang, D., Klein, C., Zhang, Z., Ito, S., Moser, J.-E., Zakeeruddin, S. M. & Grätzel, M. Stable, High-Efficiency Ionic-Liquid-Based Mesoscopic Dye-Sensitized Solar Cells. *Small* **3**, 2094-2102, (2007).
- 103 Kuang, D. Stable mesoscopic dye-sensitized solar cells based on tetracyanoborate ionic liquid electrolyte. *J. Am. Chem. Soc.* **128**, 7732-7733, (2006).
- 104 Wang, P. Charge separation and efficient light energy conversion in sensitized mesoscopic solar cells based on binary ionic liquids. *J. Am. Chem. Soc.* **127**, 6850-6856, (2005).
- 105 Wang, P. A new ionic liquid electrolyte enhances the conversion efficiency of dye-sensitized solar cells. *J. Phys. Chem. B* **107**, 13280-13285, (2003).
- 106 Kubo, W. Quasi-solid-state dye-sensitized solar cells using room temperature molten salts and a low molecular weight gelator. *Chem. Commun.*, 374-375, (2002).
- 107 Labropoulos, A. I. *et al.* Alkyl-methylimidazolium Tricyanomethanide Ionic Liquids under Extreme Confinement onto Nanoporous Ceramic Membranes. *The Journal of Physical Chemistry C* **117**, 10114-10127, (2013).
- 108 Tzialla, O. *et al.* Zeolite Imidazolate Framework-Ionic Liquid Hybrid Membranes for Highly Selective CO₂ Separation. *The Journal of Physical Chemistry C* **117**, 18434-18440, (2013).
- 109 Romanos, G. E., Zubeir, L. F., Likodimos, V., Falaras, P., Kroon, M. C., Iliev, B., Adamova, G. & Schubert, T. J. S. Enhanced CO₂ Capture in Binary Mixtures of 1-Alkyl-3-methylimidazolium Tricyanomethanide Ionic Liquids with Water. *The Journal of Physical Chemistry B* **117**, 12234-12251, (2013).

- 110 Holloway, S., Pearce, J. M., Hards, V. L., Ohsumi, T. & Gale, J. Natural emissions of CO₂ from the geosphere and their bearing on the geological storage of carbon dioxide. *Energy* **32**, 1194-1201, (2007).
- 111 Boot-Handford, M. E. *et al.* Carbon capture and storage update. *Energy & Environmental Science* **7**, 130-189, (2014).
- 112 Pires, J. C. M., Martins, F. G., Alvim-Ferraz, M. C. M. & Simões, M. Recent developments on carbon capture and storage: An overview. *Chemical Engineering Research and Design* **89**, 1446-1460, (2011).
- 113 Zhang, X., Zhang, X., Dong, H., Zhao, Z., Zhang, S. & Huang, Y. Carbon capture with ionic liquids: overview and progress. *Energy & Environmental Science* **5**, 6668-6681, (2012).
- 114 Zhao, Z., Dong, H. & Zhang, X. The Research Progress of CO₂ Capture with Ionic Liquids. *Chinese Journal of Chemical Engineering* **20**, 120-129, (2012).
- 115 Myers, C., Pennline, H., Luebke, D., Ilconich, J., Dixon, J. K., Maginn, E. J. & Brennecke, J. F. High temperature separation of carbon dioxide/hydrogen mixtures using facilitated supported ionic liquid membranes. *Journal of Membrane Science* **322**, 28-31, (2008).
- 116 Muhammad, N., Man, Z. & Bustam Khalil, M. Ionic liquid—a future solvent for the enhanced uses of wood biomass. *Eur. J. Wood Prod.* **70**, 125-133, (2012).
- 117 Hyvärinen, S., Mikkola, J. P., Murzin, D. Y., Vaher, M., Kaljurand, M. & Koel, M. Sugars and sugar derivatives in ionic liquid media obtained from lignocellulosic biomass: Comparison of capillary electrophoresis and chromatographic analysis. *Catalysis Today*, (2013).
- 118 Tadesse, H. & Luque, R. Advances on biomass pretreatment using ionic liquids: An overview. *Energy and Environmental Science* **4**, 3913-3929, (2011).
- 119 Meindersma, G. W., Hansmeier, A. R. & de Haan, A. B. Ionic Liquids for Aromatics Extraction. Present Status and Future Outlook. *Industrial & Engineering Chemistry Research* **49**, 7530-7540, (2010).
- 120 Cha, E. H., Lim, S. A., Park, J. H., Kim, D. W. & Macfarlane, D. R. Ionic conductivity studies of gel polyelectrolyte based on ionic liquid. *Journal of Power Sources* **178**, 779-782, (2008).
- 121 Thuy Pham, T. P., Cho, C.-W. & Yun, Y.-S. Environmental fate and toxicity of ionic liquids: A review. *Water Research* **44**, 352-372, (2010).
- 122 For more information visit: http://www.naturalgas.org/naturalgas/processing_ng.asp (accessed Dec 2013).
- 123 Astarita, G. S. D. W. B. A. *Gas treating with chemical solvents*. (John Wiley, 1983).
- 124 Göttlicher, G. & Pruscek, R. Comparison of CO₂ removal systems for fossil-fuelled power plant processes. *Energy Conversion and Management* **38**, S173-S178, (1997).

- 125 Torralba-Calleja, E., Skinner, J. & Gutiérrez-Tauste, D. CO₂ Capture in Ionic Liquids: A Review of Solubilities and Experimental Methods. *Journal of Chemistry* **2013**, 16, (2013).
- 126 Tokuda, H., Ishii, K., Susan, M. A. B. H., Tsuzuki, S., Hayamizu, K. & Watanabe, M. Physicochemical Properties and Structures of Room-Temperature Ionic Liquids. 3. Variation of Cationic Structures. *The Journal of Physical Chemistry B* **110**, 2833-2839, (2006).
- 127 Nguyen-Huynh, D., De Hemptinne, J. C., Lugo, R., Passarello, J. P. & Tobaly, P. Modeling liquid-liquid and liquid-vapor equilibria of binary systems containing water with an alkane, an aromatic hydrocarbon, an alcohol or a gas (methane, ethane, CO₂ or H₂S), using group contribution polar perturbed-chain statistical associating fluid theory. *Industrial and Engineering Chemistry Research* **50**, 7467-7483, (2011).
- 128 Ashrafmansouri, S. S. & Raeissi, S. Modeling gas solubility in ionic liquids with the SAFT- γ group contribution method. *Journal of Supercritical Fluids* **63**, 81-91, (2012).
- 129 Gardas, R. L. & Coutinho, J. A. P. Group contribution methods for the prediction of thermophysical and transport properties of ionic liquids. *AIChE Journal* **55**, 1274-1290, (2009).
- 130 Lazzús, J. A. A group contribution method to predict p-T-P of ionic liquids. *Chemical Engineering Communications* **197**, 974-1015, (2010).
- 131 Grubbs, L. M., Ye, S., Saifullah, M., McMillan-Wiggins, M. C., Acree, W. E., Abraham, M. H., Twu, P. & Anderson, J. L. Correlations for describing gas-to-ionic liquid partitioning at 323K based on ion-specific equation coefficient and group contribution versions of the Abraham model. *Fluid Phase Equilibria* **301**, 257-266, (2011).
- 132 Vijande, J., Piñeiro, M. M., Legido, J. L. & Bessièrès, D. Group-contribution method for the molecular parameters of the pc-saft equation of state taking into account the proximity effect. application to nonassociated compounds. *Industrial and Engineering Chemistry Research* **49**, 9394-9406, (2010).
- 133 Qiao, Y., Ma, Y., Huo, Y., Ma, P. & Xia, S. A group contribution method to estimate the densities of ionic liquids. *Journal of Chemical Thermodynamics* **42**, 852-855, (2010).
- 134 Shen, C., Li, C. X., Li, X. M., Lu, Y. Z. & Muhammad, Y. Estimation of densities of ionic liquids using Patel-Teja equation of state and critical properties determined from group contribution method. *Chemical Engineering Science* **66**, 2690-2698, (2011).
- 135 Valderrama, J. O., Toro, A. & Rojas, R. E. Prediction of the heat capacity of ionic liquids using the mass connectivity index and a group contribution method. *Journal of Chemical Thermodynamics* **43**, 1068-1073, (2011).
- 136 Mutelet, F., Ortega-Villa, V., Moïse, J. C., Jaubert, J. N. & Acree, W. E. Prediction of partition coefficients of organic compounds in ionic liquids using a temperature-dependent linear solvation energy relationship with parameters calculated through a group contribution method. *Journal of Chemical and Engineering Data* **56**, 3598-3606, (2011).

- 137 Revelli, A. L., Mutelet, F. & Jaubert, J. N. Prediction of partition coefficients of organic compounds in ionic liquids: Use of a linear solvation energy relationship with parameters calculated through a group contribution method. *Industrial and Engineering Chemistry Research* **49**, 3883-3892, (2010).
- 138 Maia, F. M., Tsivintzelis, I., Rodriguez, O., Macedo, E. A. & Kontogeorgis, G. M. Equation of state modelling of systems with ionic liquids: Literature review and application with the Cubic Plus Association (CPA) model. *Fluid Phase Equilibria* **332**, 128-143, (2012).
- 139 Llorell, F., Valente, E., Vilaseca, O. & Vega, L. F. Modeling complex associating mixtures with [C n-mim][Tf 2N] ionic liquids: Predictions from the soft-SAFT equation. *Journal of Physical Chemistry B* **115**, 4387-4398, (2011).
- 140 Paduszyński, K., Królikowski, M. & Domańska, U. Excess enthalpies of mixing of piperidinium ionic liquids with short-chain alcohols: Measurements and PC-SAFT modeling. *Journal of Physical Chemistry B* **117**, 3884-3891, (2013).
- 141 Papaioannou, V., Adjiman, C. S., Jackson, G. & Galindo, A. Simultaneous prediction of vapour-liquid and liquid-liquid equilibria (VLE and LLE) of aqueous mixtures with the SAFT- γ group contribution approach. *Fluid Phase Equilibria* **306**, 82-96, (2011).
- 142 Paduszyński, K., Chiyen, J., Ramjugernath, D., Letcher, T. M. & Domańska, U. Liquid-liquid phase equilibrium of (piperidinium-based ionic liquid+an alcohol) binary systems and modelling with NRHB and PCP-SAFT. *Fluid Phase Equilibria* **305**, 43-52, (2011).
- 143 Economou, I. G., Karakatsani, E. K., Logotheti, G. E., Ramos, J. & Vanin, A. A. Multi-scale modeling of structure, dynamic and thermodynamic properties of imidazolium-based ionic liquids: Ab initio DFT calculations, molecular simulation and equation of state predictions. *Oil and Gas Science and Technology* **63**, 283-293, (2008).
- 144 Karakatsani, E. K., Economou, I. G., Kroon, M. C., Bermejo, M. D., Peters, C. J. & Witkamp, G.-J. Equation of state modeling of the phase equilibria of ionic liquid mixtures at low and high pressure. *Physical Chemistry Chemical Physics* **10**, 6160-6168, (2008).
- 145 Karakatsani, E. K., Economou, I. G., Kroon, M. C., Peters, C. J. & Witkamp, G. J. tPC-PSAFT modeling of gas solubility in imidazolium-based ionic liquids. *J. Phys. Chem. C* **111**, 15487-15492, (2007).
- 146 Karakatsani, E. K. & Economou, I. G. Phase equilibrium calculations for multi-component polar fluid mixtures with tPC-PSAFT. *Fluid Phase Equilibria* **261**, 265-271, (2007).
- 147 Kroon, M. C., Karakatsani, E. K., Economou, I. G., Witkamp, G. J. & Peters, C. J. Modeling of the carbon dioxide solubility in imidazolium-based ionic liquids with the tPC-PSAFT equation of state. *Journal of Physical Chemistry B* **110**, 9262-9269, (2006).
- 148 Karakatsani, E. K. & Economou, I. G. Perturbed chain-statistical associating fluid theory extended to dipolar and quadrupolar molecular fluids. *Journal of Physical Chemistry B* **110**, 9252-9261, (2006).

- 149 Allen, M. P. & Tildesley, D. J. *Computer simulation of liquids*. (Clarendon Press, 1989).
- 150 Frenkel, D. & Smit, B. *Understanding Molecular Simulation: From Algorithms to Applications*. (Academic Press, Inc., 1996).
- 151 Paluch, A. S. & Maginn, E. J. Predicting the Solubility of Solid Phenanthrene: A Combined Molecular Simulation and Group Contribution Approach. *AIChE Journal*, (2013).
- 152 Morrow, T. I. & Maginn, E. J. Molecular dynamics study of the ionic liquid 1-n-butyl-3-methylimidazolium hexafluorophosphate. *Journal of Physical Chemistry B* **106**, 12807-12813, (2002).
- 153 Urahata, S. M. & Ribeiro, M. C. C. Structure of ionic liquids of 1-alkyl-3-methylimidazolium cations: A systematic computer simulation study. *The Journal of Chemical Physics* **120**, 1855-1863, (2004).
- 154 Raabe, G. & Köhler, J. Thermodynamical and structural properties of binary mixtures of imidazolium chloride ionic liquids and alcohols from molecular simulation. *The Journal of Chemical Physics* **129**, -, (2008).
- 155 Zhang, Y. & Maginn, E. J. The effect of C2 substitution on melting point and liquid phase dynamics of imidazolium based-ionic liquids: Insights from molecular dynamics simulations. *Physical Chemistry Chemical Physics* **14**, 12157-12164, (2012).
- 156 Koller, T. M., Rausch, M. H., Ramos, J., Schulz, P. S., Wasserscheid, P., Economou, I. G. & Fröba, A. P. Thermophysical Properties of the Ionic Liquids [EMIM][B(CN)₄] and [HMIM][B(CN)₄]. *The Journal of Physical Chemistry B* **117**, 8512-8523, (2013).
- 157 Borodin, O., Zhuang, G. V., Ross, P. N. & Xu, K. Molecular Dynamics Simulations and Experimental Study of Lithium Ion Transport in Dilithium Ethylene Dicarboxate. *The Journal of Physical Chemistry C* **117**, 7433-7444, (2013).
- 158 Borodin, O. & Smith, G. D. Structure and dynamics of N-methyl-N-propylpyrrolidinium bis(trifluoromethanesulfonyl)imide ionic liquid from molecular dynamics simulations. *Journal of Physical Chemistry B* **110**, 11481-11490, (2006).
- 159 Yan, T., Burnham, C. J., Del Popolo, M. G. & Voth, G. A. Molecular dynamics simulation of ionic liquids: The effect of electronic polarizability. *Journal of Physical Chemistry B* **108**, 11877-11881, (2004).
- 160 Zhang, Y. & Maginn, E. J. Toward fully in silico melting point prediction using molecular simulations. *Journal of Chemical Theory and Computation* **9**, 1592-1599, (2013).
- 161 Paluch, A. S., Vitter, C. A., Shah, J. K. & Maginn, E. J. A comparison of the solvation thermodynamics of amino acid analogues in water, 1-octanol and 1-n-alkyl-3-methylimidazolium bis(trifluoromethylsulfonyl) imide ionic liquids by molecular simulation. *Journal of Chemical Physics* **137**, (2012).

- 162 Rai, N. & Maginn, E. J. Critical behaviour and vapour-liquid coexistence of 1-alkyl-3-methylimidazolium bis(trifluoromethylsulfonyl)amide ionic liquids via Monte Carlo simulations. *Faraday Discussions* **154**, 53-69, (2012).
- 163 Wang, Y., Izvenov, S., Yan, T. & Voth, G. A. Multiscale coarse-graining of ionic liquids. *Journal of Physical Chemistry B* **110**, 3564-3575, (2006).
- 164 Karimi-Varzaneh, H. A., Müller-Plathe, F., Balasubramanian, S. & Carbone, P. Studying long-time dynamics of imidazolium-based ionic liquids with a systematically coarse-grained model. *Physical Chemistry Chemical Physics* **12**, 4714-4724, (2010).
- 165 Borodin, O. & Smith, G. D. Structure and Dynamics of N-Methyl-N-propylpyrrolidinium Bis(trifluoromethanesulfonyl)imide Ionic Liquid from Molecular Dynamics Simulations. *The Journal of Physical Chemistry B* **110**, 11481-11490, (2006).
- 166 Borodin, O. Polarizable Force Field Development and Molecular Dynamics Simulations of Ionic Liquids. *The Journal of Physical Chemistry B* **113**, 11463-11478, (2009).
- 167 Cadena, C. & Maginn, E. J. Molecular simulation study of some thermophysical and transport properties of triazolium-based ionic liquids. *Journal of Physical Chemistry B* **110**, 18026-18039, (2006).
- 168 Wang, T., Peng, C., Liu, H., Hu, Y. & Jiang, J. Equation of state for the vapor-liquid equilibria of binary systems containing imidazolium-based ionic liquids. *Industrial and Engineering Chemistry Research* **46**, 4323-4329, (2007).
- 169 Dommert, F., Wendler, K., Berger, R., Delle Site, L. & Holm, C. Force fields for studying the structure and dynamics of ionic liquids: A critical review of recent developments. *ChemPhysChem* **13**, 1625-1637, (2012).
- 170 Bagno, A., D'Amico, F. & Saielli, G. Computer simulation of diffusion coefficients of the room-temperature ionic liquid [bmim][BF₄]: Problems with classical simulation techniques. *Journal of Molecular Liquids* **131-132**, 17-23, (2007).
- 171 Tsuzuki, S. Factors Controlling the Diffusion of Ions in Ionic Liquids. *ChemPhysChem* **13**, 1664-1670, (2012).
- 172 Tsuzuki, S., Shinoda, W., Saito, H., Mikami, M., Tokuda, H. & Watanabe, M. Molecular Dynamics Simulations of Ionic Liquids: Cation and Anion Dependence of Self-Diffusion Coefficients of Ions. *The Journal of Physical Chemistry B* **113**, 10641-10649, (2009).
- 173 Schroder, C. Comparing reduced partial charge models with polarizable simulations of ionic liquids. *Physical Chemistry Chemical Physics* **14**, 3089-3102, (2012).
- 174 Schroder, C. & Steinhauser, O. The influence of electrostatic forces on the structure and dynamics of molecular ionic liquids. *The Journal of Chemical Physics* **128**, 224503, (2008).
- 175 Bhargava, B. L. & Balasubramanian, S. Refined potential model for atomistic simulations of ionic liquid [bmim][PF₆]. *Journal of Chemical Physics* **127**, 6, (2007).

- 176 Sieffert, N. & Wipff, G. The [BMI][Tf2N] ionic liquid/water binary system: A molecular dynamics study of phase separation and of the liquid-liquid interface. *Journal of Physical Chemistry B* **110**, 13076-13085, (2006).
- 177 Zhao, W., Eslami, H., Cavalcanti Welch, L. & Müller-Plathe, F. in *Zeitschrift für Physikalische Chemie* Vol. 221 1647 (2007).
- 178 Youngs, T. G. A. & Hardacre, C. Application of Static Charge Transfer within an Ionic-Liquid Force Field and Its Effect on Structure and Dynamics. *ChemPhysChem* **9**, 1548-1558, (2008).
- 179 Chaban, V. Polarizability versus mobility: atomistic force field for ionic liquids. *Physical Chemistry Chemical Physics* **13**, 16055-16062, (2011).
- 180 Chaban, V. V. & Prezhdo, O. V. A new force field model of 1-butyl-3-methylimidazolium tetrafluoroborate ionic liquid and acetonitrile mixtures. *Physical Chemistry Chemical Physics* **13**, 19345-19354, (2011).
- 181 Chaban, V. V., Voroshylova, I. V. & Kalugin, O. N. A new force field model for the simulation of transport properties of imidazolium-based ionic liquids. *Physical Chemistry Chemical Physics* **13**, 7910-7920, (2011).
- 182 Liu, Z., Wu, W., Han, B., Dong, Z., Zhao, G., Wang, J., Jiang, T. & Yang, G. Study on the Phase Behaviors, Viscosities, and Thermodynamic Properties of CO₂/[C4mim][PF₆]/Methanol System at Elevated Pressures. *Chemistry – A European Journal* **9**, 3897-3903, (2003).
- 183 Shariati, A. & Peters, C. J. High-pressure phase behavior of systems with ionic liquids: measurements and modeling of the binary system fluoroform+1-ethyl-3-methylimidazolium hexafluorophosphate. *The Journal of Supercritical Fluids* **25**, 109-117, (2003).
- 184 Peng, D.-Y. & Robinson, D. B. A New Two-Constant Equation of State. *Industrial & Engineering Chemistry Fundamentals* **15**, 59-64, (1976).
- 185 Yokozeki, A. Solubility of Refrigerants in Various Lubricants. *International Journal of Thermophysics* **22**, 1057-1071, (2001).
- 186 You, S.-S., Yoo, K.-P. & Lee, C. S. An approximate nonrandom lattice theory of fluids: General derivation and application to pure fluids. *Fluid Phase Equilibria* **93**, 193-213, (1994).
- 187 You, S.-S., Yoo, K.-P. & Soo Lee, C. An Approximate Nonrandom Lattice Theory of Fluids: Mixtures. *Fluid Phase Equilibria* **93**, 215-232, (1994).
- 188 Hu, Y., Liu, H. & Prausnitz, J. M. Equation of state for fluids containing chainlike molecules. *The Journal of Chemical Physics* **104**, 396-404, (1996).
- 189 Kontogeorgis, G. M., Voutsas, E. C., Yakoumis, I. V. & Tassios, D. P. An Equation of State for Associating Fluids. *Industrial & Engineering Chemistry Research* **35**, 4310-4318, (1996).
- 190 Chapman, W. G., Gubbins, K. E., Jackson, G. & Radosz, M. New reference equation of state for associating liquids. *Industrial and Engineering Chemistry Research*® **29**, 1709-1721, (1990).

- 191 Chapman, W. G., Gubbins, K. E., Jackson, G. & Radosz, M. SAFT: Equation-of-state solution model for associating fluids. *Fluid Phase Equilibria* **52**, 31-38, (1989).
- 192 Huang, S. H. & Radosz, M. Equation of state for small, large, polydisperse, and associating molecules. *Industrial and Engineering Chemistry Research*® **29**, 2284-2294, (1990).
- 193 Huang, S. H. & Radosz, M. Equation of state for small, large, polydisperse, and associating molecules: extension to fluid mixtures. *Industrial & Engineering Chemistry Research* **30**, 1994-2005, (1991).
- 194 Gross, J. & Sadowski, G. Perturbed-chain SAFT: An equation of state based on a perturbation theory for chain molecules. *Industrial and Engineering Chemistry Research* **40**, 1244-1260, (2001).
- 195 Karakatsani, E. K., Spyriouni, T. & Economou, I. G. Extended statistical associating fluid theory (SAFT) equations of state for dipolar fluids. *AIChE Journal* **51**, 2328-2342, (2005).
- 196 For more information visit: <http://www.iolicap.eu/>.
- 197 Phillips, J. C. *et al.* Scalable molecular dynamics with NAMD. *Journal of Computational Chemistry* **26**, 1781-1802, (2005).
- 198 Jacquemin, J., Husson, P., Mayer, V. & Cibulka, I. High-pressure volumetric properties of imidazolium-based ionic liquids: Effect of the anion. *Journal of Chemical and Engineering Data* **52**, 2204-2211, (2007).
- 199 Andreatta, A. E., Arce, A., Rodil, E. & Soto, A. Physical Properties of Binary and Ternary Mixtures of Ethyl Acetate, Ethanol, and 1-Octyl-3-methyl-imidazolium Bis(trifluoromethylsulfonyl)imide at 298.15 K. *Journal of Chemical & Engineering Data* **54**, 1022-1028, (2009).
- 200 Flory, P. J. *Statistical mechanics of chain molecules*. (Interscience Publishers, 1969).
- 201 Theodorou, D. N. & Suter, U. W. Detailed molecular structure of a vinyl polymer glass. *Macromolecules* **18**, 1467-1478, (1985).
- 202 Theodorou, D. N. & Suter, U. W. Atomistic modeling of mechanical properties of polymeric glasses. *Macromolecules* **19**, 139-154, (1986).
- 203 More information can be found in www.scienomics.com.
- 204 Martyna, G. J., Tuckerman, M. E., Tobias, D. J. & Klein, M. L. Explicit reversible integrators for extended systems dynamics. *Molecular Physics* **87**, 1117-1157, (1996).
- 205 Cadena, C., Zhao, Q., Snurr, R. Q. & Maginn, E. J. Molecular modeling and experimental studies of the thermodynamic and transport properties of pyridinium-based ionic liquids. *Journal of Physical Chemistry B* **110**, 2821-2832, (2006).
- 206 Canongia Lopes, J. N. & Pádua, A. A. H. Molecular Force Field for Ionic Liquids Composed of Triflate or Bistriflylimide Anions. *The Journal of Physical Chemistry B* **108**, 16893-16898, (2004).

- 207 Tokuda, H., Tsuzuki, S., Susan, M., Hayamizu, K. & Watanabe, M. How Ionic Are Room-Temperature Ionic Liquids? An Indicator of the Physicochemical Properties. *The Journal of Physical Chemistry B* **110**, 19593-19600, (2006).
- 208 Shah, J. K., Brennecke, J. F. & Maginn, E. J. Thermodynamic properties of the ionic liquid 1-n-butyl-3-methylimidazolium hexafluorophosphate from Monte Carlo simulations. *Green Chemistry* **4**, 112-118, (2002).
- 209 Margulis, C. J., Stern, H. A. & Berne, B. J. Computer simulation of a "green chemistry" room-temperature ionic solvent. *Journal of Physical Chemistry B* **106**, 12017-12021, (2002).
- 210 Hanke, C. G., Price, S. L. & Lynden-Bell, R. M. Intermolecular potentials for simulations of liquid imidazolium salts. *Molecular Physics* **99**, 801-809, (2001).
- 211 Makrodimitri, Z. A., Unruh, D. J. M. & Economou, I. G. Molecular simulation of diffusion of hydrogen, carbon monoxide, and water in heavy n -alkanes. *Journal of Physical Chemistry B* **115**, 1429-1439, (2011).
- 212 Mondello, M., Grest, G. S., Webb, E. B. & Peczak, P. Dynamics of n-alkanes: Comparison to Rouse model. *The Journal of Chemical Physics* **109**, 798-805, (1998).
- 213 Hansen, J.-P. & McDonald, I. R. in *Theory of Simple Liquids (Third Edition)* eds Jean-Pierre Hansen and Ian R. McDonald) 341-392 (Academic Press, 2006).
- 214 Doxastakis, M., Theodorou, D. N., Fytas, G., Kremer, F., Faller, R., Müller-Plathe, F. & Hadjichristidis, N. Chain and local dynamics of polyisoprene as probed by experiments and computer simulations. *Journal of Chemical Physics* **119**, 6883-6894, (2003).
- 215 Pasini, P., Zannoni, C. & Žumer, S. *Computer Simulations of Liquid Crystals and Polymers: Proceedings of the NATO Advanced Research Workshop on Computational Methods for Polymers and Liquid Crystalline Polymers, Erice, Italy. 16-22 July 2003.* (Springer, 2005).
- 216 Logotheti, G. E. & Theodorou, D. N. Segmental and chain dynamics of isotactic polypropylene melts. *Macromolecules* **40**, 2235-2245, (2007).
- 217 Arrighi, V., Batt-Coutrot, D., Zhang, C., Telling, M. T. F. & Triolo, A. Effect of tacticity on the local dynamics of polypropylene melts. *The Journal of Chemical Physics* **119**, 1271-1278, (2003).
- 218 Martinelli, A., Marechal, M., Ostlund, A. & Cambedouzou, J. Insights into the interplay between molecular structure and diffusional motion in 1-alkyl-3-methylimidazolium ionic liquids: a combined PFG NMR and X-ray scattering study. *Physical Chemistry Chemical Physics* **15**, 5510-5517, (2013).
- 219 Liu, Z., Huang, S. & Wang, W. A Refined Force Field for Molecular Simulation of Imidazolium-Based Ionic Liquids. *The Journal of Physical Chemistry B* **108**, 12978-12989, (2004).
- 220 Köddermann, T., Paschek, D. & Ludwig, R. Molecular Dynamic Simulations of Ionic Liquids: A Reliable Description of Structure, Thermodynamics and Dynamics. *ChemPhysChem* **8**, 2464-2470, (2007).

- 221 Tariq, M., Carvalho, P. J., Coutinho, J. A. P., Marrucho, I. M., Lopes, J. N. C. & Rebelo, L. P. N. Viscosity of (C2-C14) 1-alkyl-3-methylimidazolium bis(trifluoromethylsulfonyl)amide ionic liquids in an extended temperature range. *Fluid Phase Equilibria* **301**, 22-32, (2011).
- 222 McFarlane, J., Ridenour, W. B., Luo, H., Hunt, R. D., DePaoli, D. W. & Ren, R. X. Room temperature ionic liquids for separating organics from produced water. *Separation Science and Technology* **40**, 1245-1265, (2005).
- 223 Yu, H. & van Gunsteren, W. F. Accounting for polarization in molecular simulation. *Computer Physics Communications* **172**, 69-85, (2005).
- 224 Lamoureux, G. & Roux, B. Modeling induced polarization with classical Drude oscillators: Theory and molecular dynamics simulation algorithm. *The Journal of Chemical Physics* **119**, 3025-3039, (2003).
- 225 Anisimov, V. M., Lamoureux, G., Vorobyov, I. V., Huang, N., Roux, B. & MacKerell, A. D. Determination of Electrostatic Parameters for a Polarizable Force Field Based on the Classical Drude Oscillator. *Journal of Chemical Theory and Computation* **1**, 153-168, (2004).
- 226 Harder, E., Anisimov, V. M., Vorobyov, I. V., Lopes, P. E. M., Noskov, S. Y., MacKerell, A. D. & Roux, B. Atomic Level Anisotropy in the Electrostatic Modeling of Lone Pairs for a Polarizable Force Field Based on the Classical Drude Oscillator. *Journal of Chemical Theory and Computation* **2**, 1587-1597, (2006).
- 227 Geerke, D. P. & van Gunsteren, W. F. On the Calculation of Atomic Forces in Classical Simulation Using the Charge-on-Spring Method To Explicitly Treat Electronic Polarization. *Journal of Chemical Theory and Computation* **3**, 2128-2137, (2007).
- 228 Baker, C. & MacKerell, A., Jr. Polarizability rescaling and atom-based Thole scaling in the CHARMM Drude polarizable force field for ethers. *J Mol Model* **16**, 567-576, (2010).
- 229 van Duijnen, P. T. & Swart, M. Molecular and Atomic Polarizabilities: Thole's Model Revisited. *The Journal of Physical Chemistry A* **102**, 2399-2407, (1998).
- 230 Kolbeck, C., Lehmann, J., Lovelock, K. R. J., Cremer, T., Paape, N., Wasserscheid, P., Fröba, A. P., Maier, F. & Steinrück, H. P. Density and surface tension of ionic liquids. *Journal of Physical Chemistry B* **114**, 17025-17036, (2010).
- 231 Van Hove, L. Correlations in Space and Time and Born Approximation Scattering in Systems of Interacting Particles. *Physical Review* **95**, 249-262, (1954).
- 232 Rahman, A. Correlations in the Motion of Atoms in Liquid Argon. *Physical Review* **136**, A405-A411, (1964).
- 233 Gaub, M., Fritzsche, S., Haberlandt, R. & Theodorou, D. N. Van Hove function for diffusion in zeolites. *Journal of Physical Chemistry B* **103**, 4721-4729, (1999).
- 234 Martin, M. G., Maginn, E. J., Rogers, R. D., Voth, G. & Gordon, M. S. *Technologies for Developing Predictive Atomistic and Coarse-Grained Force Fields for Ionic Liquid Property Prediction*, <<http://handle.dtic.mil/100.2/ADA486185>> (2008).

- 235 Personal communication with Dr. Peter Schulz from Institute of Chemical Reaction Engineering, University of Erlangen-Nuremberg, Erlangen, Germany. Unpublished results.
- 236 Androulaki, E., Vergadou, N., Hill, J.-H. & Ecomomou, I. G. Molecular Simulation of Imidazolium-Based Tricyanomethanide Ionic Liquids using an Optimized Classical Force Field. *in preparation*.
- 237 Królikowski, M., Walczak, K. & Domańska, U. Solvent extraction of aromatic sulfur compounds from n-heptane using the 1-ethyl-3-methylimidazolium tricyanomethanide ionic liquid. *The Journal of Chemical Thermodynamics* **65**, 168-173, (2013).
- 238 Larriba, M., Navarro, P., García, J. & Rodríguez, F. Liquid–Liquid Extraction of Toluene from Heptane Using [emim][DCA], [bmim][DCA], and [emim][TCM] Ionic Liquids. *Industrial & Engineering Chemistry Research* **52**, 2714-2720, (2013).
- 239 Carvalho, P. J., Regueira, T., Santos, L. M. N. B. F., Fernandez, J. & Coutinho, J. o. A. P. Effect of Water on the Viscosities and Densities of 1-Butyl-3-methylimidazolium Dicyanamide and 1-Butyl-3-methylimidazolium Tricyanomethane at Atmospheric Pressure†. *Journal of Chemical & Engineering Data* **55**, 645-652, (2010).
- 240 Domańska, U., Królikowska, M. & Walczak, K. Effect of temperature and composition on the density, viscosity surface tension and excess quantities of binary mixtures of 1-ethyl-3-methylimidazolium tricyanomethanide with thiophene. *Colloids and Surfaces A: Physicochemical and Engineering Aspects* **436**, 504-511, (2013).
- 241 Harris, J. G. & Yung, K. H. Carbon Dioxide's Liquid-Vapor Coexistence Curve And Critical Properties as Predicted by a Simple Molecular Model. *The Journal of Physical Chemistry* **99**, 12021-12024, (1995).
- 242 Martin, M. G. & Siepmann, J. I. Transferable Potentials for Phase Equilibria. 1. United-Atom Description of n-Alkanes. *The Journal of Physical Chemistry B* **102**, 2569-2577, (1998).
- 243 Stan, G., Bojan, M. J., Curtarolo, S., Gatica, S. M. & Cole, M. W. Uptake of gases in bundles of carbon nanotubes. *Physical Review B* **62**, 2173-2180, (2000).
- 244 Rivera, J. L., Alexandre, J., Nath, S. K. & De Pablo, J. J. Thermodynamic and transport properties of nitrogen and butane mixtures. *Molecular Physics* **98**, 43-55, (2000).
- 245 Miyano, Y. Molecular simulation with an EOS algorithm for vapor–liquid equilibria of oxygen and ethane. *Fluid Phase Equilibria* **158–160**, 29-35, (1999).
- 246 Morgan, D., Ferguson, L. & Scovazzo, P. Diffusivities of Gases in Room-Temperature Ionic Liquids: Data and Correlations Obtained Using a Lag-Time Technique. *Industrial & Engineering Chemistry Research* **44**, 4815-4823, (2005).
- 247 Moganty, S. S. & Baltus, R. E. Diffusivity of Carbon Dioxide in Room-Temperature Ionic Liquids. *Industrial & Engineering Chemistry Research* **49**, 9370-9376, (2010).

- 248 Camper, D., Becker, C., Koval, C. & Noble, R. Diffusion and Solubility Measurements in Room Temperature Ionic Liquids. *Industrial & Engineering Chemistry Research* **45**, 445-450, (2005).
- 249 Hou, Y. & Baltus, R. E. Experimental Measurement of the Solubility and Diffusivity of CO₂ in Room-Temperature Ionic Liquids Using a Transient Thin-Liquid-Film Method. *Industrial & Engineering Chemistry Research* **46**, 8166-8175, (2007).
- 250 Hazelbaker, E. D., Budhathoki, S., Katihar, A., Shah, J. K., Maginn, E. J. & Vasenkov, S. Combined application of high-field diffusion NMR and molecular dynamics simulations to study dynamics in a mixture of carbon dioxide and an imidazolium-based ionic liquid. *Journal of Physical Chemistry B* **116**, 9141-9151, (2012).
- 251 Condemarin, R. & Scovazzo, P. Gas permeabilities, solubilities, diffusivities, and diffusivity correlations for ammonium-based room temperature ionic liquids with comparison to imidazolium and phosphonium RTIL data. *Chemical Engineering Journal* **147**, 51-57, (2009).
- 252 Finotello, A., Bara, J. E., Camper, D. & Noble, R. D. Room-Temperature Ionic Liquids: Temperature Dependence of Gas Solubility Selectivity. *Industrial & Engineering Chemistry Research* **47**, 3453-3459, (2007).
- 253 Membranes and Microporous Materials for Environmental Separations Laboratory, National Center for Scientific Research "Demokritos", Athens, Greece. For more information visit: mesl.chem.demokritos.gr/.
- 254 School in Advanced Optical Technologies, University of Erlangen-Nuremberg, Erlangen, Germany. For more information visit: <http://www.aot.uni-erlangen.de/saot/home.html>.
- 255 Widom, B. Some Topics in the Theory of Fluids. *The Journal of Chemical Physics* **39**, 2808-2812, (1963).
- 256 Theodorou, D. N. in *Materials Science of Membranes for Gas and Vapor Separation* 49-94 (John Wiley & Sons, Ltd, 2006).
- 257 Gan, Q., Zou, Y., Rooney, D., Nancarrow, P., Thompson, J., Liang, L. & Lewis, M. Theoretical and experimental correlations of gas dissolution, diffusion, and thermodynamic properties in determination of gas permeability and selectivity in supported ionic liquid membranes. *Advances in Colloid and Interface Science* **164**, 45-55, (2011).
- 258 Husson-Borg, P., Majer, V. & Costa Gomes, M. F. Solubilities of Oxygen and Carbon Dioxide in Butyl Methyl Imidazolium Tetrafluoroborate as a Function of Temperature and at Pressures Close to Atmospheric Pressure†. *Journal of Chemical & Engineering Data* **48**, 480-485, (2003).
- 259 Scovazzo, P., Havard, D., McShea, M., Mixon, S. & Morgan, D. Long-term, continuous mixed-gas dry fed CO₂/CH₄ and CO₂/N₂ separation performance and selectivities for room temperature ionic liquid membranes. *Journal of Membrane Science* **327**, 41-48, (2009).
- 260 Scovazzo, P. Determination of the upper limits, benchmarks, and critical properties for gas separations using stabilized room temperature ionic liquid membranes

(SILMs) for the purpose of guiding future research. *Journal of Membrane Science* **343**, 199-211, (2009).